First-Principles Study of Bismuth at Transition Metal Surfaces, Interfaces and Boron Carbide Bulk Thermodynamics

by

Qin Gao

Submitted in partial fulfillment of the
requirements for the degree of
Doctor of Philosophy
at

Carnegie Mellon University
Department of Physics
Pittsburgh, Pennsylvania

Advised by Professor Michael Widom

December 12, 2015

Abstract

With the help of density functional theory (DFT) and powerful computers, first-principles computation of solid state systems can be performed to accurately explain and predict nanoscale phenomena. This thesis focuses on our first-principles investigation of bismuth on the Ni(111) surface, at transition metal interfaces, and describes our study of boron carbide bulk thermodynamics combining DFT calculations, machine learning methods and Monte Carlo simulations. Our Bi on Ni(111) surface study confirms the stability of odd-layer Bi films, proposes specific stable atomic structures, and explains their stability with covalent chemical bonding. Our research of Bi at transition metal grain boundaries verifies the stability of bilayer films, explains the difference between transition metals, and proposes a model for bilayer stability on general grain boundaries. Although DFT calculations are accurate, they can be time consuming and scale badly with system size. Our DFT-based machine learning interaction models are used to capture certain non-linear effects associated with many-body interactions blue which reduce the error of prediction by $20 - 33\%$ comparing to a linear model. We utilize these models to evaluate the thermodynamics of boron carbide in Monte Carlo simulations and identify three boron carbide phases.

Acknowledgments

First and foremost, I would like to express my profound gratitude to my advisor Michael Widom for his wise guidance, support and help.

I would like to thank my doctoral committee members, Michael Widom (chair), Randall Feenstra, Di Xiao and Anthony Rollett for advice on my PhD research and this thesis.

I would like to thank Randall Feenstra for extensive collaboration and guidance on the study of first-principle low energy electron reflectivity, Jeff Schneider for guidance on constructing and analyzing machine learning models, Di Xiao for elevating my understanding on quantum size effect, MURI collaborators Martin Harmer, Jian Luo, Anthony Rollett, Greg Rohrer and Zhiyang Yu for collaboration and discussion on bismuth at transition metal interfaces, and Marek Mihalkovič for illuminating discussion. Thanks to Manfred Paulini and Stephen Garoff for academic and administrative help.

I would like to thank Bruce McWilliams and the McWilliams Fellowship committee for awarding me the prestigious McWilliams Fellowship in 2014 that supported my exploration on exciting problems.

Thanks to the fellow graduate students that overlaped with me in Professor Widom's group, Ben Sauerwine, Will Huhn, Sanxi Yao and Bojun Feng for discussion, collaboration and accompany.

Last but not least, the support from my parents Shiqing Gao, Jianjun Wang and my fiancée Rulin Chen is invaluable, without which this thesis cannot be finished.

This work was financially supported by the ONR-MURI under the grant NO. N00014-11-1-0678 and the McWilliams Fellowship.

Contents

1 Introduction **1**

1.1 The Need For Density Functional Theory 2

1.2 Bi grain boundary complexions in transition metal 3

1.2.1 Experiments 4

1.2.2 Analytic thermodynamic models 7

1.2.3 Molecular dynamics and Monte Carlo simulations of complexion transitions 9

1.3 Boron Carbide bulk thermodynamics 10

1.4 Structure of this thesis 11

2 First Principle Methods **12**

2.1 Density Functional Theory 12

2.1.1 Schrodinger equation 12

2.1.2 Slater Determinant and Hartree-Fock Energy 14

2.1.3 Hohenberg-Kohn Theorems 15

2.1.4 Kohn-Sham Ansatz 17

2.1.5 Exchange and Correlation Energy 18

2.1.6 Collinear Spin-polarization 21

2.2 Plane-wave Methods 21

2.2.1 Plane-wave expansion 23

2.2.2 Pseudopotentials 26

2.2.3 Force on Nuclei and Relaxation 27
2.3 Corrections to Total Energy 28
2.3.1 SOC 28
2.3.2 Temperature corrections 32

3 Bi on Ni(111) Surface 37
3.1 Introduction 37
3.2 Methods 39
3.3 Results and Discussion 41
3.4 Conclusion 46
3.5 Appendix 47
3.5.1 A1. Lateral strain 47
3.5.2 A2. Quantum size effect 49

4 Bi on Transition Metal Grain Boundaries 52
4.1 Introduction 52
4.2 Methods 53
4.3 Results and Discussion 55
4.3.1 A. Film stability 55
4.3.2 B. Thermodynamic Model 60
4.3.3 C. Embrittlement and differences among TMs 62
4.3.4 D. Vibrational Free Energies 64
4.4 Conclusion 65
4.5 Appendix 66
4.5.1 A1. Bi bilayer on Fe $\Sigma 5(012)$ GB 66
4.5.2 A2. Convergence with respect to number of Ni layers 67

5 Boron Carbide thermodynamics with Machine Learning methods 69
5.1 Introduction 69
5.2 Methods 71

5.2.1 DFT calculations 71
5.2.2 Supervised Regression Models 71
5.2.3 Cross validation 76
5.2.4 Monte Carlo 77
5.3 Results and analysis 77
5.3.1 Model Selection and Acceleration 79
5.4 Monte Carlo simulation 81
5.5 Conclusion 84
5.6 Appendix 85
5.6.1 A1. Data Exploration 85
5.6.2 A2. Residuals of Linear model and GP 85

6 Summary and Future Work **88**
6.1 Summary 88
6.2 Future Work 90

List of Tables

4.1 GB energies, units are eV/Å^2. The energy conversion factor is 1 eV/Å^2 =16 J/m^2. Values from other studies are in parentheses. Note the Co $\Sigma 3(111)$ GB energy is negative because the $T = 0$ K state is HCP rather than the high-T FCC that we choose to compare with. . 55

4.2 Calculated input quantities for the enthalpy model (Eq. 3). Predicted $E_{\mathrm{GB}}^{\mathrm{min}}$ values for GB with the same surface plane (i.e. $a = b$) at two sides. The energy units are eV/Å^2. The Bi monolayer structure on Ni(100) surface is the $c(2 \times 2)$ structure as observed in experiment [1]. 61

4.3 Model and calculated Ni GB energies and Bi bilayer enthalpies of formation at different Ni GBs. Work of separation for bare and Bi bilayer segregated GBs is shown on right. The energy units are eV/Å^2. The $\Sigma 7(111)$ GB is made by twisting the one side of bulk Ni by 21.8^o around the [111] axis with (111) as GB plane. The resulting GB cell is [3-112] as defined in [2] on which Bi favors 3 atoms per layer. The $\Sigma 5(100)$ GB is made by twisting one side of bulk Ni by 36.9^o around the [001] axis with (001) as GB plane. The general GB (111)/(100) is constructed with a =(111) and b =(100) planes with a (3×3) surface cell at the a side and a [2-213] surface cell (following the notation of [2]) at the b side. Unlike the CSL GBs, this general GB ΔH^{calc} is greater than ΔH^{model} due to strain of the Ni cells (around 5%). This artificial strain introduced by forcing the two weakly interacting grains to share a common small cell makes the direct calculation inaccurate. 62

4.4 The (012) surface energy, Bi monolayer enthalpies of formation, integrated COHP (iCOHP) energies of Bi-TM bond, TM-TM bond near to Bi(a) and TM-TM bond away from impurities(b). The energy units are eV/bond for the iCOHP energies. 63

4.5 $\Delta F(T)/A$ of Bi bilayer at TM GBs, units are eV/Å^2. Values in parenthesis are $\Delta H/A$. 66

5.1 RMSE of 5-fold cross validation and improvement of different models. The standard error of these quantities are obtained from the statistics of ten repetitions of cross validation. 78

List of Figures

1.1 (A) Cross-section of a Ni polycrystal in contact with liquid Ni-Bi alloy. Top left region shows a micrometer thick intergranular penetration tip. Middle region shows long crack due to the penetration tip and the nanometrer-thick film. (B) Schematic representation of Bi concentration profile across the fracture surface between the external surface and the ductile core in Ni-Bi system at 700°C. (C) Cu-rich side of the Cu-Bi phase diagram. The thick curve is the (retrograde) bulk solidus line [3]. The thin retrograde curve is the GB solidus line obtained for the Cu-Bi polycrystals [3]. The horizontal lines at $T_{\mathrm{w,max}}$ and $T_{\mathrm{w,min}}$ are GB wetting phase transition tie-lines. (A) and (B) are reprinted from [4] with permission, (C) is reprinted from [5] with permission. . 5

1.2 (Color online)(A, D) STEM HAADF micrographs showing Bi bilayer complexion. (B, C) Brittle decohesion occurs due to the bilayer complexion. (E) Coexistence of bilayer and trilayer interfacial phases at a single GB, indicating a possible GB phase transition between them. (F) Measured (projected) distances between two neighboring adsorbed Bi atom columns across two adsorbed layers. The large layer spacing (3.9 Å) between Bi layers indicates weak interaction and embrittlement. All panels are reprinted from [6] with permission from AAAS. . 6

1.3 (Color online) (A) GB composition of Pt-1 at % Au (100) 43.6^o GB at 850 K Model predicted by model of Wynblatt et al [7] and MC simulation [8]. Error bars on simulation results represent one standard deviation. (B) Portion of the three-dimensional phase diagram for the model alloy with certain parameters, showing superposition of the prewetting line and its extension for a FCC (311)-(311) GB generated by model of Wynblatt et al [9]. (A) is reprinted from [7] with permission and (B) is reprinted from [9] with permission. 7

1.4 (Color online) Complexion transformation of pure Cu Σ5(310) GB and Ag segregated Cu Σ5(120) GB. (A) Coexistance of kites complexion and split kites complexion with the geometry of a wall of fixed atoms at left and an open surface at right. Cu (B) kites and (C) split kites complexion at Cu Σ5(310) and (D) their 1D-phase boundary separation accompanied by a step. (E) Coexistance of spit kites complexion and filled kites complexion with the geometry of open surfaces at both left and right of Ag segregated Cu Σ5(120) GB. Ag segregated Cu (F) split kites and (G) filled kites complexion at Cu Σ5(120). (A-D) is reprinted from [10] with permission. (E-G) is reprinted from [11] with permission. 9

2.1 Electron density difference between bulk Bi and atomic Bi. Cyan circles are Bi atoms. Electron density isosurface for $0.028|e|/\text{Å}^3$ are plotted. Red is for charge excess and green for charge deficient. 22

2.2 Bulk FCC Ni density of states. Solid lines for spin up and dashed lines (y-axis inverted) for spin down. Black for all orbitals, red for s orbitals, blue for p orbitals, and orange for d orbitals. The black dotted line is the Fermi energy. 23

2.3 The first Brillouin zone of face-centered cubic (FCC) crystal. The labels on the figure are the special symmetric points. Reprinted from Wikipedia website. 24

2.4 Sketch of the effective potential of the nucleus and inner-shell electrons V_{eff} and corresponding wavefunction Ψ (blue), and the pseudopotential V_{pseudo} and corresponding wavefunction Ψ_{pseudo} (red). The Ψ_{pseudo} and V_{pseudo} are the same as Ψ and V_{eff} respectively outside the distance r_c. Adapted and modified from Wikipedia. 28

2.5 Band structure of Bi along the Γ-T direction in its Brillouin zone [12]. Left is calculated with spin-orbital coupling, right without. 29

2.6 Phonon density of states of bulk FCC Ni with different cell sizes. $4 \times 4 \times 4$ cell has 64 repetition of the primitive cell and thus contains 64 Ni atoms. 35

2.7 Vibrational free energy F_{vib} of bulk FCC Ni with different cell sizes and electronic free energy F_e of bulk FCC Ni. $4 \times 4 \times 4$ cell has 64 repetition of the primitive cell and thus contains 64 Ni atoms. F_e is calculated with the primitive cell. 36

3.1 (Color online) Top view (top left) and side view (top middle) of relaxed 4-layer hexagonal Bi film on Ni (111) (3×3) cell (dashed). Same for 3 layer hR2 Bi film (bottom). Insert at top of the left-hand figure is a histogram of atoms at different heights. Shading in insert convers the region illustrated containing the top layer of Ni, the Bi surface monolayer and additional Bi layers. Atom size indicates depth (large below small). Length units are in Å . Chemical bonding is shown at right (slightly tilted). 40

3.2 (Color online) Relative surface energies of hexagonal Bi films with (3×3) (top) and [3-112] (bottom) Ni (111) surface cells. Note the energy conversion factor is 1 eV/Å^2=16.0 J/m^2. Red and blue points are from collinear calculations, green points are noncollinear. Data points connected by line segments correspond to coverage of integer numbers of monolayers (1-9 for (3×3), 1-11 for [3-112]). Extra data points in the (3×3) cell are three layer films with one extra capping atom at a valley site. Extra points in the [3-112] cell are 4 layer plus one atom, and 8 layer plus one atom at valley sites. 41

3.3 (Color online) Enthalpy of formation. Dot-dashed orange points are the (sub)monolayer structures with (3×3) cell. Cyan and green stars are the (7×7) and (8×8) surface monolayer respectively. Red points are hexagonal films and black are hR2 Bi films on the (3×3) cell. Blue points are hexagonal Bi films on the [3-112] cell. Color and plotting symbol are shared with Fig. 3.2 for (3×3) and [3-112] cells. 44

3.4 (Color online) Surface free energy. Dashed-dotted lines stand for monolayer or less. Solid and dotted lines stand for hexagonal and hR2 films on (3×3) cells respectively. Different slopes indicate different coverage according to Eq. 3.3. Stable sequence is indicated by arrows for monolayer or more. Vertical line at $\Delta\mu$ =0 indicates chemical potential of unstrained bulk Bi. 45

3.5 (Color online) Bi bulk energy of hexagonal and hR2 structures. Black is the relaxed hR2 structure. Red is the relaxed hexagonal structure. Blue is the evenly spaced hexagonal structure. Points (a),(b),(c),(d) correspond to the structures whose energies are plotted in Fig. 3.6. . 48

3.6 (Color online) Surface energies of free standing Bi films with different in-plane lattice constants a (units of Å). Black and red curves are using collinear calculation. Green using noncollinear. 51

4.1 (Color online) Left: Side view of our $\Sigma5(012)$ GB. The black cell is our unit cell. The dashed green lines are GB planes. Right: Top view of $\Sigma5(012)$ GB plane. Three layers of atoms are shown. The black solid cell is the orthorhombic unit cell we use to calculate $\Sigma5(012)$ GB energies. Atom size indicates depth (large below small). Units are Å. 54

4.2 (Color online) Enthalpies of Bi films at $\Sigma3(111)$ and $\Sigma5(012)$ GBs. Solid lines connect Bi films on $\Sigma3(111)$ GBs. Films of 1-3 layer thickness (labeled 1-3) have 4 Bi atoms per layer while the 4-layer films contain 4 Bi atoms per layer in layers adjacent to Ni but 3 Bi per layer in the middle two layers [13] for Ni and Co. Films for Cu have 2 Bi per layer. Dashed lines connect Bi films in (1×1) cells of $\Sigma5(120)$ GBs. Red, green and blue colors indicate Co, Ni and Cu respectively. Square points (labeled as $3'$) stand for trilayer films in (3×1) cells of $\Sigma5(120)$ GBs with denser middle layer (4 Bi in (3×1) cell). Diamond points (labeled as $4'$) stand for four layer films in (1×4) cells of $\Sigma5(012)$ GBs with the in-plane density of the middle bilayer similar to bulk Bi (3 Bi in a (1×4) cell). 57

4.3 (Color online) GB free energy of Bi films at Co, Ni, Cu $\Sigma5(120)$ GBs, respectively, top to bottom. The black solid lines stand for bare GBs while the black dashed lines stand for infinite bulk-like Bi films. Other lines are for different Bi films, with stable bilayer labeled. 58

4.4 (Color online) Relaxed bilayer Bi films at (1×1) cell of Ni $\Sigma5(120)$ GB. Only Ni atoms close to Bi are shown. Atom size indicates depth (large below small). Units are Å. 59

4.5 (Color online) Grain boundary energies calculated by DFT compared with embedded atom method (EAM) for Ni and Cu. The EAM data is taken from [14]. Numbers shown in the figure are the Σ values of those CSL GBs. For both metals, the results show similar trends and differ by less than 0.005 eV/ Å^2. 61

4.6 (Color online) Differential COHP of Metal-Metal interaction in the bulk and near to Bi. Negative is bonding while positive is antibonding. The Ni and Co results are the summation of two spin components. The dashed green line is the x axis. The zero in x axis is the Fermi energy. 65

4.7 (Color online) Side view (left) of relaxed Bi bilayer at Fe Σ5(012) GB and top view (right) of Bi monolayer on one side of the GB plane. The cyan cell is the Fe GB unit cell, the green cell is the Bi segregated GB unit cell. Atom size indicates depth (large below small). Length units are in Å. 67

4.8 (Color online) Convergence with respect to the number of Ni layers in calculation of Bi bilayer at Ni Σ5(210) GB. 68

5.1 (a) GP and (b) SVR fits of a toy one-dimensional function. The dashed-red curve is the ground truth function. A "o" denotes a data point which is drawn randomly from the ground truth function and added with Gaussian noise. The black solid lines in both panels are the fitted functions. (a) The shaded region lies within two standard error of the GP prediction (95% confidence interval). (b) The dashed curves are the boundaries of the ϵ-tube. The "o" points with "*" at the centers are support vectors. 75

5.2 (Color online) The predicted energies in 5-fold CV vs the ground truth DFT energies. The black line is $y = x$. Red points are from linear model and blue from GP predictions. 79

5.3 (Color online) RMSE of linear model, GP, NN and SVR vs number of features. The black curve is linear model, solid curves are GP with different kernels. Dashed curves are SVR with different kernels. The purple dot-dashed curve is NN. 80
5.4 (Color online) Energy histograms of the linear model (left), the 41-feature PR2 model (middle), and the mixed-kernel GP (right). 82
5.5 (Color online) The MC simulated heat capacity of boron carbide using the linear model (left), the 41-feature PR2 model (middle), and the mixed-kernel GP (right). 82
5.6 (Color online) Boron carbide phase diagram in the (X_C, T) plane. Black region is the Monoclinic phase, red is the Bipolar phase, and green is the Rhombohedral phase. 83
5.7 (Color online) Histograms (diagonal plots) and pairwise scatter plots (off-diagonal plots) of features and energies. The variables from left to right and from top to bottom are the polar C concentration x_C, number of nearest C-C bonds N_1, number of second nearest C-C bond N_2, and the DFT calculated energy E. All the three features are normalized. Every red star represents the value of one structure. 86
5.8 (Color online) Residuals of predicted energies in 5-fold CV of linear model (top) and GP (bottom). From left to right the x-axis represents the DFT energy, carbon concentration, number of nearest bonds and number of second nearest bonds, respectively. 87

Chapter 1

Introduction

This thesis presents our application of physics-based methods including first-principles density functional theory (DFT) calculations, machine learning, and Monte Carlo simulations to study bulk and surface structures of materials. DFT is an accurate and computationally efficient method that calculates energies of matter from quantum mechanical first principles. In this thesis, we attempt to overcome the computational cost limitation of DFT by combining physical models and machine learning methods with DFT. Since the electron density has to be determined in DFT by solving a set of coupled Schrodinger equations, it is too expensive to calculate structures containing thousands or more atoms in the smallest repeating unit. Thus we introduce models that allow us to approximate quantities of interest in large systems using accurate DFT input obtained for small systems.

Directly using DFT calculations, we propose the structures of Bi multilayer films on Ni(111) and that their stability are due to Bi covalent bonding. We also confirm Bi bilayer stability at Ni and Cu high energy grain boundaries and explain liquid metal embrittlement. We significantly reduce the computational cost to determine Bi bilayer stability by ignoring weak Bi interlayer interaction at transition metal GBs and using empirical potential calculated bare transition metal GB energies. Moreover, we develop a DFT/machine learning interatomic interaction model and perform Monte

Carlo simulations to study the boron carbide thermodynamics and phase diagram and identify three phases.

1.1 The Need For Density Functional Theory

Quantum mechanics provides explanations for a wide variety of physical phenomena. Some can be explained using simplified effective Hamiltonians (e.g. superconductivity [15], the quantum Hall effect [16], Dirac fermions in graphene [17], topological insulator [18]), but to accurately determine many properties of materials it is necessary to directly deal with the full Hamiltonian. However, it is difficult. Dirac has a famous quote in 1929 [19],

> "The underlying physical laws necessary for the mathematical theory of a large part of physics and the whole of chemistry are thus completely known, and the difficulty is only that the exact application of these laws leads to equations much too complicated to be soluble. It therefore becomes desirable that approximate practical methods of applying quantum mechanics should be developed, which can lead to an explanation of the main features of complex atomic systems without too much computation."

Wavefunction-based methods like Hartree-Fock can be used to approximately solve the Schrodinger equation of the full Hamiltonian, but becomes very computationally expensive for large systems. On the other hand, density functional theory (DFT), which takes the electron density rather than the wavefunctions as the basic variable is a widely used method that can accurately determine the properties of structures with much less computation. In principle, DFT is exact, however, in practice, it bears approximations from the exchange-correlation functional and finite basis cutoff. The details of DFT calculations will be discussed in Chapter 2. Most of the computations in this thesis employ DFT calculations.

1.2 Bi grain boundary complexions in transition metal[1]

Segregation at grain boundaries affects various properties of polycrystals such as grain growth [21, 22], liquid metal embrittlement (LME) [23, 24] and corrosion [25, 26]. However, the exact segregated structures, and hence the underlying mechanisms at atomic level, are far from being fully revealed. As a generalization of Gibbs' definition of phase, the new concept "complexion" was proposed to describe thermodynamically stable surface and interfacial structures [27, 28].

One example showing the importance of complexion is Bi film at transition metal grain boundaries. Bismuth replaces lead in solder alloys due to its low melting temperature and non-toxicity [29]. Bismuth naphthenate is used as environmentally friendly lubricant additives in extreme pressure applications [30]. Moreover, liquid Bi is used as a spallation target to generate neutrons due to its high neutron production rate [31]. However, liquid Bi is known to embrittle its solid container through grain boundary (GB) penetration. To understand and ultimately solve the liquid metal embrittlement problem, extensive theoretical and experimental studies were performed on Bi at metal GBs. The Micron-scale Bi penetration tips, nanometer-scale integranular films and bilayer complexions were discovered in experiments with Ni and Cu [32, 4, 6].

Analytical thermodynamic models based on ideal solution [9] and critical wetting theory [33, 34, 35] explain the complexion wetting and prewetting transitions [36]. First principles studies with density functional theory (DFT) calculations confirmed the stability of bilayer films and explained the difference between transition met-

[1]This section has been adapted from our paper "First Principles Study of Bismuth Films at Transition Metal Grain Boundaries" [20], and our review paper "Surface and grain boundary complexions in transition metal - bismuth alloys", to be published in the journal "Current Opinion in Solid State and Materials Science".

als [37, 20][2]. Molecular dynamics (MD) simulation demonstrates complexion transitions in pure Cu [10] and Ag segregated Cu [11], and agreed well with the diffusion experiments [38]. People debate over whether liquid metal embrittlement (LME) is due to an electronic effect [39] or atomic size effect [40] based on monolayer segregation models.

This section will review Bi complexions at transition metal GBs from the aspects of experiments, analytical models and MD simulations. Our DFT study of Bi complexions at Ni(111) surface and transition metal GBs will be discussed in Chapter 3 and Chapter 4 respectively.

1.2.1 Experiments

Liquid metal embrittlement (LME) is a long standing puzzle for physics and material science community. Severe embrittlement occurs when ductile metals like Ni and Cu contact liquid metals like Bi. Experimental studies using Auger Electron Spectroscopy (AES) and scanning electron microscopy (SEM) focused on the properties of the liquid metal penetration tip, which is tens or hundreds of microns long and several microns thick liquid Bi formed by wetting [32] the transition metal GB as shown in Fig. 1.1(A). The penetration tip dissociates the GB by forming two solid-liquid interfaces which are regarded as complexions [41], with bulk liquid Bi-Ni alloy in-between. The region in front of the penetration tip is believed to be a plastic deformation zone [42, 43]. Recent experiments found Mn, Sn, and Fe impurities in solid Ni enhance the integranular penetration 10 - 20 fold [44]. Based on thermodynamic models, it is inferred that Mn and Sn segregate to the Ni GB and change the penetration morphologies. While Fe in solid Ni is expected to have no effect due to its large solubility, Fe in a liquid Bi-Ni alloy precipitates, consumes Ni, causes dissolution of Ni from the Ni GB, and thus enhance the integranular penetration.

Besides the penetration tip, SEM and AES measurements indicate a nanometer-

[2]Will be discussed in detail in Chapter 4.

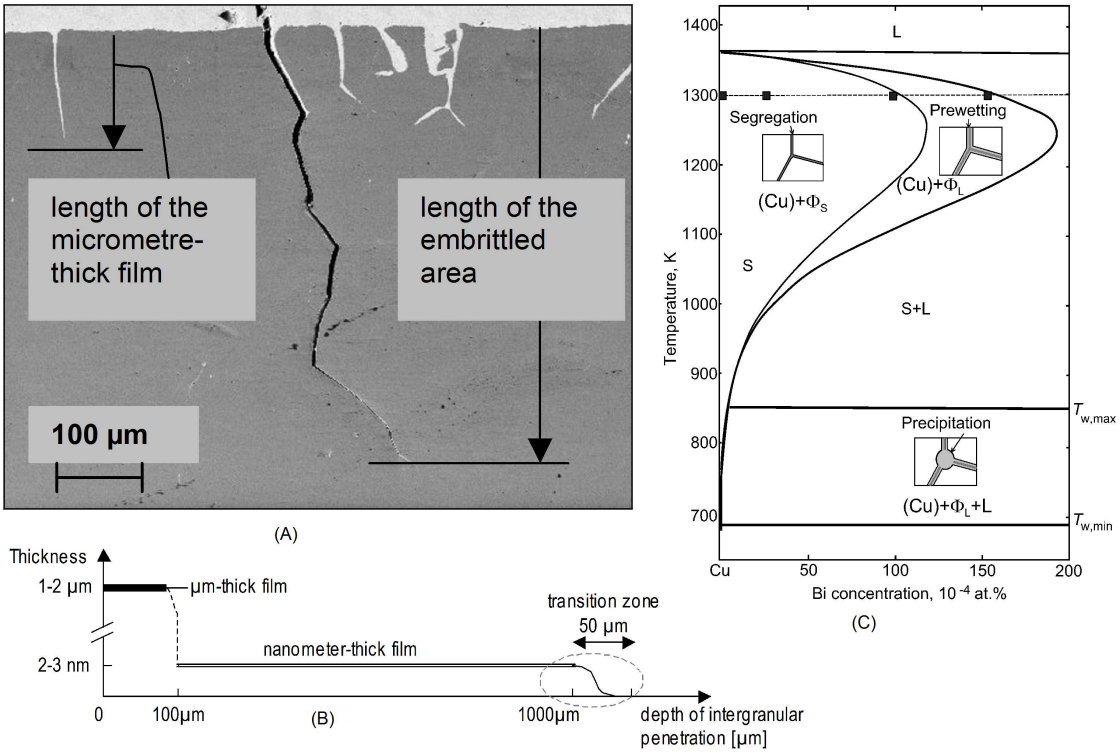

Figure 1.1: (A) Cross-section of a Ni polycrystal in contact with liquid Ni-Bi alloy. Top left region shows a micrometer thick intergranular penetration tip. Middle region shows long crack due to the penetration tip and the nanometrer-thick film. (B) Schematic representation of Bi concentration profile across the fracture surface between the external surface and the ductile core in Ni-Bi system at 700°C. (C) Cu-rich side of the Cu-Bi phase diagram. The thick curve is the (retrograde) bulk solidus line [3]. The thin retrograde curve is the GB solidus line obtained for the Cu-Bi polycrystals [3]. The horizontal lines at $T_{\mathrm{w,max}}$ and $T_{\mathrm{w,min}}$ are GB wetting phase transition tie-lines. (A) and (B) are reprinted from [4] with permission, (C) is reprinted from [5] with permission.

thick quasi-liquid Bi intergranular film (IGF) extends hundreds micrometers ahead the penetration tip when Ni is in contact with liquid Bi-Ni alloy [45], extending the crack depth to several times the length of the penetration tip in bending or tensile

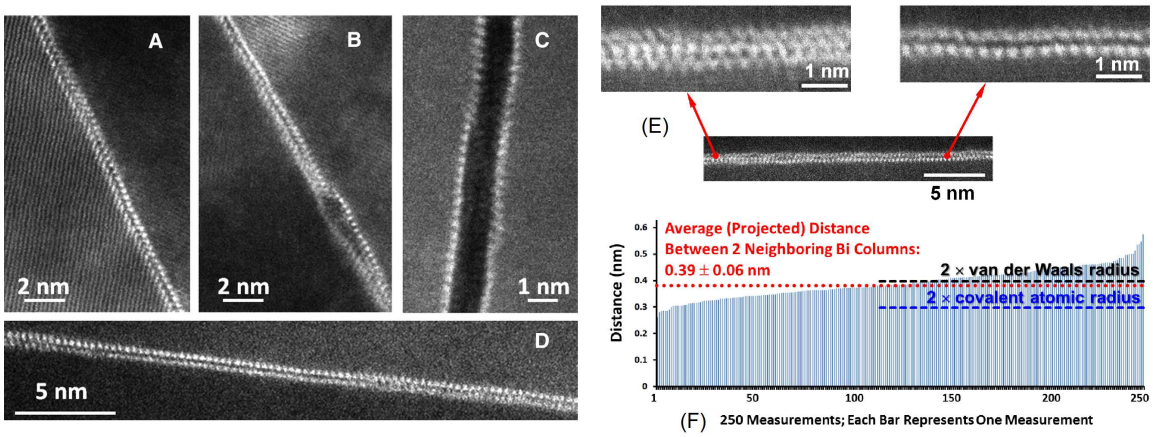

Figure 1.2: (Color online)(A, D) STEM HAADF micrographs showing Bi bilayer complexion. (B, C) Brittle decohesion occurs due to the bilayer complexion. (E) Coexistence of bilayer and trilayer interfacial phases at a single GB, indicating a possible GB phase transition between them. (F) Measured (projected) distances between two neighboring adsorbed Bi atom columns across two adsorbed layers. The large layer spacing (3.9 Å) between Bi layers indicates weak interaction and embrittlement. All panels are reprinted from [6] with permission from AAAS.

tests [42, 4] as shown in Fig. 1.1(A, B). By observing an abrupt change in GB grooving angle [46] and in the temperature dependence of the Bi adsorption [47], people inferred the existence of complexion prewetting transition as shown in Fig. 1.1(C). Moreover, a Bi monolayer complexion on a special Cu GB was observed [39].

Recently, using aberration-corrected high-angle annular dark-field (HAADF) scanning transmission electron microscopy (STEM), Bi (sub)nanometer thick complexions were directly observed at Ni general grain boundaries [6], as shown in Fig. 1.2(A - D). The Bi complexions are mostly bilayers and are ubiquitous at Ni high energy GBs around the penetration tip. Besides the bilayer complexion, a trilayer complexion coexists with a bilayer complexion as shown in Fig. 1.2(E), on a single GB near the penetration tip indicates complexion prewetting transition. The two layers in the Bi bilayer complexions are coherent with the Ni GB planes, but not coherent with

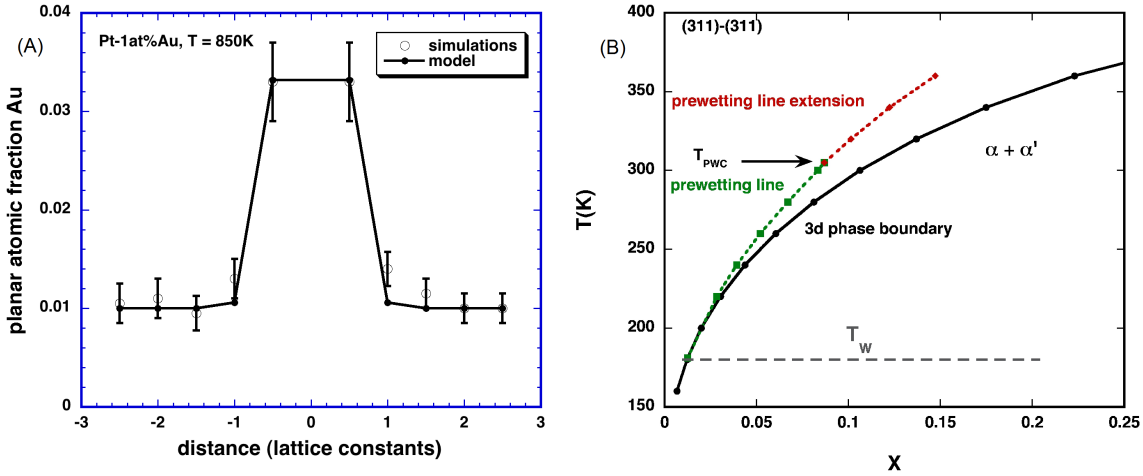

Figure 1.3: (Color online) (A) GB composition of Pt-1 at % Au (100) 43.6^o GB at 850 K Model predicted by model of Wynblatt et al [7] and MC simulation [8]. Error bars on simulation results represent one standard deviation. (B) Portion of the three-dimensional phase diagram for the model alloy with certain parameters, showing superposition of the prewetting line and its extension for a FCC (311)-(311) GB generated by model of Wynblatt et al [9]. (A) is reprinted from [7] with permission and (B) is reprinted from [9] with permission.

each other and have large layer spacing(3.9 Å, Fig. 1.2(F)), which indicates strong Bi-Ni interaction and weak Bi-Bi interlayer interaction. The weak Bi-Bi interlayer interaction could significantly reduce GB cohesion thus lead to embrittlement. The penetration tip and IGF together with the Bi bilayer complexion, could thus explain the LME. Moreover, similar Bi bilayer complexions were observed on Cu general GBs [48]. Besides forming bilayer complexions at GBs, Bi also alters the structure of triple junctions due to the strong reduction of GB energies by segregation [49, 50].

1.2.2 Analytic thermodynamic models

Analytical thermodynamics models of segregation can explain and predict the complexion transitions. Based on the assumption of monolayer adsorption on an interface

with homogeneous adsorption sites, the Langmuir-McLean isotherm [51] shows

$$\frac{X^s}{1-X^s} = \frac{X}{1-X} e^{-\frac{\Delta H_{seg}}{RT}}, \tag{1.1}$$

where X^s and X are the atomic fraction of segregants at the GB and in the bulk respectively. ΔH_{seg} is the molar enthalpy of segregation, R is the universal gas constant, and T is temperature. The model generalizes to a multi-layer GB segregation model [52, 53, 54], where X^i, the atomic fraction of segregates in the ith atomic layer from GB replaces X^s, and the enthalpy of segregation to the ith layer ΔH^i_{seg} replaces ΔH_{seg}. Wynblatt and Ku recognized that ΔH^i_{seg} consists of a chemical contribution [55] which could be derived with bond energy [7] and an elastic contribution that derives from a continuum linear elastic formalism [56]. The model-predicted GB composition profiles [7] agree well with Monte Carlo (MC) simulation [8] as shown in Fig. 1.3(A). The model is capable of producing a phase diagram containing wetting and prewetting complexion transitions as shown in Fig. 1.3(B) [9]. GB layering transitions in bicrystals were studied in [57].

Another approach originates from Cahn's critical point wetting theory [33] which is a phase field model of a binary liquid with a miscibility gap. The model is extended to the binary solid interface [34, 35, 58] where the excess free energy includes: a linear term in misorientation angle, the squared gradient of composition, the square gradient of crystallinity (characterizing the local structural order), and the excess free energy of a material with no misorientation. This extended model can produce GB phase diagrams containing complexion wetting and prewetting transitions in a binary system with a eutectic transition [41]. Multilayer adsorption was also incorporated in later models [59].

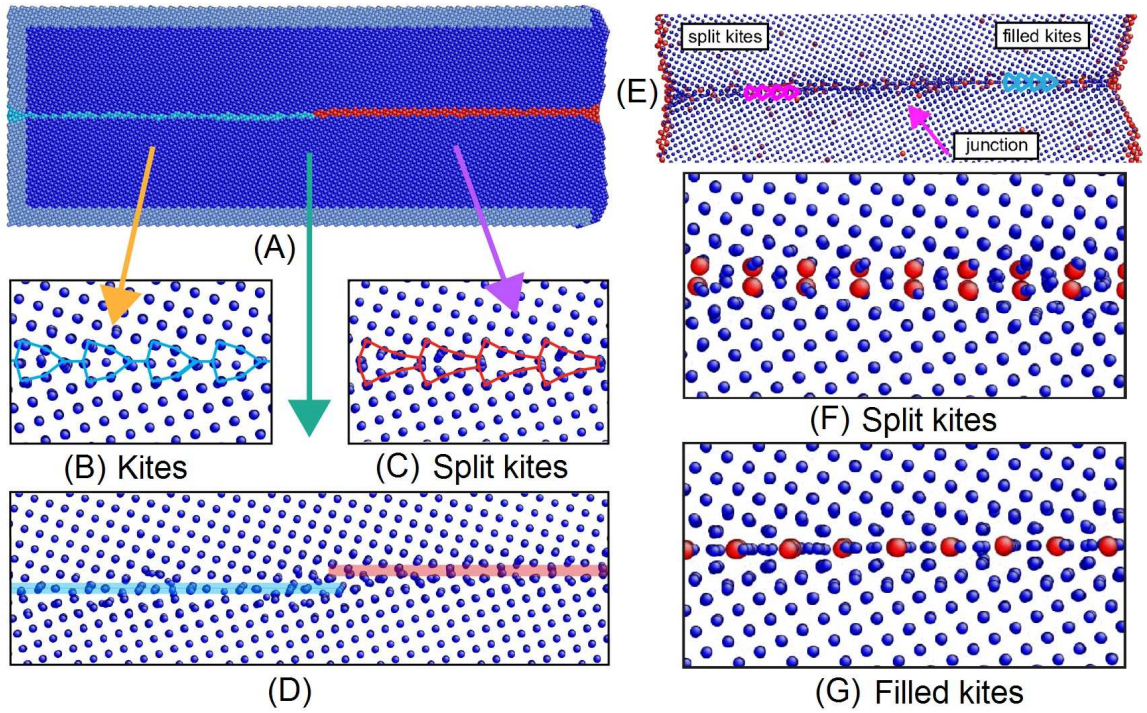

Figure 1.4: (Color online) Complexion transformation of pure Cu Σ5(310) GB and Ag segregated Cu Σ5(120) GB. (A) Coexistance of kites complexion and split kites complexion with the geometry of a wall of fixed atoms at left and an open surface at right. Cu (B) kites and (C) split kites complexion at Cu Σ5(310) and (D) their 1D-phase boundary separation accompanied by a step. (E) Coexistance of spit kites complexion and filled kites complexion with the geometry of open surfaces at both left and right of Ag segregated Cu Σ5(120) GB. Ag segregated Cu (F) split kites and (G) filled kites complexion at Cu Σ5(120). (A-D) is reprinted from [10] with permission. (E-G) is reprinted from [11] with permission.

1.2.3 Molecular dynamics and Monte Carlo simulations of complexion transitions

Complexion transitions can dramatically change material properties [60]. However, since high-temperature GB observation is difficult, no direct complexion transition has been observed so far. Computer simulation of complexion transitions involves the

evolution of $\sim 10^4$ atoms in time scale of tens of nanoseconds which is infeasible with DFT calculations but feasible with less accurate empirical potential methods.

Recently, complexion transitions in pure Cu $\Sigma5(120)$ and $\Sigma5(310)$ were demonstrated with empirical potential methods based molecular dynamics simulation [10], as shown in Fig. 1.4. The authors utilized a new methodology that allows variations in atomic density inside the GB by terminating GB with an open surface at one end and a wall of fixed atoms at the other end. The coexistence of two complexions, kites and split kites, is demonstrated (Fig. 1.4(A)) at 800 K on a $\Sigma5(310)$ GB. A line defect with an atomic scale cross-section separates the two complexions. When terminating the GB with two free surfaces, the whole GB transforms into the split kites at 800 K. On the $\Sigma5(120)$ GB, the reversible complexion transition between split kites at 1000 K and filled kites at 1100 K was shown. Similar simulations with MC and MD [38] directly show that the distinct breaks in the slopes observed in an Arrhenius plot of Ag and Au diffusion in Cu $\Sigma5(310)$ GB [61, 62] are due to a Cu GB complexion transition. The Ag segregation-induced phase transition in Cu $\Sigma5(120)$ GB is also demonstrated [11], as shown in Fig. 1.4.

1.3 Boron Carbide bulk thermodynamics

Boron carbide is an extremely hard and very light material with wide range of applications [63]. Despite its importance, the phase diagram of boron carbide is not precisely known, due to its structural complexity which features 12-atom icosahedra and 3-atom chains, difficulty of equilibration and the small difference between the atomic numbers of boron and carbon. However, DFT is time consuming and scales as the cube of the number of atoms. It is thus generally infeasible to directly use DFT for energy prediction in the Monte Carlo (MC) simulation of phase transitions, which in principle only occurs at infinite cell size and thus require energies very large structures. Interatomic potentials [64], which typically fit the DFT energies as a

function of the positions of the atomic nuclei, can be quickly evaluated to predict approximate energies. We notice that certain interactions in the higher order terms can be included with machine learning (ML) methods such as regression models that can capture complex nonlinear interactions. Our study of boron carbide bulk thermodynamics using DFT, machine learning models and Monte Carlo simulations is shown in Chapter 5.

1.4 Structure of this thesis

This thesis contains 5 following chapters. In Chapter 2, a brief introduction to DFT will be given, including its theoretical foundation, plane-wave implementation, and energy corrections. In Chapter 3, I will present our DFT results of Bi on the Ni(111) surface. Chapter 4 is about Bi at transition metal grain boundaries. Chapter 5 covers our study of boron carbide bulk thermodynamics. I will summarize this thesis and provide perspectives on future directions in Chapter 6.

Chapter 2

First Principle Methods

2.1 Density Functional Theory[1]

2.1.1 Schrodinger equation

At absolute zero temperature, in a periodically repeating quantum system consisting of nuclei and electrons, neglecting spin, relativistic effects and interactions with other systems, the state of the system Φ is determined by the time-independent Schrodinger equation [67],

$$H_{\text{full}}\Phi(\mathbf{R}_1, \mathbf{R}_2, ...\mathbf{R}_{N_c}, \mathbf{r}_1, \mathbf{r}_2, ...\mathbf{r}_N) = E\Phi(\mathbf{R}_1, \mathbf{R}_2, ...\mathbf{R}_{N_c}, \mathbf{r}_1, \mathbf{r}_2, ...\mathbf{r}_N), \tag{2.1}$$

where H_{full} is the Hamiltonian of the system and can be decomposed as,

$$H_{\text{full}} = T_N + T_e + V_{ee} + V_{eN} + V_{NN}, \tag{2.2}$$

where T_N and T_e are the kinetic energies of nuclei and electrons respectively, V_{ee}, V_{eN}, and V_{NN} are the potentials of electron-electron interaction, electron-nucleus

[1] [65] is a good introduction of density functional theory and [66] well introduces its practical usage.

interaction and nucleus-nucleus interaction respectively. More explicitly,

$$T_N = -\sum_{I=1}^{N_c} \frac{\nabla^2_{\mathbf{R}_I}}{2M_I}, \tag{2.3}$$

$$T_e = -\sum_{i}^{N} \frac{\nabla^2_{\mathbf{r}_i}}{2}, \tag{2.4}$$

$$V_{ee} = \sum_{i>j}^{N} \sum_{j}^{N} \frac{1}{|\mathbf{r}_i - \mathbf{r}_j|}, \tag{2.5}$$

$$V_{eN} = -\sum_{i}^{N} \sum_{J}^{N_c} \frac{Z_J}{|\mathbf{r}_i - \mathbf{R}_J|}, \tag{2.6}$$

$$V_{NN} = \sum_{I>J}^{N_c} \sum_{J}^{N_c} \frac{Z_I Z_J}{|\mathbf{R}_I - \mathbf{R}_J|}, \tag{2.7}$$

where we use the atomic units. M_I is the mass of Ith nucleus, $\nabla^2_{\mathbf{R}_I}$ is the Laplacian operator acting on the position of the Ith nucleus $\mathbf{R}_I$, $\nabla^2_{\mathbf{r}_i}$ is the Laplacian operator acting on the position of the ith electron $\mathbf{r}_i$, N_c is the total number of nuclei, N is the total number of electrons, E_n is the energy of the nth state of the system, and $\Phi(\mathbf{R}_1, \mathbf{R}_2, ...\mathbf{R}_{N_c}, \mathbf{r}_1, \mathbf{r}_2, ...\mathbf{r}_N)$ is the wavefunction of the nth state of the system. Due to the periodicity, the energies of the states are quantized.

Since the mass of nucleus is thousands times larger than the mass of electron ($M_I \sim 10^3$), nuclei move much slower than electrons and can be approximated to be stationary when solving the motion of electrons. Thus, we can separate the wavefunction Φ as,

$$\Phi(\mathbf{R}_1, \mathbf{R}_2, ...\mathbf{R}_{N_c}, \mathbf{r}_1, \mathbf{r}_2, ...\mathbf{r}_N) = \Psi(\mathbf{r}_1, \mathbf{r}_2, ...\mathbf{r}_N; \mathbf{R}_1, \mathbf{R}_2, ...\mathbf{R}_{N_c})\chi(\mathbf{R}_1, \mathbf{R}_2, ...\mathbf{R}_{N_c}), \tag{2.8}$$

and treat $\mathbf{R}$'s as constant parameters in Ψ (drop for simplicity below). This is called the Born-Oppenheimer approximation [68].

Based on this approximation, from Eq. (2.1), we can derive that Ψ and χ obey equations,

$$(T_e + V_{ee} + V_{eN})\Psi(\mathbf{r}_1, \mathbf{r}_2, ...\mathbf{r}_N) = \epsilon(\mathbf{R}_1, \mathbf{R}_2, ...\mathbf{R}_{N_c})\Psi(\mathbf{r}_1, \mathbf{r}_2, ...\mathbf{r}_N), \tag{2.9}$$

and

$$(T_N + V_{NN} + \epsilon(\mathbf{R}_1, \mathbf{R}_2, ...\mathbf{R}_{N_c}))\chi(\mathbf{R}_1, \mathbf{R}_2, ...\mathbf{R}_{N_c}) = E\chi(\mathbf{R}_1, \mathbf{R}_2, ...\mathbf{R}_{N_c}). \quad (2.10)$$

In practice, we treat nuclei classically and calculate the total energy of the system E with,

$$E = \epsilon(\mathbf{R}_1, \mathbf{R}_2, ...\mathbf{R}_{N_c}) + \sum_{I>J}^{N_c}\sum_{J}^{N} \frac{Z_I Z_J}{|\mathbf{R}_I - \mathbf{R}_J|}, \quad (2.11)$$

instead of solving Eq. (2.10).

2.1.2 Slater Determinant and Hartree-Fock Energy

To solve the many-electron wavefunction Ψ, one way is to represent it by individual electrons. Since electrons obeys Fermi statistics, namely the wavefunction $\Psi(\mathbf{r}_1, \mathbf{r}_2, ...\mathbf{r}_N)$ changes sign when exchange the positions of any two electrons, $\Psi(\mathbf{r}_1, \mathbf{r}_2, ...\mathbf{r}_N)$ can be approximately written as a Slater determinant [69],

$$\Psi(\mathbf{r}_1, \mathbf{r}_2, ...\mathbf{r}_N) = \frac{1}{\sqrt{N!}} \begin{vmatrix} \psi_1(\mathbf{r}_1) & \psi_1(\mathbf{r}_2) & \dots & \psi_1(\mathbf{r}_N) \\ \psi_2(\mathbf{r}_1) & \psi_2(\mathbf{r}_2) & \dots & \psi_2(\mathbf{r}_N) \\ \dots & \dots & \dots & \dots \\ \psi_N(\mathbf{r}_1) & \psi_N(\mathbf{r}_2) & \dots & \psi_N(\mathbf{r}_N) \end{vmatrix}, \quad (2.12)$$

where $\psi_i(\mathbf{r}_j)$ is the single electron wave function of ith electron at position $\mathbf{r}_j$.

Define the electron Hamiltonian as

$$H = T_e + V_{ee} + V_{eN}. \quad (2.13)$$

By simple manipulation, we can find the electronic energy of the Slater determinant E_{HF}, which is called the Hartree-Fock energy, is

$$\begin{aligned} E_{HF} = \langle\Psi|H|\Psi\rangle &= \sum_{i=1}^{N}\int d^3r[-\frac{\psi_i^*(\mathbf{r})\nabla^2_{\mathbf{r}_i}\psi_i(\mathbf{r})}{2} - \sum_{J}^{N_c}\frac{Z_J|\psi_i(\mathbf{r})|^2}{|r - R_J|}] \\ &+ \frac{1}{2}\sum_{i,j=1}^{N}\int d^3r d^3r'[\frac{|\psi_i(\mathbf{r})|^2|\psi_j(\mathbf{r}')|^2}{|\mathbf{r}-\mathbf{r}'|} - \frac{\psi_i^*(\mathbf{r})\psi_j^*(\mathbf{r}')\psi_j(\mathbf{r})\psi_i(\mathbf{r}')}{|\mathbf{r}-\mathbf{r}'|}] \\ &\equiv T + E_{\text{ext}} + E_{\text{Hartree}} + E_{\text{exchange}}, \end{aligned} \quad (2.14)$$

where we have defined the kinetic energy T, external energy E_{ext}, Hartree energy E_{Hartree} and the exchange energy E_{exchange} as,

$$T = -\sum_{i=1}^{N} \int d^3r \frac{\psi_i^*(\mathbf{r})\nabla^2_{\mathbf{r}_i}\psi_i(\mathbf{r})}{2} \tag{2.15}$$

$$E_{\text{ext}} = -\sum_{i=1}^{N} \int d^3r \sum_{J}^{N_c} \frac{Z_J|\psi_i(\mathbf{r})|^2}{|r - R_J|} \tag{2.16}$$

$$E_{\text{Hartree}} = \frac{1}{2}\sum_{i,j=1}^{N} \int d^3r d^3r' \frac{|\psi_i(\mathbf{r})|^2|\psi_j(\mathbf{r}')|^2}{|\mathbf{r} - \mathbf{r}'|} \tag{2.17}$$

$$E_{\text{exchange}} = -\frac{1}{2}\sum_{i,j=1}^{N} \int d^3r d^3r' \frac{\psi_i^*(\mathbf{r})\psi_j^*(\mathbf{r}')\psi_j(\mathbf{r})\psi_i(\mathbf{r}')}{|\mathbf{r} - \mathbf{r}'|}, \tag{2.18}$$

and the $i = j$ terms in E_{Hartree} and E_{exchange} cancel out. E_{exchange} arises from Fermi statistics and are usually called the Hartree-Fock exact exchange. We will introduce an approximate exchange energy in later subsections.

2.1.3 Hohenberg-Kohn Theorems

Eq. (2.9) has $3N$ variables, which is hard to solve numerically for systems with large N. Hohenberg and Kohn [70] proved that the ground state energy of an interacting electron gas is uniquely determined by its electron density $n(\mathbf{r})$, which is the sum over individual electron densities,

$$n(\mathbf{r}) = \langle\Psi|\sum_{i=1}^{N}\delta(\mathbf{r} - \mathbf{r}_i)|\Psi\rangle = N\int d^3r_2 d^3r_3 ... d^3r_N |\Psi(\mathbf{r}, \mathbf{r}_2, ..., \mathbf{r}_N)|^2. \tag{2.19}$$

$n(\mathbf{r})$ has only 3 variables, much less than $3N$, the number of variables in the many-body wavefunction $\Psi(\mathbf{r}_1, \mathbf{r}_2, ...\mathbf{r}_N)$.

Hohenberg-Kohn Theorem 1: For any system of electrons in an external potential $V_{\text{ext}}(\mathbf{r})$, the potential $V_{\text{ext}}(\mathbf{r})$ is determined up to a constant by the ground state electron density $n_0(\mathbf{r})$.

Proof[2]. Suppose a given electron density $n_0(\mathbf{r})$ corresponds to two different external potentials $V_{\text{ext}}^{(1)}$ and $V_{\text{ext}}^{(2)}$ that differ by more than a constant, leading to two

[2]This proof follows [65].

Hamiltonians $H^{(1)}$ and $H^{(2)}$ respectively. Suppose $|\Psi^{(1)}\rangle$ and $|\Psi^{(2)}\rangle$ are the non-degenerate ground states of $H^{(1)}$ and $H^{(2)}$ respectively, we thus have

$$\begin{aligned} &H^{(1)}|\Psi^{(1)}\rangle = E^{(1)}|\Psi^{(1)}\rangle, \quad H^{(2)}|\Psi^{(2)}\rangle = E^{(2)}|\Psi^{(2)}\rangle \text{ and,} \\ &n_0(\mathbf{r}) = \langle\Psi^{(1)}|\sum_{i=1}^{N}\delta(\mathbf{r}-\mathbf{r}_i)|\Psi^{(1)}\rangle = \langle\Psi^{(2)}|\sum_{i=1}^{N}\delta(\mathbf{r}-\mathbf{r}_i)|\Psi^{(2)}\rangle, \end{aligned} \tag{2.20}$$

where N is the number of electrons in the system.

Thus,

$$E^{(1)} = \langle\Psi^{(1)}|H^{(1)}|\Psi^{(1)}\rangle < \langle\Psi^{(2)}|H^{(1)}|\Psi^{(2)}\rangle. \tag{2.21}$$

Using Eq. (2.19), we have,

$$\langle\Psi^{(2)}|H^{(1)}|\Psi^{(2)}\rangle = E^{(2)} + \int d^3r[V_{\text{ext}}^{(1)}(\mathbf{r}) - V_{\text{ext}}^{(2)}(\mathbf{r})]n_0(\mathbf{r}), \tag{2.22}$$

thus,

$$E^{(1)} < E^{(2)} + \int d^3r[V_{\text{ext}}^{(1)}(\mathbf{r}) - V_{\text{ext}}^{(2)}(\mathbf{r})]n_0(\mathbf{r}). \tag{2.23}$$

With the same argument,

$$E^{(2)} < E^{(1)} + \int d^3r[V_{\text{ext}}^{(2)}(\mathbf{r}) - V_{\text{ext}}^{(1)}(\mathbf{r})]n_0(\mathbf{r}). \tag{2.24}$$

Summing up Eq. (2.23) and Eq. (2.24) we get the contradictory result,

$$E^{(1)} + E^{(2)} < E^{(1)} + E^{(2)}. \qquad \text{Q.E.D.} \tag{2.25}$$

Thus we prove the theorem is true for system with non-degenerate ground state. The proof can be extended to degenerate cases [71].

Hohenberg-Kohn Theorem 2: A universal functional for the electron energy $E[n]$ can be defined in terms of the electron density $n(\mathbf{r})$. The ground state electron density $n_0(\mathbf{r})$ minimizes $E[n]$ globally.

Proof. A general proof can be done with Levy's constrained search formalism [72]. From the variational principle, the ground state energy is

$$E_0 = \min_{\Psi}\langle\Psi|T + V_{ee} + V_{\text{ext}}|\Psi\rangle, \tag{2.26}$$

where V_{ee} is the electron-electron interaction potential. Define $\Psi \to n$ as an all wavefunctions that correspond to a certain electron density $n(\mathbf{r})$. In particular, the ground state corresponds to the electron density $n_0(\mathbf{r})$. The minimization in Eq. (2.26) can be carried out in two steps: first, given electron density $n(\mathbf{r})$, find the wavefunction in all $\Psi \to n$ that minimize energy, and then find $n(\mathbf{r})$ that minimizes energy, which can be written as

$$\begin{aligned} E_0 &= \min_{\Psi} \langle \Psi | T + V_{ee} + V_{\text{ext}} | \Psi \rangle \\ &= \min_{n} \{ \min_{\Psi \to n} \langle \Psi | T + V_{ee} + V_{\text{ext}} | \Psi \rangle \}. \end{aligned} \tag{2.27}$$

Define the functionals

$$F[n] = \min_{\Psi \to n} \langle \Psi | T + V_{ee} | \Psi \rangle, \tag{2.28}$$

$$E[n] = F[n] + \int d^3 r V_{\text{ext}}(\mathbf{r}) n(\mathbf{r}) \tag{2.29}$$

Eq. (2.27) can be written as,

$$\begin{aligned} E_0 &= \min_{n} (F[n] + \int d^3 r V_{\text{ext}}(\mathbf{r}) n(\mathbf{r})) \\ &= \min_{n} E[n] \\ &= E[n_0] \qquad \text{Q.E.D.} \end{aligned} \tag{2.30}$$

2.1.4 Kohn-Sham Ansatz

The fact that $F[n]$ in Eq. (2.29) is unknown prevents density functional theory (Hohenberg-Kohn theorems) from practical calculations. The Kohn-Sham ansatz [73], which assumes the ground state electron density $n_0(\mathbf{r})$ can be represented by the ground state density of an auxiliary system of non-interaction electrons, paves a way to practically use density functional theory. Define the wavefunction of the ith electron in this auxiliary non-interaction system as ψ_i^{KS}, then the electron density and kinetic energy of this auxiliary system are

$$n(\mathbf{r}) = \sum_{i=1}^{N} |\psi_i^{KS}(\mathbf{r})|^2, \tag{2.31}$$

and

$$T[n] = -\frac{1}{2}\sum_{i=1}^{N}\langle\psi_i^{KS}|\nabla^2|\psi_i^{KS}\rangle = \frac{1}{2}\sum_{i=1}^{N}\int d^3r|\nabla\psi_i^{KS}(\mathbf{r})|^2, \tag{2.32}$$

respectively. $T[n]$ is a functional of $n(\mathbf{r})$ due to Hohenberg-Kohn Theorem 2 although it is not written explicitly as a functional of $n(\mathbf{r})$. Define the Hartree energy functional,

$$E_{\text{Hartree}}[n] = \frac{1}{2}\int d^3r d^3r' \frac{n(\mathbf{r})n(\mathbf{r}')}{|\mathbf{r}-\mathbf{r}'|}, \tag{2.33}$$

then the ground state energy functional of the original system (Eq. (2.29)) is

$$E_{KS}[n] = T[n] + \int d^3r V_{\text{ext}}(\mathbf{r})n(\mathbf{r}) + E_{\text{Hartree}}[n] + E_{xc}[n], \tag{2.34}$$

where $E_{xc}[n]$ is the exchange-correlation functional than contains all the many-body interactions. Using the variational principle, together with Eq. (2.31), and the fact the wavefunctions of individual electrons are orthonormalized, we can find the Kohn-Sham Schrodinger-like equation for i^{th} non-interacting electron,

$$[-\frac{1}{2}\nabla^2 + V_{KS}(\mathbf{r})]\psi_i^{KS}(\mathbf{r}) = \epsilon_i^{KS}\psi_i^{KS}(\mathbf{r}), \tag{2.35}$$

where ϵ_i^{KS} is the energy of the ith electron and V_{KS} is the effective potential,

$$V_{KS}(\mathbf{r}) = V_{\text{ext}}(\mathbf{r}) + \int d^3\mathbf{r}' \frac{n(\mathbf{r}')}{|\mathbf{r}-\mathbf{r}'|} + V_{xc}(\mathbf{r}), \tag{2.36}$$

and

$$V_{xc}(\mathbf{r}) \equiv \frac{\delta E_{xc}[n]}{\delta n(\mathbf{r})}. \tag{2.37}$$

2.1.5 Exchange and Correlation Energy

The only unknown term in the Kohn-Sham energy functional Eq. (2.34) and the Kohn-Sham effective single-electron potential Eq. (2.36) is the exchange-correlation energy functional $E_{xc}[n]$. $E_{xc}[n]$ can be further decomposed in to the exchange and the correlation functionals,

$$E_{xc}[n] = E_x[n] + E_c[n]. \tag{2.38}$$

The exchange part $E_x[n]$ arises from the Fermi statistics which imposes the constraint that the total wavefunction of the N electrons must be antisymmetric. As an analogy to the exchange energy in the Hartree-Fock energy Eq. (2.18), the exact exchange energy is

$$E_x[n] = -\frac{1}{2}\sum_{i,j=1}^{N}\int d^3r d^3r' \frac{\psi_i^{KS*}(\mathbf{r})\psi_j^{KS*}(\mathbf{r}')\psi_j^{KS}(\mathbf{r})\psi_i^{KS}(\mathbf{r}')}{|\mathbf{r}-\mathbf{r}'|}, \tag{2.39}$$

which differs from the Hartree-Fock exchange energy only by using different wavefunctions. This exact exchange energy fully characterizes the effect of exchange interaction of Kohn-Sham wavefunctions. However, it cannot be written directly as a simple functional of $n(\mathbf{r})$ and it involves double summation, and is thus computationally expensive. In practice, we usually use an approximate exchange functional rather than this exact exchange. The correlation functional $E_c[n]$ contains other many-body effects due to the approximation of the kinetic energy functional and potential energy functional because of using the Kohn-Sham wavefunctions.

Similar as $T[n]$ and $E_{\text{Hartree}}[n]$, $E_{xc}[n]$ is universal for all systems, and in principle can be precisely known. However, in practice, it involves all the many-body interactions and is too complex to find its exact form. To write $E_{xc}[n]$ as analytic functional of $n(\mathbf{r})$, two types of approximations, local density approximation (LDA) and generalized gradient approximation (GGA) are widely used.

LDA assumes $E_{xc}[n]$ only depends on electron density $n(\mathbf{r})$ at the point $\mathbf{r}$, and ignores its explicit dependence on the variation of n,

$$E_{xc}[n] = \int d^3r n(\mathbf{r})\epsilon_{xc}(n(\mathbf{r})), \tag{2.40}$$

where $\epsilon_{xc}(n(\mathbf{r}))$ is the exchange-correlation energy density, which can be further divide into the exchange density $\epsilon_x(n(\mathbf{r}))$ and $\epsilon_c(n(\mathbf{r}))$ as,

$$\epsilon_{xc}(n(\mathbf{r})) = \epsilon_x(n(\mathbf{r})) + \epsilon_c(n(\mathbf{r})). \tag{2.41}$$

With the approximation that the external potential V_{ext} arises from a uniform positive background, the Kohn-Sham wavefunctions are simply free electrons. In this

case, the exact exchange can be derived as [74]

$$\epsilon_x^{\mathrm{LDA}}(n) = -\frac{3}{4}(\frac{3}{2\pi})^{2/3} n^{1/3}. \tag{2.42}$$

The correlation functional is much harder to find. One widely used functional was proposed by Perdew and Wang [75] (PW92) as

$$\epsilon_c^{\mathrm{PW92}}(x) = -2A(1+\alpha_1 x)\ln[1 + \frac{1}{2A(\beta_1 x^{1/2} + \beta_2 x + \beta_3 x^{3/2} + \beta_4 x^2)}], \tag{2.43}$$

where $x = (3/(4\pi n))^{1/3}$, and A, p, α_1, β_1, β_2, β_3 and β_4 are parameters to fit with the Quantum Monte Carlo simulations [76].

LDA is quite accurate for solids in where electrons are nearly free, but unsatisfactory for atoms and molecules since electrons are more localized in these cases. Thus density functional theory with LDA functionals is widely used in solid state physics but not in chemistry.

GGA assumes that $E_{xc}[n]$ depends on electron density n and its gradient $|\nabla n|$,

$$E_{xc}[n] = \int d^3 r f(n, |\nabla n|). \tag{2.44}$$

In the widely used Perdew, Burke, and Ernzerhof [77](PBE) GGA functional, the exchange functional is

$$E_x^{\mathrm{GGA}} = \int d^3 r n \epsilon_x^{\mathrm{LDA}}(n)[1 + \frac{\kappa \mu s^2}{\kappa + \mu s^2}], \tag{2.45}$$

where $\kappa = 0.804$, $\mu = 0.21951$, and s is a dimensionless density gradient,

$$s = \frac{|\nabla n|}{2(3\pi^2)^{1/3} n^{4/3}}. \tag{2.46}$$

The PBE-GGA correlation functional is

$$E_c[n] = \int d^3 r n[\epsilon_c^{\mathrm{LDA}}(n) + H^{\mathrm{PBE}}(n, |\nabla n|)], \tag{2.47}$$

where H^{PBE} is,

$$H^{\mathrm{PBE}}(n, |\nabla n|) = \ln[1 + \frac{2\alpha}{\beta}\frac{t^2 + At^4}{1 + At^2 + A^2 t^4}], \tag{2.48}$$

where $\alpha = 0.0716$, $\beta = 0.066725$, $t = \frac{|\nabla n|}{2k_s n}$, $k_s = (\frac{4k_F}{\pi})^{1/2}$, $k_F = (3\pi^2 n)^{1/3}$ and $A = 2\alpha/(\beta(\exp[-2\alpha\epsilon_x^{\mathrm{LDA}}(n)/\beta^2] - 1))$.

With the Hohenberg-Kohn theorems, Kohn-Sham ansatz, and the LDA or GGA exchange correlation functionals we can calculate the electron densities, total energies, and various material properties on computers. As an example[3], the difference between the bulk Bi and atomic Bi electron densities is shown in Fig. (2.1), which clearly shows the Bi nearest-neighbor chemical bonding.

2.1.6 Collinear Spin-polarization

For simplicity, all the above derivations are for the non-magnetic case, where the electron densities of both spins are the same. When the ground state is magnetic (for example FCC bulk Ni), we can define the spin-up density $n_\uparrow$ and spin-down density $n_\downarrow$, which is called collinear spin-polarization since all the spins are parallel with each other. Density functional theory and the LDA and GGA functional can be used to calculate the charge densities $n_\uparrow$ and $n_\downarrow$ with just minor modifications. As an example, the density of states of bulk FCC Ni is shown in 2.2.

2.2 Plane-wave Methods

To solve the Kohn-Sham equation Eq. (2.35), we need to represent the wavefunctions and operators in some convenient basis. One commonly used basis is the plane-wave basis which is used in packages like VASP, ABINIT, Quantum ESPRESSO, CASTEP. Alternatively, atom-centered basis is used in packages such as FHI-aims, Gaussian, PLATO, FPLO. Although the Plane-wave basis only works for periodic system, cannot achieve linear scaling and usually takes many more basis functions than atom-centered basis, it can be programmed efficiently, it is easy to take derivatives

[3] All the DFT calculations in this thesis are using the PBE-GGA functional and the plane-wave basis (discussed in next section).

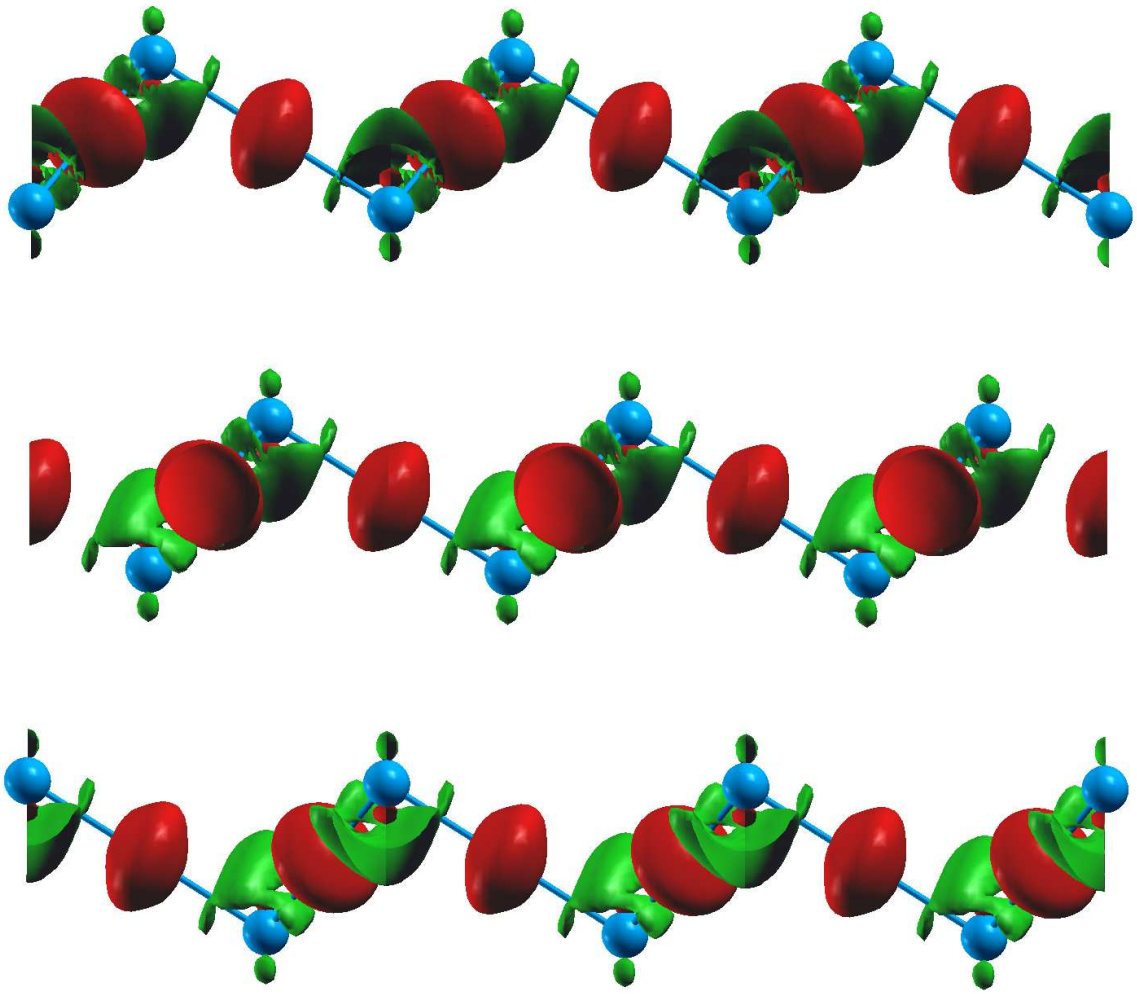

Figure 2.1: Electron density difference between bulk Bi and atomic Bi. Cyan circles are Bi atoms. Electron density isosurface for $0.028|e|/\text{Å}^3$ are plotted. Red is for charge excess and green for charge deficient.

with respect to position, the basis set is independent of the positions of nuclei, and it is easy to control convergence (via cut-off energy). Since we focus on periodic crystal structures, we use VASP to perform DFT calculations. This section introduces the details of plane-wave expansion in solving Khon-Sham equations.

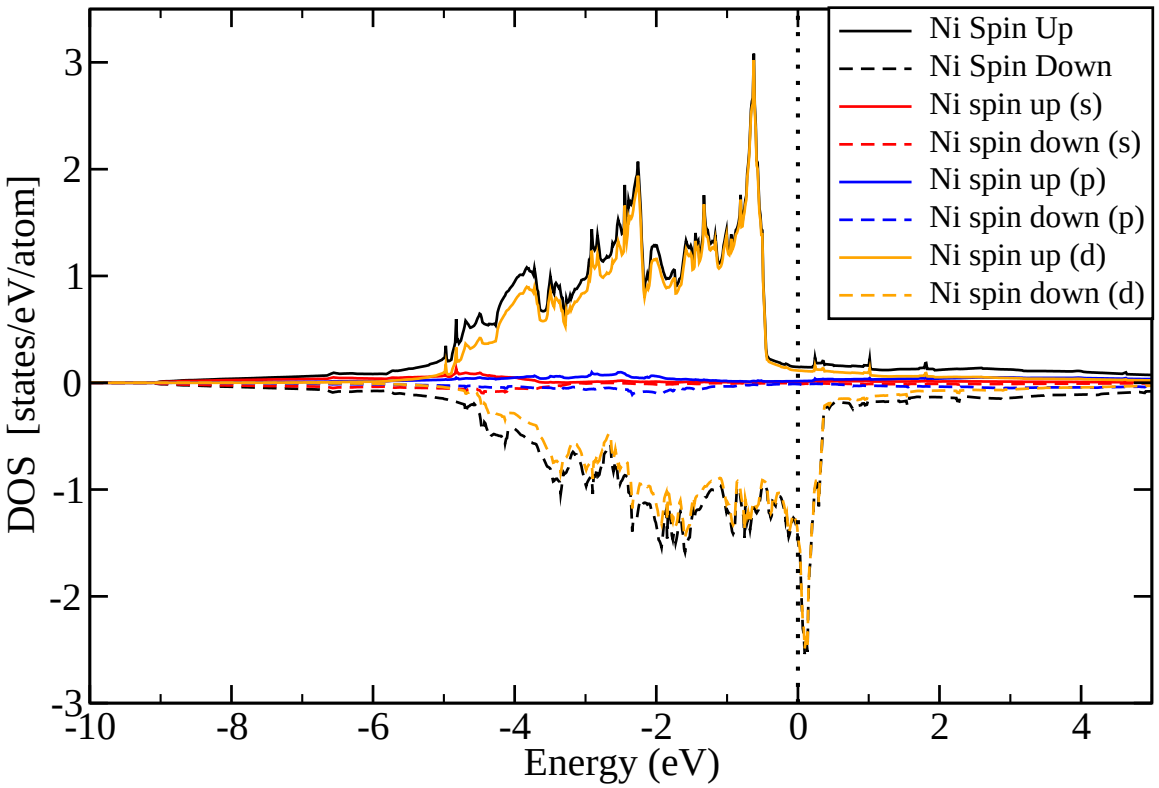

Figure 2.2: Bulk FCC Ni density of states. Solid lines for spin up and dashed lines (y-axis inverted) for spin down. Black for all orbitals, red for s orbitals, blue for p orbitals, and orange for d orbitals. The black dotted line is the Fermi energy.

2.2.1 Plane-wave expansion

For a crystal with three lattice vectors $\mathbf{a}_1$, $\mathbf{a}_2$ and $\mathbf{a}_3$, any potential $V(\mathbf{r})$ acting on electrons in this crystal is periodic,

$$V(\mathbf{r} + \mathbf{a}_i) = V(\mathbf{r}) \tag{2.49}$$

for $i = 1,\ 2$ and 3. The reciprocal space has lattice vectors,

$$\begin{aligned} \mathbf{b}_1 &= 2\pi \frac{\mathbf{a}_2 \times \mathbf{a}_3}{\mathbf{a}_1 \cdot (\mathbf{a}_2 \times \mathbf{a}_3)} \\ \mathbf{b}_2 &= 2\pi \frac{\mathbf{a}_3 \times \mathbf{a}_1}{\mathbf{a}_1 \cdot (\mathbf{a}_2 \times \mathbf{a}_3)} \\ \mathbf{b}_3 &= 2\pi \frac{\mathbf{a}_1 \times \mathbf{a}_2}{\mathbf{a}_1 \cdot (\mathbf{a}_2 \times \mathbf{a}_3)}. \end{aligned} \tag{2.50}$$

The first Brillouin zone is the Wigner-Seitz cell of the primitive cell in the reciprocal space. As an example, the first Brillouin zone of a face-centered cubic (FCC) crystal is shown in Fig. (2.3).

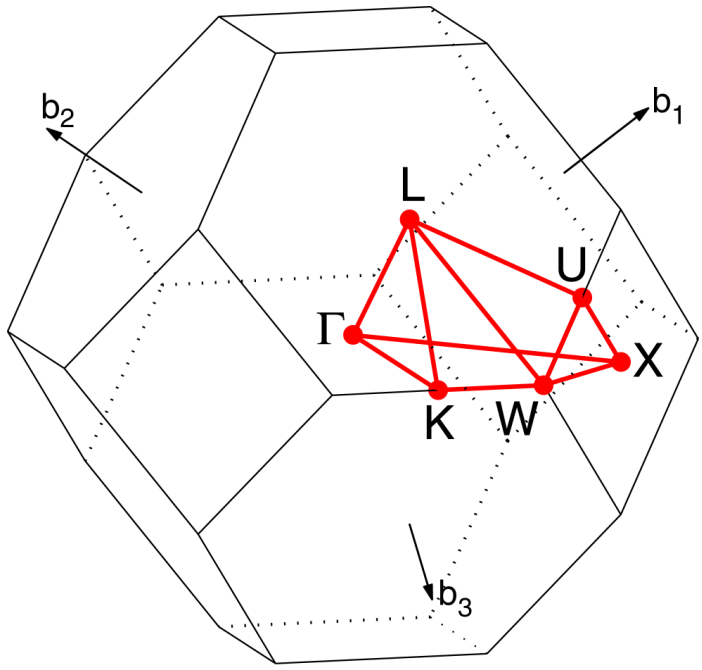

Figure 2.3: The first Brillouin zone of face-centered cubic (FCC) crystal. The labels on the figure are the special symmetric points. Reprinted from Wikipedia website.

The Bloch's theorem [78] states that the wavefunction of an electron in a periodical potential can be written as the product of a free-electron wave and a periodic function

$$\psi_{\mathbf{k}}(\mathbf{r}) = e^{i\mathbf{k}\cdot\mathbf{r}} u(\mathbf{r}), \tag{2.51}$$

where $u(\mathbf{r})$ has same periodicity as the potential.

For a crystal with three reciprocal lattice vectors $\mathbf{b}_1$, $\mathbf{b}_2$ and $\mathbf{b}_3$, it is easy to see that $\psi_{\mathbf{k}+\mathbf{b}_i}(\mathbf{r}) = \psi_{\mathbf{k}}(\mathbf{r})$ for $i = 1,\ 2$ and 3. Thus we just need to solve for the wavefunctions in the first Brillouin zone.

One way to solve the Kohn-Sham equation Eq. (2.35) is to expand it in a plane wave basis to transform it into a matrix equation and then solve it iteratively.

Define the basis wavefunction, $|\mathbf{G_m}\rangle$ which satisfies

$$\langle \mathbf{r}|\mathbf{G_m}\rangle = \frac{1}{\sqrt{\Omega}} e^{i\mathbf{G_m}\cdot\mathbf{r}}, \tag{2.52}$$

where $\Omega = \mathbf{a}_1 \cdot (\mathbf{a}_2 \times \mathbf{a}_3)$ is the volume of the primitive cell, $\mathbf{G_m} = m_1\mathbf{b}_1 + m_2\mathbf{b}_2 + m_3\mathbf{b}_3$ for any integer m_1, m_2 and m_3, and $|\mathbf{r}\rangle$ is the real space basis satisfying

$$\langle \mathbf{r}|\mathbf{r}'\rangle = \delta(\mathbf{r}-\mathbf{r}') \quad \text{, and } \int d^3r |\mathbf{r}\rangle\langle\mathbf{r}| = I, \tag{2.53}$$

where I is the identity operator. We can easily see,

$$\langle \mathbf{G_m}|\mathbf{G_n}\rangle = \delta_{\mathbf{m},\mathbf{n}} \quad \text{, and } \sum_{\mathbf{m}} |\mathbf{G_m}\rangle\langle\mathbf{G_m}| = I. \tag{2.54}$$

Any potential can be expanded as

$$V(\mathbf{r}) = \sum_{\mathbf{m}} V(\mathbf{G_m}) e^{i\mathbf{G_m}\cdot\mathbf{r}}. \tag{2.55}$$

Due to Bloch's theorem, the jth Kohn-Sham wavefunction with wave vector $\mathbf{k}$, $\psi_{j,\mathbf{k}}$ can be written as

$$\psi_{j,\mathbf{k}}(\mathbf{r}) = \frac{1}{\sqrt{\Omega}} \sum_{\mathbf{m}} c_{j,\mathbf{m}}(\mathbf{k}) e^{i(\mathbf{k}+\mathbf{G_m})\cdot\mathbf{r}}. \tag{2.56}$$

The corresponding charge density is

$$\begin{aligned} n(\mathbf{r}) &= \sum_j \int d^3k \langle \psi_{j,\mathbf{k}}|\psi_{j,\mathbf{k}}\rangle \\ &= \frac{1}{\Omega} \int d^3k \sum_j \sum_{\mathbf{m}',\mathbf{m}''} c^*_{j,\mathbf{m}'}(\mathbf{k}) c_{j,\mathbf{m}''}(\mathbf{k}) e^{i(\mathbf{G_{m''}}-\mathbf{G_{m'}})\cdot\mathbf{r}} \\ &\equiv \int d^3k \sum_{j,\mathbf{m}} n_{j,\mathbf{m}}(\mathbf{k}) e^{i\mathbf{G_m}\cdot\mathbf{r}}, \end{aligned} \tag{2.57}$$

where

$$n_{j,\mathbf{m}}(\mathbf{k}) = \frac{1}{\Omega} \sum_{\mathbf{m}'} c^*_{j,\mathbf{m}'}(\mathbf{k}) c_{j,\mathbf{m}'+\mathbf{m}}(\mathbf{k}). \tag{2.58}$$

Left product the Schrodinger equation

$$H|\psi_{j,\mathbf{k}}\rangle = \epsilon_j(\mathbf{k})|\psi_{j,\mathbf{k}}\rangle \tag{2.59}$$

with any basis $\langle \mathbf{k}+\mathbf{G_n}|$, we have

$$\sum_{\mathbf{m}} H_{\mathbf{n},\mathbf{m}}(\mathbf{k}) c_{j,\mathbf{m}}(\mathbf{k}) = \epsilon_j(\mathbf{k}) c_{j,\mathbf{n}}(\mathbf{k}), \tag{2.60}$$

where

$$H_{\mathbf{n},\mathbf{m}}(\mathbf{k}) = \frac{1}{2}|\mathbf{k}+\mathbf{G_m}|^2 \delta_{\mathbf{n},\mathbf{m}} + V(\mathbf{G_m}-\mathbf{G_n}). \tag{2.61}$$

Thus we have shown how to represent the Kohn-Sham equation and the electron density $n(\mathbf{r})$ with the plane wave basis. The procedure of finding the ground state charge density and Kohn-Sham wavefunctions is:

1. Initially guess $n_{j,\mathbf{m}}(\mathbf{k})$.
2. Calculate potential (need $n_{j,\mathbf{m}}(\mathbf{k})$) and Hamiltonian from Eq. (2.61).
3. Solve Eq. (2.60) to find $c_{j,\mathbf{m}}(\mathbf{k})$.
4. Calculate electron density $n_{j,\mathbf{m}}(\mathbf{k})$.

repeat 2-4 until convergence.

In all our previous derivations we use the infinite basis set $\{|\mathbf{G_m}\rangle\}$ and infinitely many wave vectors $\{\mathbf{k}\}$ in the first Brillouin zone. However, to perform numerical calculations on computers, we need to make them finite. For the $\{\mathbf{k}\}$, we just need to sample some discrete points in the first irreducible Brillouin zone, which is the region inside the red lines in Fig. (2.3) for FCC crystal. For the basis set $\{|\mathbf{G_m}\rangle\}$, in practice people truncate it up to a certain cutoff energy E_{cut} on the order of hundreds eV, namely just expand with basis satisfying

$$\frac{\hbar^2|\mathbf{k}+\mathbf{G}|^2}{2m} < E_{\text{cut}}. \tag{2.62}$$

2.2.2 Pseudopotentials

The truncation of plane-wave basis is reliable if all physical quantities are spatially slow varying. However, the external Coulomb potential due to nuclei has the form $1/r$ which divergences and changes rapidly near the cores. This causes the wavefunctions of inner shell electrons and the near-core part of the wavefunctions of valance electrons to wiggle rapidly. Thus a direct computation with all electrons and Coulomb

external potential needs a large number of plane-wave basis and is very computationally expensive. Luckily, only the away-from-core part of the wavefunctions of valance electrons participate bonding and thus determines the material properties. In practice, people first used a frozen core approximation that only calculates the valance electrons under the fixed effective external potential of the nuclei and the inner shell electrons. Directly using this effective potential still leaves the wavefunctions of valance electrons wiggling near the cores, which is hard to calculate and anyways not interesting. People then learned to alter the effective potential to maintain good behavior of valence electrons away from the core while making it slowly varying near the core. This modified effective potential is called a pseudopotential. A sketch of the pseudopotential is shown in 2.4. In practice, every element has a pseudopotential which can be used in any chemical environment.

2.2.3 Force on Nuclei and Relaxation

Given an initial structure containing certain atoms, one important goal is to find the stable structure after relaxation. This is achieved by moving nuclei under the influence of electrons and other nuclei. Since nuclei are very massive, they are typically treated classically,

$$\mathbf{F}_i = \frac{\partial E}{\partial \mathbf{R}_i} = -\langle \Psi | \frac{\partial H}{\partial \mathbf{R}_i} | \Psi \rangle + \frac{\partial V_{II}}{\partial \mathbf{R}_i}, \tag{2.63}$$

where $\mathbf{R}_i$ is the coordinate of ith nucleus, $\mathbf{F}_i$ is the force on i^{th} nucleus, $|\Psi\rangle$ is the wave-function of all valance electrons, H is the Kohn-Sham Halmitonian of electrons, and V_{II} is the Coulomb interaction potential between ions.

One simple procedure of performing the structural relaxation is as follows,

1. Initialize the positions of the nuclei.

2. Calculate the ground state electron density $n_0(\mathbf{r})$ using the procedure in Subsection 2.2.3.

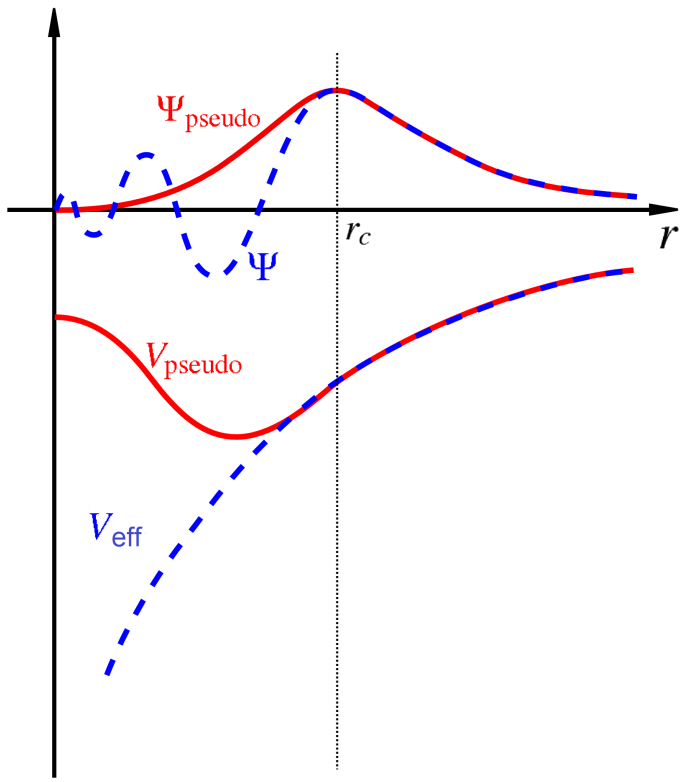

Figure 2.4: Sketch of the effective potential of the nucleus and inner-shell electrons V_{eff} and corresponding wavefunction Ψ (blue), and the pseudopotential V_{pseudo} and corresponding wavefunction Ψ_{pseudo} (red). The Ψ_{pseudo} and V_{pseudo} are the same as Ψ and V_{eff} respectively outside the distance r_c. Adapted and modified from Wikipedia.

3. Calculate the forces on every nucleus. Move nuclei slightly in the direction of the force on them[4].

Repeat 2 and 3 until the convergence of total energy.

2.3 Corrections to Total Energy

2.3.1 Spin-orbit Coupling[5]

[4]In practice, the conjugate gradient algorithm is usually used to move the atoms [79].

[5]In this subsection we use the SI units to emphasize coupling, electron mass, etc. The derivations

Spin-orbit coupling is not included in basic DFT calculations. However, it is especially important for heavy atoms since it scales roughly as the square of the atomic number [80]. It can also strongly alter the band structures of heavy metals. An example is shown for Bi in Fig. (2.5) where DFT correctly predicts the electron pocket around Γ with SOC correction but is incorrect without SOC correction.

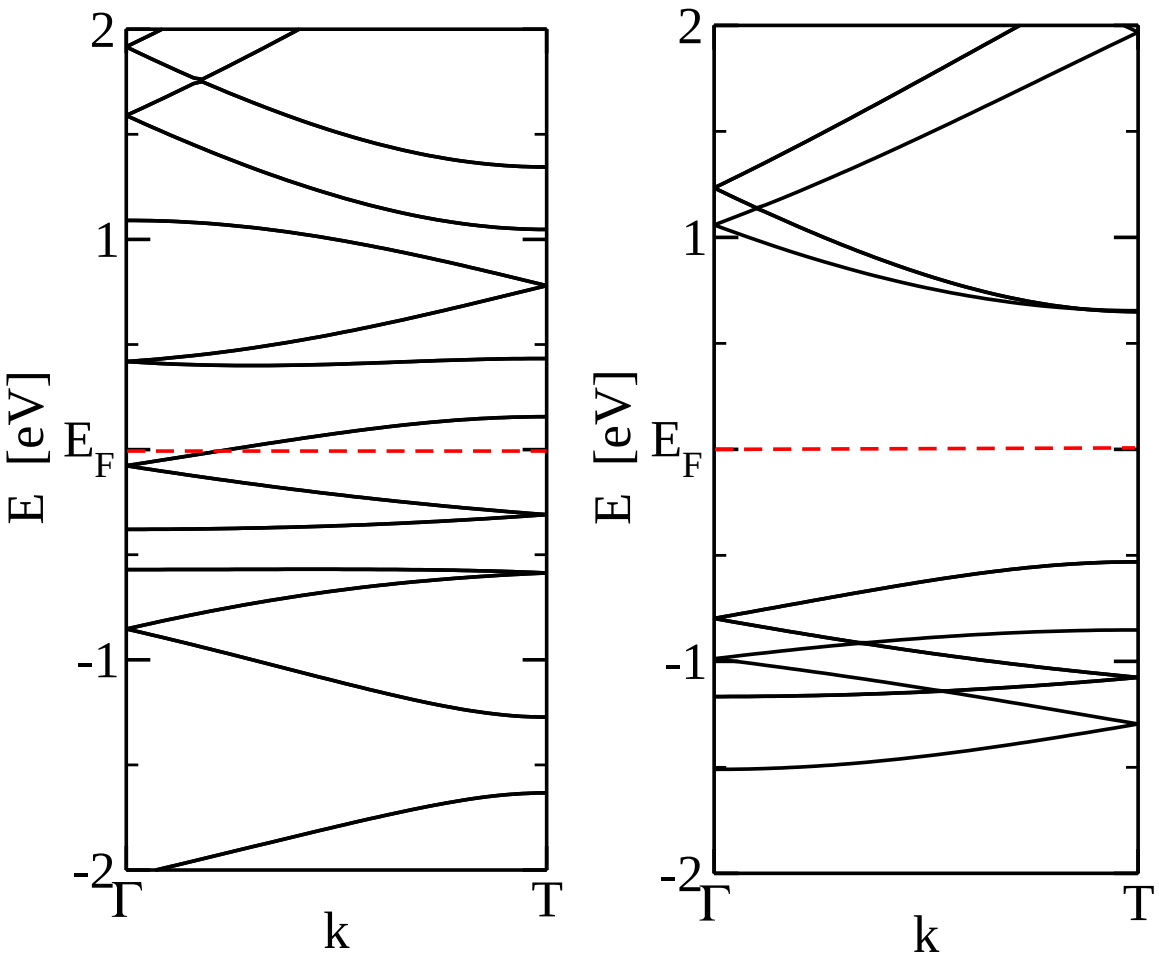

Figure 2.5: Band structure of Bi along the Γ-T direction in its Brillouin zone [12]. Left is calculated with spin-orbital coupling, right without.

The spin-orbit coupling term can be derived from Dirac Equation [81] for a free

follow the lecture note of Charlotte Elster.

electron with inertial mass m,

$$(i\hbar\gamma^\mu\partial_\mu - mc)\psi(x) = 0, \tag{2.64}$$

where $\partial_\mu = \partial/\partial x^\mu$ for $\mu = 0,\ 1,\ 2,\ 3$, $x^0 = ct$, c is the speed of light. The Einstein summation convention and the Minkowski metric are used, $\gamma^\mu\partial_\mu = -\gamma^0\partial_0 + \gamma^1\partial_1 + \gamma^2\partial_2 + \gamma^3\partial_3$. γ^μ's are the Dirac matrices,

$$\gamma^0 = \begin{bmatrix} I_{2\times 2} & 0 \\ 0 & -I_{2\times 2} \end{bmatrix},\ \gamma^k = \begin{bmatrix} 0 & \sigma_k \\ -\sigma_k & 0 \end{bmatrix},\ \text{for } k = 1, 2, 3. \tag{2.65}$$

σ_k's are the Pauli matrices,

$$\sigma_1 = \begin{bmatrix} 0 & 1 \\ 1 & 0 \end{bmatrix},\ \sigma_2 = \begin{bmatrix} 0 & -i \\ i & 0 \end{bmatrix},\ \sigma_3 = \begin{bmatrix} 1 & 0 \\ 0 & -1 \end{bmatrix}. \tag{2.66}$$

The electron interacts with electromagnetic field $A_\mu = (\varphi,\ c\mathbf{A})$, where φ is the electric potential and $\mathbf{A}$ is the magnetic potential, through minimal coupling,

$$[\gamma^\mu(i\hbar\partial_\mu - \frac{e}{c}A_\mu) - mc]\psi(x) = 0, \tag{2.67}$$

which is gauge invariant. Rewrite the wavefunction $\psi(x)$ as

$$\psi(x) = e^{-imc^2t/\hbar}\begin{bmatrix} \Psi(x) \\ \chi(x) \end{bmatrix} \tag{2.68}$$

and plug in Eq. (2.67) to get

$$i\hbar\frac{\partial\Psi(x)}{\partial t} = c\boldsymbol{\sigma}\cdot(\mathbf{p} - e\mathbf{A})\chi(x) + e\varphi\Psi(x) \tag{2.69}$$

$$i\hbar\frac{\partial\chi(x)}{\partial t} = c\boldsymbol{\sigma}\cdot(\mathbf{p} - e\mathbf{A})\Psi(x) - (2mc^2 - e\varphi)\chi(x). \tag{2.70}$$

When an electron moves with speed $v << c$ in a weak electromagnetic field $e\varphi << mc^2$,

$$\left|i\hbar\frac{\partial\chi(x)}{\partial t}\right| \approx \frac{1}{2}mv^2 << (2mc^2 - e\varphi)|\chi|. \tag{2.71}$$

Thus Eq. (2.70) becomes

$$\chi = \frac{c\boldsymbol{\sigma}\cdot(\mathbf{p}-e\mathbf{A})}{2mc^2-e\varphi}\Psi \approx \frac{1}{2mc^2}(1+\frac{e}{2mc^2}\varphi)c\boldsymbol{\sigma}\cdot(\mathbf{p}-e\mathbf{A})\Psi, \tag{2.72}$$

where the approximation is due to a Taylor expansion to first order in $e\varphi/(mc^2)$. Plugging Eq. (2.72) into Eq. (2.70), we get,

$$i\hbar\frac{\partial\Psi(x)}{\partial t} = \frac{1}{2m}\boldsymbol{\sigma}\cdot(\mathbf{p}-e\mathbf{A})(1+\frac{e}{2mc^2}\varphi)\boldsymbol{\sigma}\cdot(\mathbf{p}-e\mathbf{A})\Psi + e\varphi\Psi \tag{2.73}$$

Using the property of Pauli matrices,

$$(\boldsymbol{\sigma}\cdot\mathbf{W})(\boldsymbol{\sigma}\cdot\mathbf{W}) = \mathbf{W}^2 + i\boldsymbol{\sigma}\cdot(\mathbf{W}\times\mathbf{W}), \tag{2.74}$$

for any vector $\mathbf{W}$, and noting

$$\begin{aligned}(\mathbf{p}-e\mathbf{A})\times(\mathbf{p}-e\mathbf{A})\Psi &= -\frac{e}{i}[\nabla\times\mathbf{A}+\mathbf{A}\times\nabla]\Psi \\ &= -\frac{e\hbar}{i}[(\nabla\times\mathbf{A})\Psi+\nabla\Psi\times\mathbf{A}+\mathbf{A}\times\nabla\Psi] \\ &= -\frac{e\hbar}{i}\mathbf{B}\Psi,\end{aligned} \tag{2.75}$$

where $\mathbf{B}=\nabla\times\mathbf{A}$ is the magnetic field, we get,

$$\frac{1}{2m}\boldsymbol{\sigma}\cdot(\mathbf{p}-e\mathbf{A})\boldsymbol{\sigma}\cdot(\mathbf{p}-e\mathbf{A}) = \frac{1}{2m}(\mathbf{p}-e\mathbf{A})^2 - \frac{eg}{2m}\mathbf{S}\cdot\mathbf{B}, \tag{2.76}$$

where $g=2$ is the g-factor of the electron and $\mathbf{S}=\hbar\boldsymbol{\sigma}/2$ is the spin operator.

Neglecting the second and higher orders of potential, we have

$$\begin{aligned}\frac{e}{4m^2c^2}\boldsymbol{\sigma}\cdot(\mathbf{p}-e\mathbf{A})\varphi\boldsymbol{\sigma}\cdot(\mathbf{p}-e\mathbf{A}) &\approx \frac{e}{4m^2c^2}\boldsymbol{\sigma}\cdot\mathbf{p}\varphi\boldsymbol{\sigma}\cdot\mathbf{p} = \frac{e}{4m^2}\sigma_k\sigma_l p_k\varphi p_l \\ &= \frac{e}{4m^2c^2}(p_k\varphi p_k + i\epsilon_{klm}\sigma_m p_k\varphi p_l)\end{aligned} \tag{2.77}$$

where in the last equality we use the property of Pauli matrices,

$$\sigma_k\sigma_l = \delta_{kl} + i\epsilon_{klm}\sigma_m. \tag{2.78}$$

Moreover,

$$i\epsilon_{klm}\sigma_m p_k\varphi p_l = i\epsilon_{klm}\sigma_m(p_k\varphi)p_l + i\epsilon_{klm}\sigma_m\varphi p_k p_l = i\epsilon_{klm}\sigma_m(p_k\varphi)p_l = \boldsymbol{\sigma}\cdot(\nabla\varphi\times\mathbf{p}). \tag{2.79}$$

Assuming the electric potential is rotationally invariant (i.e. the Coulomb potential), we have

$$\nabla\varphi = \frac{d\varphi}{dr}\frac{\mathbf{r}}{r}. \tag{2.80}$$

Since $\mathbf{L} = \mathbf{r} \times \mathbf{p}$, pluging Eq. (2.79) in Eq. (2.77) and combining with Eq. (2.76), Eq. (2.73) can be written as

$$i\hbar\frac{\partial\Psi}{\partial t} = (\frac{(\mathbf{p} - e\mathbf{A})^2}{2m} + V(r) - \frac{eg}{2m}\mathbf{S}\cdot\mathbf{B} + \frac{1}{2m^2c^2r}\frac{dV(r)}{dr}\mathbf{L}\cdot\mathbf{S})\Psi, \tag{2.81}$$

where $V(r) = e\varphi$. Thus we obtain the spin-orbit coupling term,

$$H_{\text{SOC}} = \frac{1}{2m^2c^2r}\frac{dV(r)}{dr}\mathbf{L}\cdot\mathbf{S}, \tag{2.82}$$

which is treated perturbatively in practical calculations.

We have omitted the term proportional to $p_k\varphi p_k$ which is a relativistic correction of the order $(v/c)^2$ that does not have a non-relativistic correspondence and arises due to corrections in this order are not fully considered in our approximations. A full treatment of the non-relativistic approximation of Dirac equation for spin-half particles can be done with the Foldy-Wouthuysen transformation [82] which is outside the scope of this thesis.

2.3.2 Temperature corrections

Density functional theory can accurately calculate the total energy of a structure at the absolute zero temperature $T = 0$ K. To obtain the total energy of a structure at finite temperature, corrections like vibrational free energy and electronic free energy are needed.

Vibrational free energy F_{vib} comes from the vibration of nuclei at finite temperature. For a vibrational mode with natural frequency ω, its energy levels are

$$E_n = (n + \frac{1}{2})\hbar\omega, \tag{2.83}$$

where $n = 0,\ 1,\ 2, ...$

The partition function of this mode is

$$Z_\omega = \sum_{n=0}^{\infty} e^{-E_n/k_B T} = \frac{1}{2\sinh(\hbar\omega/2k_B T)}\ , \tag{2.84}$$

where k_B is the Boltzman constant. The vibrational free energy of this particular mode is,

$$F_\omega = -k_B T \ln Z_\omega = k_B T \ln[2\sinh(\hbar\omega/2k_B T)]. \tag{2.85}$$

For a structure with mode (phonon) density of states $g(\omega)$, the vibrational free energy is the sum of the contribution of all modes,

$$F_{\text{vib}} = k_B T \int g(\omega) \ln[2\sinh(\hbar\omega/2k_B T)] d\omega. \tag{2.86}$$

Density functional theory can be used to accurately determine the phonon density of states $g(\omega)$ through the force constant method [83]. Due to the periodicity of the crystal, the position of Ith atom $\mathbf{R}_I$ can be decomposed as,

$$\mathbf{R}_I = \mathbf{T}_l + \mathbf{v}_s, \tag{2.87}$$

where $\mathbf{T}_l = l_1\mathbf{a}_1 + l_2\mathbf{a}_2 + l_3\mathbf{a}_3$, and $\mathbf{v}_s$ is the relative position of Ith atom in the unit cell containing it. $\mathbf{R}_I$ can be labeled as $\mathbf{R}_{l,s}$ and its α's coordinate is $R_{l,s,\alpha}$.

Under the harmonic approximation,

$$\begin{aligned} E &\approx E_0 + \frac{1}{2}\sum_{l,m,s,t\alpha,\beta} \Delta R_{l,s,\alpha} D_{(s,\alpha),(t,\beta)}(\mathbf{T}_l, \mathbf{T}_m) \Delta R_{m,t,\beta} \\ &= E_0 + \frac{1}{2}\sum_{l,m,s,t\alpha,\beta} \Delta v_{l,s,\alpha} D_{(s,\alpha),(t,\beta)}(\mathbf{T}_l, \mathbf{T}_m) \Delta v_{m,t,\beta} \end{aligned} \tag{2.88}$$

where E_0 is the energy of the fully relaxed structure, $\Delta R_{l,s,\alpha}$ and $\Delta R_{\beta,j,n}$ are the small derivation of $R_{l,s,\alpha}$ and $R_{\beta,j,n}$ from their relaxed position respectively, and

$$D_{(s,\alpha),(t,\beta)}(\mathbf{T}_l, \mathbf{T}_m) = \frac{\partial^2 E}{\partial R_{l,s,\alpha} \partial R_{m,t,\beta}}|_{\text{relaxed position}}. \tag{2.89}$$

Due to translational symmetry,

$$D_{(s,\alpha),(t,\beta)}(\mathbf{T}_l, \mathbf{T}_m) = D_{(s,\alpha),(t,\beta)}(\mathbf{T}_l - \mathbf{T}_m, 0) \equiv D_{(s,\alpha),(t,\beta)}(\mathbf{T}_l - \mathbf{T}_m). \tag{2.90}$$

Perform the Fourier transformation,

$$D_{(s,\alpha),(t,\beta)}(\mathbf{q}) = \frac{1}{\sqrt{M_i M_j}} \sum_{\mathbf{T}} D_{(s,\alpha),(t,\beta)}(\mathbf{T}) e^{-i\mathbf{q}\cdot\mathbf{T}} \tag{2.91}$$

for phonon wavevector $\mathbf{q}$'s in its first Brillouin zone.

The phonon frequencies can be found by solving the eigenvalue problems

$$\sum_{t,\beta} D_{(s,\alpha),(t,\beta)}(\mathbf{q}) \mathbf{U}_{t,\beta}(\mathbf{q}) = \omega(\mathbf{q})^2 \mathbf{U}_{s,\alpha}(\mathbf{q}). \tag{2.92}$$

We thus obtain phonon density in Eq. (2.86) as

$$g(\omega) = \int d^3q \delta(\omega - \omega_{\mathbf{q}}), \tag{2.93}$$

where the integration is taken inside the first Brillouin zone.

In theory due to the interactions between atoms and the conservation of momentum, we need to calculate an infinite cell to obtain exact phonon results. In practice, this is not practical and usually a large supercell ($\sim$ 10 Å) is enough to get convergent results. An example of the calculated phonon density and vibrational free energy of FCC bulk Ni is shown in Fig. (2.6) and Fig. (2.7).

Since we can obtain electron density $D(E)$ from DFT, as shown in Fig. (2.2), it is easy to calculate the electronic free energy. Electrons occupy states with probability given by the Fermi-Dirac occupation function,

$$f(E,T) = \frac{1}{1 + \exp[(E-\mu)/k_B T]}, \tag{2.94}$$

where E is the energy of the state and μ is the chemical potential of electrons which is usually approximated by the Fermi energy E_F. The free energy correction is,

$$\Delta F_e(T) = \Delta U_e(T) - T S_e(T), \tag{2.95}$$

where the correction of inner energy $\Delta U_e(T)$ is,

$$\Delta U_e(T) = \int dE D(E)(E - E_F)(f(E,T) - f(E,0)), \tag{2.96}$$

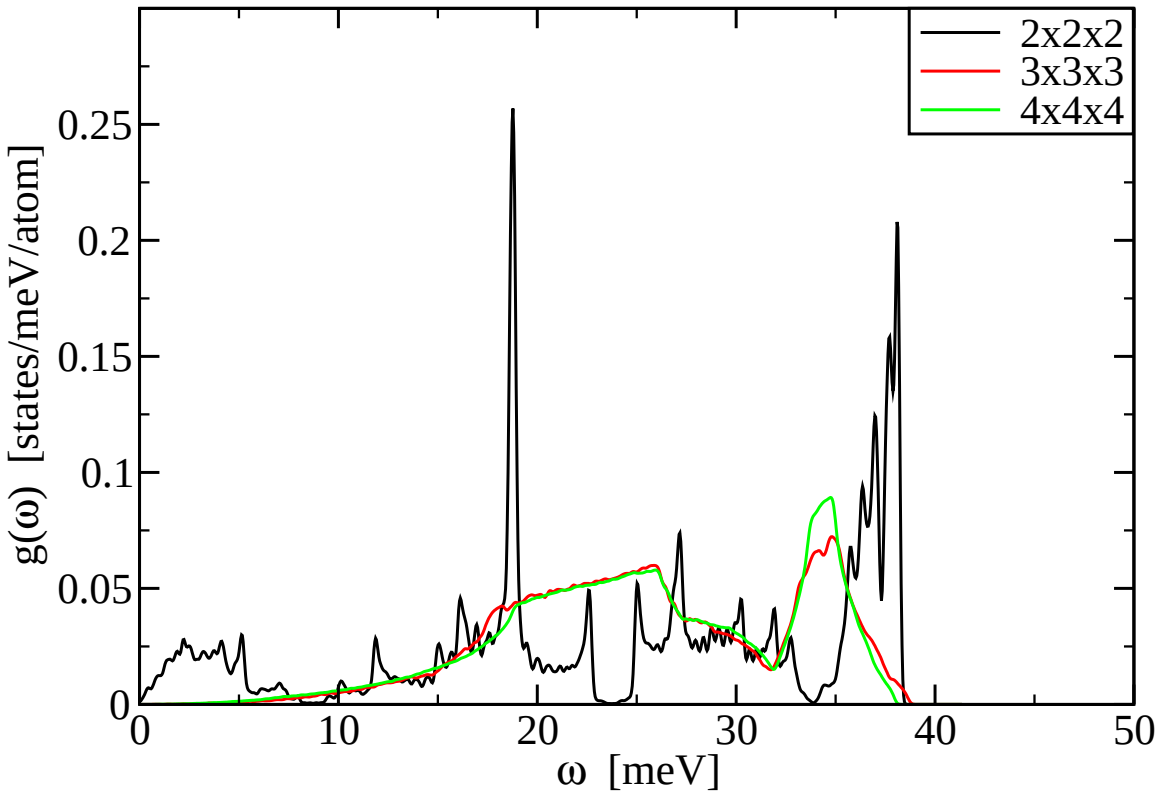

Figure 2.6: Phonon density of states of bulk FCC Ni with different cell sizes. $4 \times 4 \times 4$ cell has 64 repetition of the primitive cell and thus contains 64 Ni atoms.

and the electronic entropy $S_e(T)$ is,

$$S_e(T) = \int dE D(E)[f(E,T)\ln(f(E,T)) + (1 - f(E,T))\ln(1 - f(E,T))]. \quad (2.97)$$

F_e is typically 100 times smaller than F_{vib} as shown in Fig. (2.7) and is neglected in this thesis.

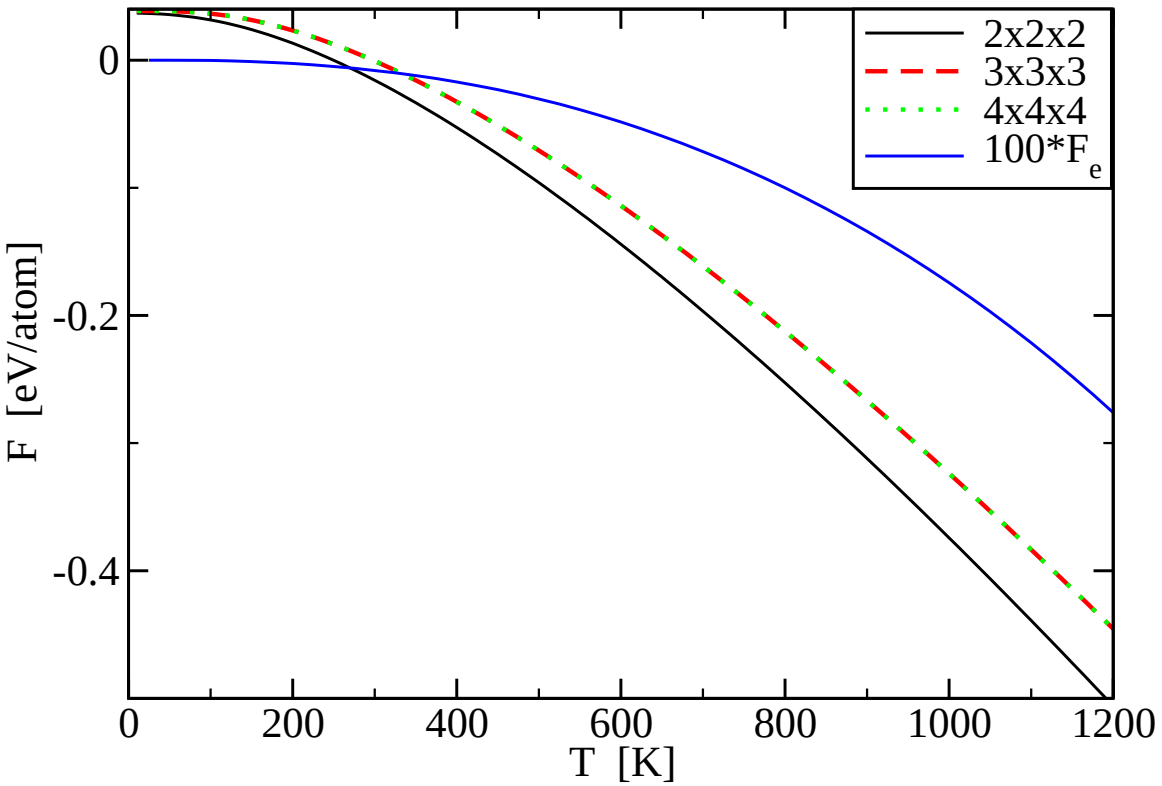

Figure 2.7: Vibrational free energy F_{vib} of bulk FCC Ni with different cell sizes and electronic free energy F_e of bulk FCC Ni. $4 \times 4 \times 4$ cell has 64 repetition of the primitive cell and thus contains 64 Ni atoms. F_e is calculated with the primitive cell.

Chapter 3

Bi on Ni(111) Surface[1]

3.1 Introduction

During the growth of thin metallic films, confinement of electrons can favor film heights that are commensurate with half the Fermi wavelength [84]. This well-known quantum size effect due to confinement (QSE) has long been studied in various materials, including bismuth. Bismuth differs from conventional QSE elements because it is a semimetal with an especially long Fermi wavelength ($\sim$ 40 nm) [85, 86] that causes various physical properties of Bi films to oscillate with long periods [87]. In ultrathin films ($\sim$ 1 nm), Bi exhibits allotropic transformations from puckered pseudocubic films to bulk-like rhombohedral films on Si (111) and on some quasicrystal surfaces [88, 89]. Experiments and first principles calculations concur that both film types exhibit bilayer growth, due to the exotic bonding character of Bi, rather than QSE [90]. In contrast, the initial growth of Bi films on metallic substrates has not been well studied until a recent experiment [2] reported stable 3, 5 and 7 layer Bi hexagonal films of Bi on the Ni (111) surface. They attempted to explain the stability by quantum confinement based on a free electron model. A more in-depth theoretical

[1]This chapter has been adapted from my paper "First-principles study of bismuth films on the Ni(111) surface" [13].

study is needed to understand this possible short period QSE in Bi.

Bulk Bi takes the rhombohedral structure of Pearson type hR2 (prototype α-As) common to group-V semimetals, which is distorted from the simple cubic structure by a Jones-Peierls mechanism [91]. The bulk Bi structure is best described as a stacking of bilayers in the [001] direction [92] (here we use 3-element hexagonal indexing, it would be [111] using rhombohedral indexing). Each bilayer has height 1.59 Å and is separated from the adjacent bilayer by 2.35 Å. Within the (001) plane the Bi spacing is 4.53 Å. However, three strong covalent bonds of length 3.06 Å link each Bi atom to others within each bilayer, while three weak metallic bonds of length 3.51 Å connect each Bi atom to others in the adjacent bilayer. The (001) plane is thus a natural cleavage plane, with divisions expected between bilayers. In addition to hR2, bulk Bi possesses many allotropes, especially at high pressure, including Pearson structure types mP4, mC4, cP1 and cI2, but it does not take the hexagonal structure.

In their experiment [2], the authors grew Bi on a Ni (111) surface at a temperature of 473 K via vapor deposition. Based on the low energy electron diffraction (LEED) patterns, deposition and film growth rates, and low energy electron reflectivity spectra, the authors proposed that initially a (7×7) wetting layer forms (hereafter referred to as adsorbed surface monolayer), which transitions to a 3 layer hexagonal film with a (3×3) surface cell sitting directly on the Ni substrate, as well as a 5 layer hexagonal film with a [3-112] surface cell, as coverage grows. However, at 422 K, Bi formed a 7 layer film with an (8×8) cell [93] surrounded by the 3 layer (3×3) film. The proposed 3 layer and 5 layer Bi films on Ni have in-plane lattice constant 3.7-3.8 Å (See Appendix A1 for discussion of lateral strain). The detailed structures are shown in Fig. 2 of Reference [2]. Taking their measured lattice constants, their proposed model, and an assumed free electron valence of 5, they calculated that their 3, 5 and 7-layer films were, respectively, 2.5, 4.0 and 5.0 Fermi wavelengths in height. As these structures and bond lengths have not been previously observed, and Bi is notoriously *not* free electron-like, a first principles electronic structure investigation

is warranted.

3.2 Methods

We apply electronic density functional theory, using the Vienna ab-initio simulation package (VASP [94, 95]) to solve the Kohn-Sham equations with the Perdew-Burke-Ernzerhof (PBE [77]) parameterization of the generalized gradient approximation (GGA) for the electron exchange correlation potential. We use projector augmented wave potentials [96, 97] with a fixed energy cutoff of 269.5 eV (the default for Ni). The d semi-core levels of bismuth are treated as valence electrons. Collinear spin polarization is used since Ni is ferromagnetic, though we test noncollinear magnetism to check the importance of spin-orbit coupling (SOC) for some structures. In the noncollinear calculations, we take the relaxed structure from collinear calculations and perform a static calculation. All structures are relaxed holding the cell sizes and bottom layer Ni atoms fixed, with in-plane lattice constants set by the relaxed bulk Ni structure. Energy convergence is carefully checked with respect to the vacuum size, k-point mesh and the number of Ni layers.

We construct models based on four Ni layers normal to the (111) surface with Bi films on one side. Our cells include 22 Å of vacuum, with periodic boundary conditions. Electrostatic energy created by the asymmetric charge distribution in the presence of Bi is small relative to the differences of surface energies. As an example, the relaxed 4 layer hexagonal film on the (3×3) cell is shown in Fig. 3.1. The hexagonal film structures are as described in [2] with 4 Bi atoms per layer in the (3×3) cell and hexagonal AB stacking. The relaxed 3 layer hR2 film (our model) on the (3×3) cell is also shown in Fig. 3.1. The hR2 films contain an adsorbed surface monolayer with 4 Bi atoms on the (3×3) cell similar to the hexagonal film. However, bulk-like Bi (001) films which contain 3 Bi atoms per layer on the (3×3) cell sit on top of the surface monolayer. Henceforth, when we say "hR2 film" we include the

surface monolayer and the bulk-like Bi (001) film on top.

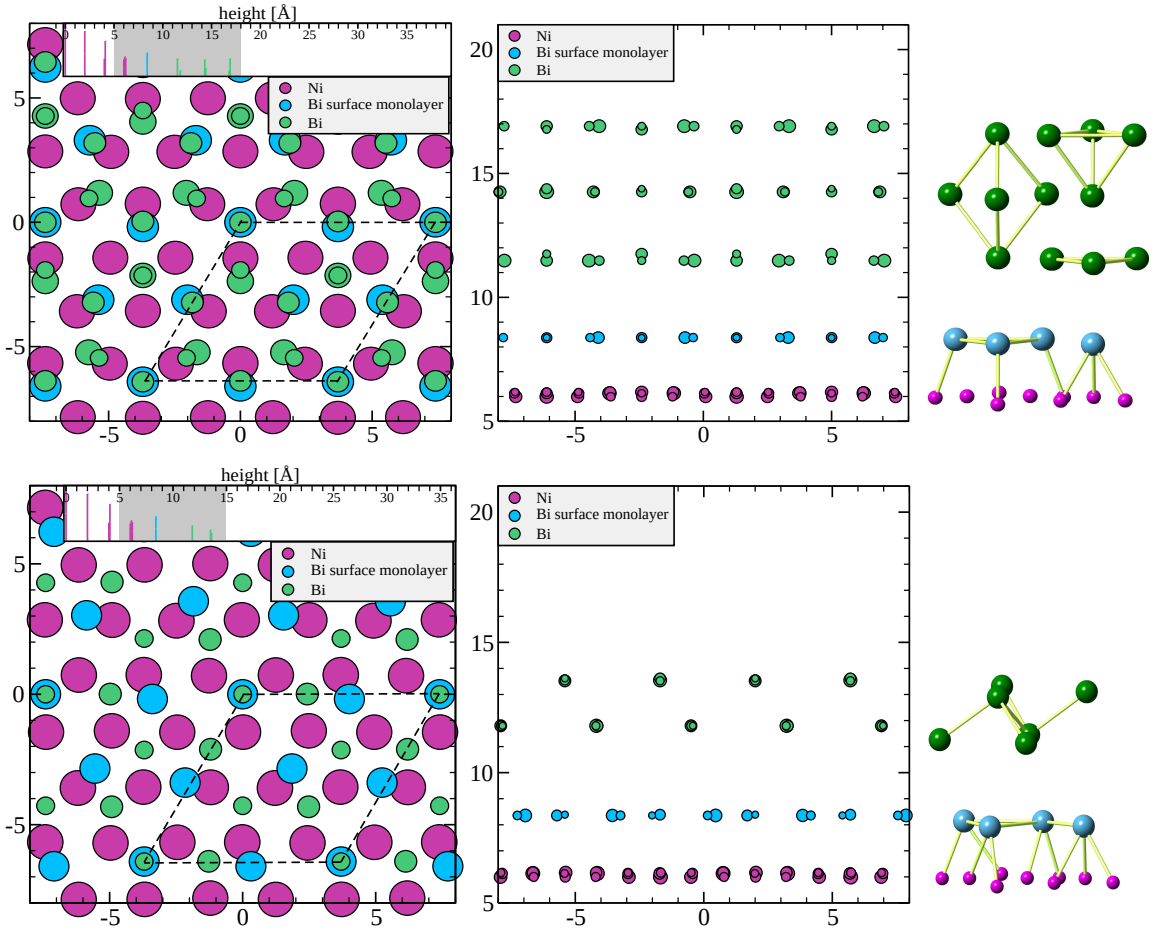

Figure 3.1: (Color online) Top view (top left) and side view (top middle) of relaxed 4-layer hexagonal Bi film on Ni (111) (3×3) cell (dashed). Same for 3 layer hR2 Bi film (bottom). Insert at top of the left-hand figure is a histogram of atoms at different heights. Shading in insert convers the region illustrated containing the top layer of Ni, the Bi surface monolayer and additional Bi layers. Atom size indicates depth (large below small). Length units are in Å . Chemical bonding is shown at right (slightly tilted).

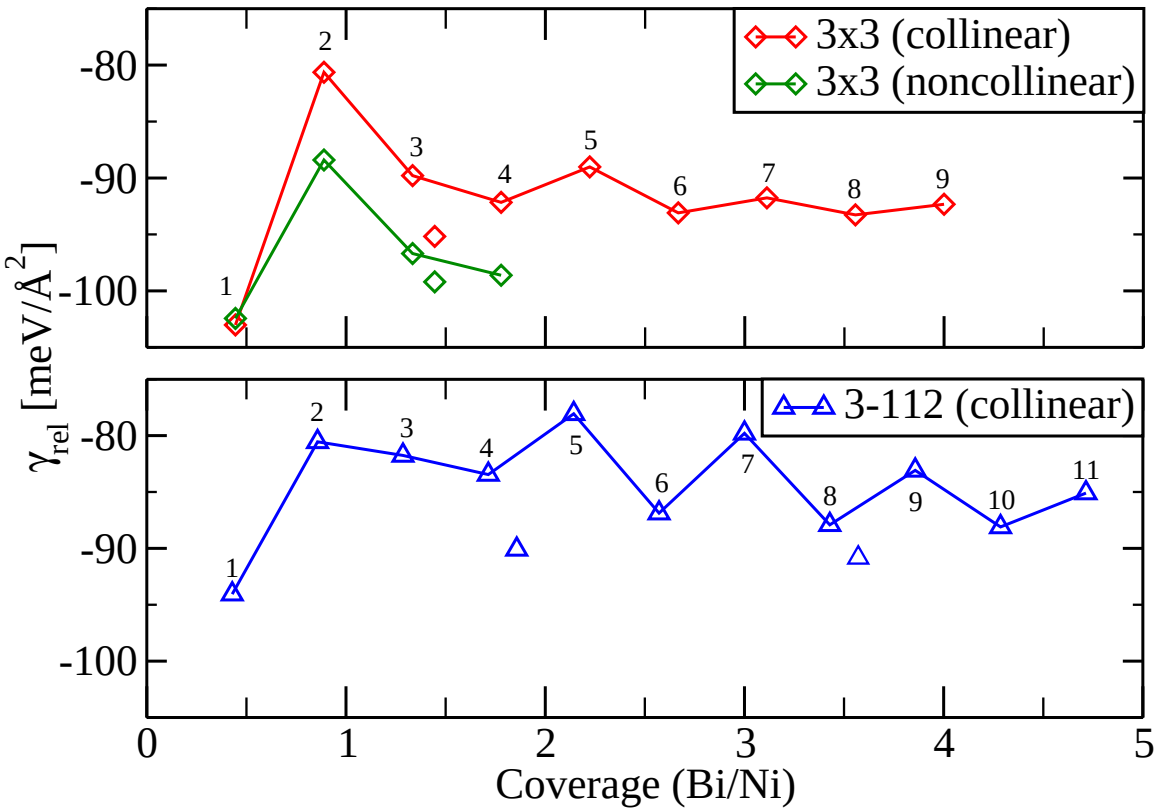

Figure 3.2: (Color online) Relative surface energies of hexagonal Bi films with (3×3) (top) and [3-112] (bottom) Ni (111) surface cells. Note the energy conversion factor is 1 eV/Å^2=16.0 J/m^2. Red and blue points are from collinear calculations, green points are noncollinear. Data points connected by line segments correspond to coverage of integer numbers of monolayers (1-9 for (3×3), 1-11 for [3-112]). Extra data points in the (3×3) cell are three layer films with one extra capping atom at a valley site. Extra points in the [3-112] cell are 4 layer plus one atom, and 8 layer plus one atom at valley sites.

3.3 Results and Discussion

We first compare the relative surface energies of the proposed Bi hexagonal films of different thickness on Ni (111). Several quantities are needed to define relative surface energy: the total energy E_{tot} of the N_{Bi} atoms of Bi on the surface of the 4-layer Ni

slab; the slope E_{Bi}, which is the linear part of E_{tot} as it depends on N_{Bi}; the energy E_{Ni}^{slab} of the Ni slab including its two free surfaces, each of area A. The slope E_{Bi} can be considered as the energy of bulk Bi in the hexagonal structure with the in-plane lattice constant determined by the surface cell [98]. With these definitions, relative surface energy is

$$\gamma_{rel} = [E_{tot} - E_{Ni}^{slab} - E_{Bi}N_{Bi}]/A. \tag{3.1}$$

Fig. 3.2 shows the relative surface energies of the (3×3) and [3-112] hexagonal films. A structure is relatively stable if the second derivative of its relative surface energy with respect to film thickness is positive [99]. Relative stability occurs for (3×3) cells of 1, 3, 4, 6 and 8 layers and for the [3-112] cells of 1, 4, 6, 8 and 10 layers. The asymptotic period 2 oscillations of relative surface energies are reminiscent of the QSE. However, these predicted stabilities disagree with the experimentally discovered film heights. Specifically, the predicted relatively stable 4 layer (3x3) film is not seen experimentally and we do not confirm stability of 5 layer hexagonal [3-112] film.

Also shown in Fig. 3.2 are data points for films with single Bi adatoms. These data points lie below the relative surface energies of integer layer coverage, revealing that terminating on complete hexagonal layers is unfavorable. Strong puckering of the hexagonal layers occurs during relaxation of structures with adatoms. Relative surface energies calculated with SOC are shown for the (3×3) films. SOC influences the relative surface energies quantitatively but does not alter the sequence of stable structures.

The relatively stable 4-layer (3×3) structure is illustrated in Fig. 3.1. The first layer Bi atoms strongly bond with the Ni surface atoms. On top of the first layer, Bi atoms form slightly puckered layers in order to achieve short Bi bonds with adjacent layers. These short covalent bonds lower the relative surface energy.

To test the proposed free-electron model of QSE, we have done a genuine first principles study of QSE in free standing hexagonal Bi films (see Appendix A2) and find that the actual predicted oscillation period is close to 3 layers. Understanding

this QSE requires incorporating band structure effects and cannot be understood on the basis of a free-electron model. Thus our first principles calculations cast doubt on both the hexagonal structure model and the proposed explanation in terms of QSE of hexagonal films.

We now seek alternate film structures. Inspecting Fig. 3.1 we note the interaction of the upper layer Bi with the surface monolayer is weak, so strong deviations of structure and bonding from bulk Bi due to the Ni substrate are not anticipated. Thus bulk-like hR2 Bi (001) films are good candidates to grow on top of the surface monolayer. For example, a 3 layer hR2 film (see Fig. 3.1) consists of the surface monolayer plus an hR2 (001) bilayer. The in-plane lattice constant of bulk hR2 Bi is 4.53 Å(see Appendix A1). Meanwhile, $\sqrt{3}$ times the Ni interatomic spacing is 4.31 Å which differs by only 5%. Furthermore, in our calculated energy of strained free standing Bi (001) films, the energy minimum occurs at in plane lattice constants 4.3 Å, 4.4 Å and 4.5 Å for one, two and three bilayer films respectively. Thus the stable thin bilayer films match with Ni very well.

To illustrate the relative stability of various structures, we compare the surface enthalpy of formation, which is defined as,

$$\Delta H/A = [E_{tot} - E_{Ni}^{slab} - E_{Bi}^{bulk} N_{Bi}]/A \tag{3.2}$$

which differs from the relative surface energy γ_{rel} in Eq. 3.1 only in our choice of reference energy for pure Bi, E_{Bi}^{bulk} is the relaxed Bi bulk energy in the hR2 structure.

Fig. 3.3 shows the enthalpy of formation for various surface structures with different thickness. Notice that both the (8×8) and (7×7) surface monolayer structure touch the convex hall which implies they are both energetically stable. The stable (3×3) surface monolayer is e2quivalent to both 1 layer hexagonal film and hR2 film with (3×3) cell. Moreover, for higher coverage, hR2 films have much lower energy than the hexagonal films. For instance, at the same total coverage of 16/9=1.8 Bi/Ni, the total energy the five layer hR2 film is 1.5 eV lower than the four layer hexagonal film on the bare (3×3) surface. This energy difference is much larger than the thermal

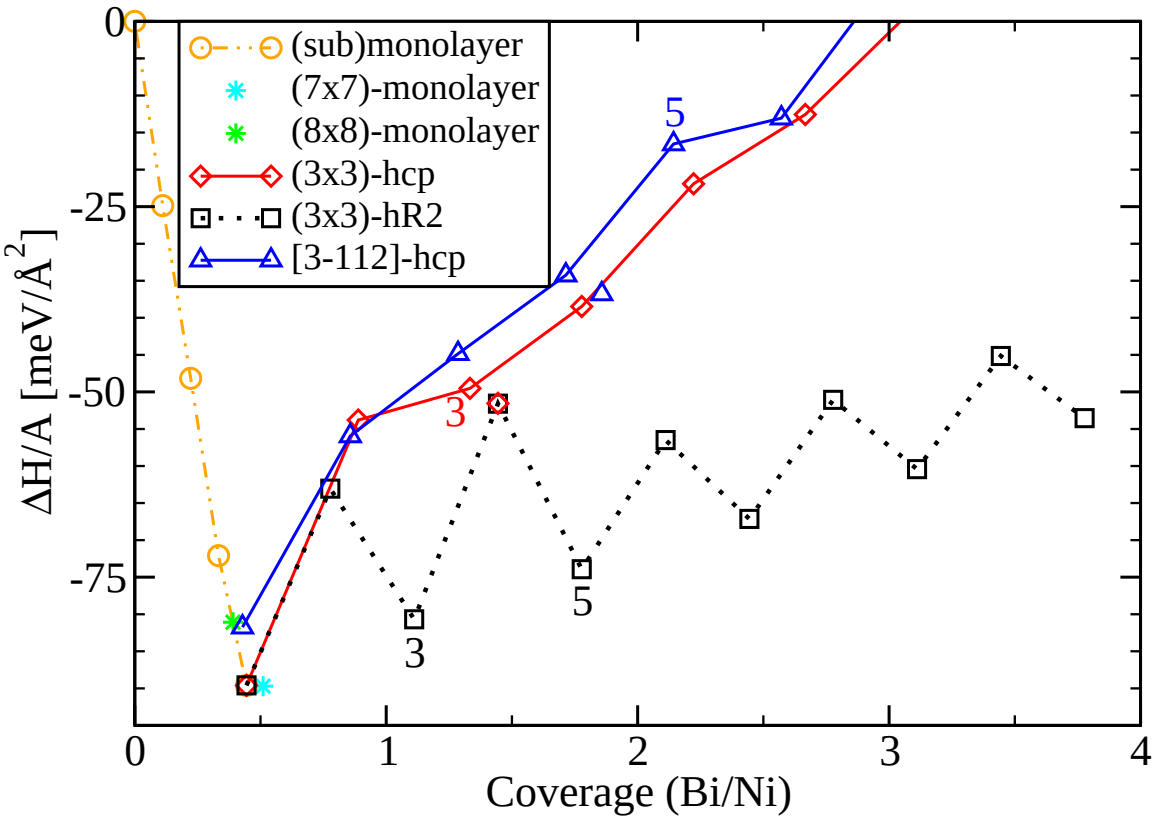

Figure 3.3: (Color online) Enthalpy of formation. Dot-dashed orange points are the (sub)monolayer structures with (3×3) cell. Cyan and green stars are the (7×7) and (8×8) surface monolayer respectively. Red points are hexagonal films and black are hR2 Bi films on the (3×3) cell. Blue points are hexagonal Bi films on the [3-112] cell. Color and plotting symbol are shared with Fig. 3.2 for (3×3) and [3-112] cells.

energy, k_BT=40 meV at 473 K. The hR2 films are thus much more likely to form than the hexagonal films. The hR2 films favor odd number of layers (surface monolayer + integer bilayers) which is consistent with the experimental observations of 3, 5 and 7 layer films. However, the stability is due to the exotic chemical bonding of Bi rather than QSE.

To further illustrate the stable sequence from equilibrium thermodynamics, we calculate the surface free energy. This quantity is the Legendre transform of the enthalpy of formation (Eq. 3.2), replacing the surface coverage with relative chemical

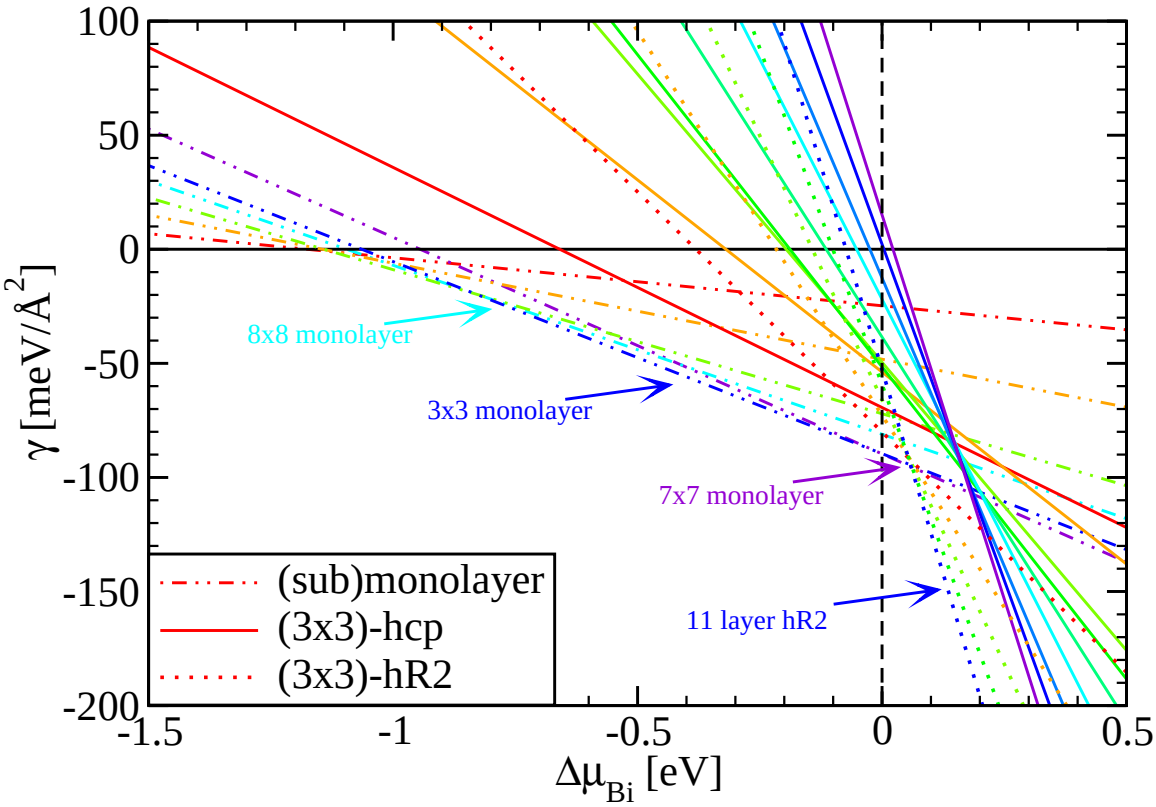

Figure 3.4: (Color online) Surface free energy. Dashed-dotted lines stand for monolayer or less. Solid and dotted lines stand for hexagonal and hR2 films on (3×3) cells respectively. Different slopes indicate different coverage according to Eq. 3.3. Stable sequence is indicated by arrows for monolayer or more. Vertical line at $\Delta\mu$ =0 indicates chemical potential of unstrained bulk Bi.

potential $\Delta\mu_{Bi}$. From equilibrium thermodynamics, the most stable structure at a certain Bi chemical potential $\Delta\mu_{Bi}$ minimizes the surface free energy [100],

$$\gamma = [\Delta H - \Delta\mu_{Bi} N_{Bi}]/A \tag{3.3}$$

where ΔH is the enthalpy of formation (Eq. 3.2), $\Delta\mu_{Bi} = \mu_{Bi} - E_{Bi}^{bulk}$ is the Bi chemical potential relative to unstrained bulk Bi. The results in Fig. 3.4 shows the stable sequence of surface structures is from bare surface to one atom on the (3×3) cell at $\Delta\mu_{Bi}$=-1.16 eV, to three atoms on the (3×3) cell at -1.11 eV, to (8×8) surface

monolayer at -0.83 eV to four atoms ((3×3) surface monolayer) at -0.82 eV, to the (7×7) surface monolayer at -0.01 eV, and then finally to the 11 layer hR2 films at around 0.06 eV. Extrapolating to an infinite height strained film yields a limiting vertical line at $\Delta\mu_{Bi}$ =0.05 eV (not shown). Other structures are thermodynamically unstable. However due to the energy cost to forming edges of small and high Bi islands, and the kinetic barrier at the boundary of Bi films, tall islands should not appear. Instead, metastable structures with low energies (e.g. finite thickness hR2 films) will appear in actual growth. The hexagonal-based structures lie systematically above the hR2 ones. By studying the bulk Bi energy with different lateral strains, we confirm that the underlying reason that hR2 films are more favorable than hexagonal films is that Bi favors a bilayer structure with strong covalent bonding (see Appendix A1).

Besides the hexagonal and hR2 (001) films, we also studied the energy of free standing hR2 (012) films. The 1 and 2 bilayer hR2 (012) films are more stable on Si (111) than hR2 (001) films [88]. However, with the Ni lattice constant rather than Si, the commensurate bilayer (001) film has lower energy by 30 meV/atom, and thus the (012) films are not favorable. This is also consistent with the experimental observation that no pseudocubic structure appears.

3.4 Conclusion

We study the growth of Bi on Ni (111) surface using first principles calculations. The proposed hexagonal films pucker under relaxation and are energetically and mechanically unstable to adding capping atoms. In the experiment, the authors identified the surface cell to be (3×3) and [3-112], and proposed hexagonal structure based on LEED patterns. However, film heights and Bi-Bi in-plane separation were inferred indirectly based on deposition rates and electron reflectivity curves. Their free electron model introduced to interpret their results is of doubtful validity. We find instead,

using a full ab-initio treatment, that bulk-like (001)-oriented hR2 films above the surface monolayer are more energetically favorable than hexagonal films. One large difference between these two models is the in-plane distance of Bi, 3.7 Å for hexagonal and 4.3 Å for hR2 which can be further examined by experiment. We have not investigated why different film thickness favor different surface cells.

If our model is correct, growth on Ni (111) might provide a useful synthesis of uniform hR2 bilayers, which have been shown to act as two-dimensional topological insulators [101, 102]. Besides the surface growth, phenomena of Bi at Ni interfaces also attract attention recently. Liquid Bi penetrates and segregates at Ni grain boundaries forming bilayer structures [6] in a stable grain boundary phase called a complexion [28, 103]. These bilayer interfacial structures can possibly explain the long standing puzzle of the liquid metal embrittlement. However, the underlying mechanisms of bilayer segregation and their relation with embrittlement have not been revealed at the quantum level. Our study of Bi on Ni surfaces serves as a precursor to this interfacial study. In particular, we note that a pair of surface monolayer films, one on each surface at a grain boundary, provides an attractive model for the observed Bi bilayers. We hope our theoretical work can trigger more interesting work, both theoretical and experimental in these subjects.

3.5 Appendix

3.5.1 A1. Lateral strain

The proposed Bi hexagonal films have in-plane lattice constant $a = 3.7$ Å (3×3) and 3.8 Å ([3-112]), while the hR2 films commensurate to Ni (111) has $a = 4.3$ Å. To explain why the hR2 films are more favorable than the proposed hexagonal films we investigate the bonding character of Bi by calculating bulk Bi energies with different a. We adopt bulk cells with a (1×1) unit cell in the xy plane and 6 atomic layers in the z direction. The a's are fixed while lattice constants c's are fully relaxed. For a

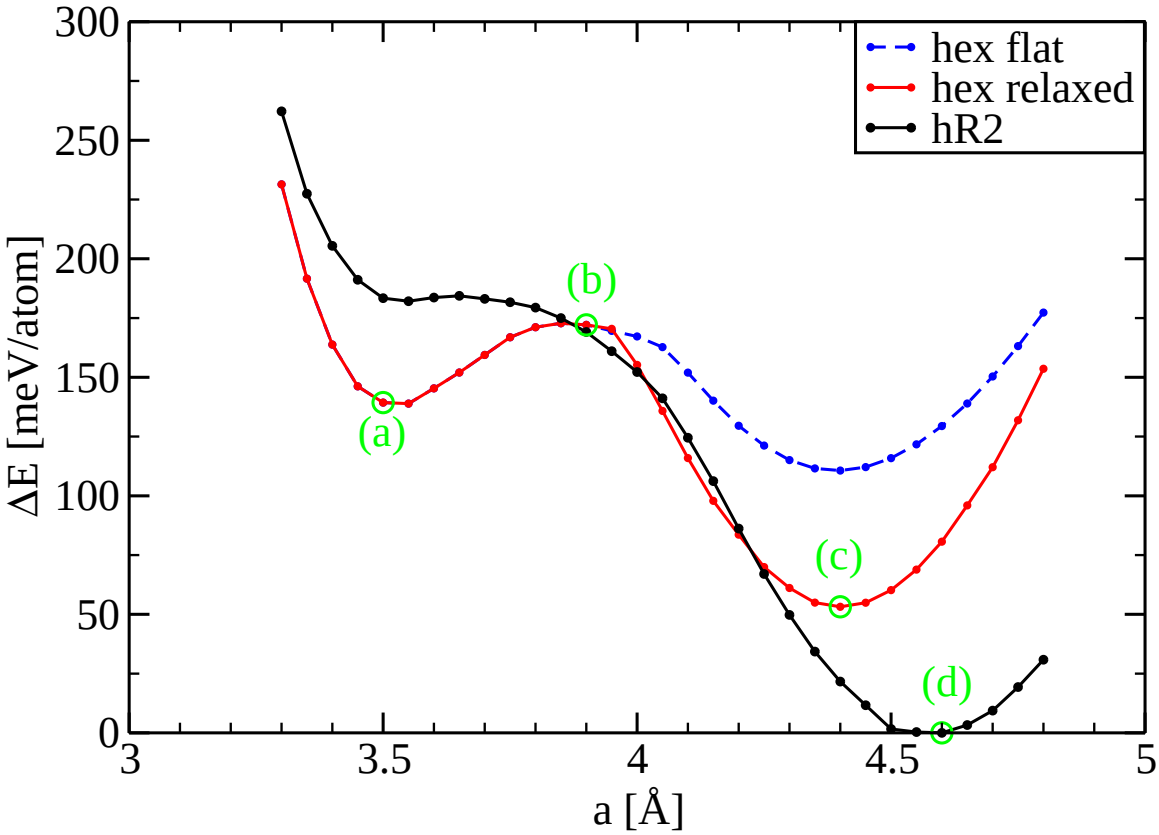

Figure 3.5: (Color online) Bi bulk energy of hexagonal and hR2 structures. Black is the relaxed hR2 structure. Red is the relaxed hexagonal structure. Blue is the evenly spaced hexagonal structure. Points (a),(b),(c),(d) correspond to the structures whose energies are plotted in Fig. 3.6.

less than 3.9 Å , both the relaxed hexagonal and hR2 structures are evenly spaced. For larger a values, Bi in both structures pairs up to bilayer structures. Fig. 3.5 shows Bi hexagonal and hR2 bulk energies with fixed a. Clearly, the paired hR2 bilayer structures with $a \approx 4.6$ Å are more favorable than the proposed hexagonal structures with $a \approx 3.5$ Å. By paring up, the Bi chemical bonds change from metallic to covalent in nature. This strongly affects the periods and amplitudes of surface energy oscillation of free standing Bi films.

3.5.2 A2. Quantum size effect

In thin metallic films, electrons are confined in the vertical direction. At low temperature, the energies of the confined electrons varying with film thickness governs the relative stability of the films. This leads to "electronic growth" [84], a type of QSE. Based on the usual quantization rule, the energy oscillation period in a free electron model is half of the Fermi wavelength [104]. In a solid, taking account of the band structure, the actual energy oscillation is the superposition of different oscillations at high symmetry points in the surface Brillouin zone [105]. For hexagonal metal, the (001) electron confinement energy can be written as,

$$E(N) = A_{\bar{\Gamma}} \sin(2k_{\bar{\Gamma}}Nd + \phi_{\bar{\Gamma}}) + A_{\bar{M}} \sin(2k_{\bar{M}}Nd + \phi_{\bar{M}}) + A_{\bar{K}} \sin(2k_{\bar{K}}Nd + \phi_{\bar{K}}) \quad (3.4)$$

where $\bar{\Gamma}$, $\bar{M}$ and $\bar{K}$ are three high symmetry points in the surface Brillouin zone, k's are the Fermi wave vectors, A's characterize the importance of those three points, ϕ's are the phase shift of three oscillations, N is the number of layers and d is layer spacing. The resulting energy is the superposition of those three oscillations. We compare the band structure prediction and the total energy oscillation of Bi films.

Fig. 3.6 shows the surface energy oscillation with different a values. Here the surface energy is defined as,

$$\gamma_{surf} = \frac{1}{2A}[E_{tot} - E_{Bi}N_{Bi}] \quad (3.5)$$

where E_{tot} is the energy of the film, N_{Bi} is the number of Bi atoms in the film, A is the surface area and E_{Bi} is the linear part of the total energies of the film structures as in Eq. 3.1. Shown in Fig. 3.6(a), for hexagonal films with $a = 3.5$ Å, the oscillation is complex in both period and amplitude reflecting the superposition of multiple periodicities. Fourier analysis of γ_{surf} yields a period of around 3 layers. From our band structure calculation, the bulk Fermi wave vectors at $\bar{\Gamma}$, $\bar{M}$ and $\bar{K}$ are, respectively, $0.59\pi/d$, $0.33\pi/d$ and $0.13\pi/d$. Averaging over these three frequencies, the resulting oscillation period is 2.9 layers, which agrees well with the total energy

calculation γ_{surf}. This QSE due to electron confinement does govern the energy oscillation of the free-standing hexagonal film with $a = 3.5$ Å. However, the energy oscillation amplitude is much smaller than the energy oscillation of Bi hexagonal films on Ni (111), implying that quantum size effect is not the dominant factor in determining the stability of Bi hexagonal film on Ni (111). Also unlike Bi on Ni (111), SOC does alter the relative stability of free standing hexagonal films with $a = 3.5$ Å.

Fig. 3.6(b) shows the surface energies of hexagonal films with a equal to 3.9 Å where the bulk Bi atoms start to pair up. The energy oscillation period is close to 2 layers which is different from the band structure prediction of 3.2 layers. Fig. 3.6(c) and 3.6(d) show the energies of hexagonal films with a equal to 4.4 Å and hR2 films with a equal to 4.6 Å respectively. In both cases, the energies show bilayer oscillation with much larger amplitude than the oscillation due to this QSE. We conclude that the oscillations of γ_{surf} are not due to this QSE for $a > 3.9$ Å instead it is due to covalent bonding into bilayers which is a different type of QSE.

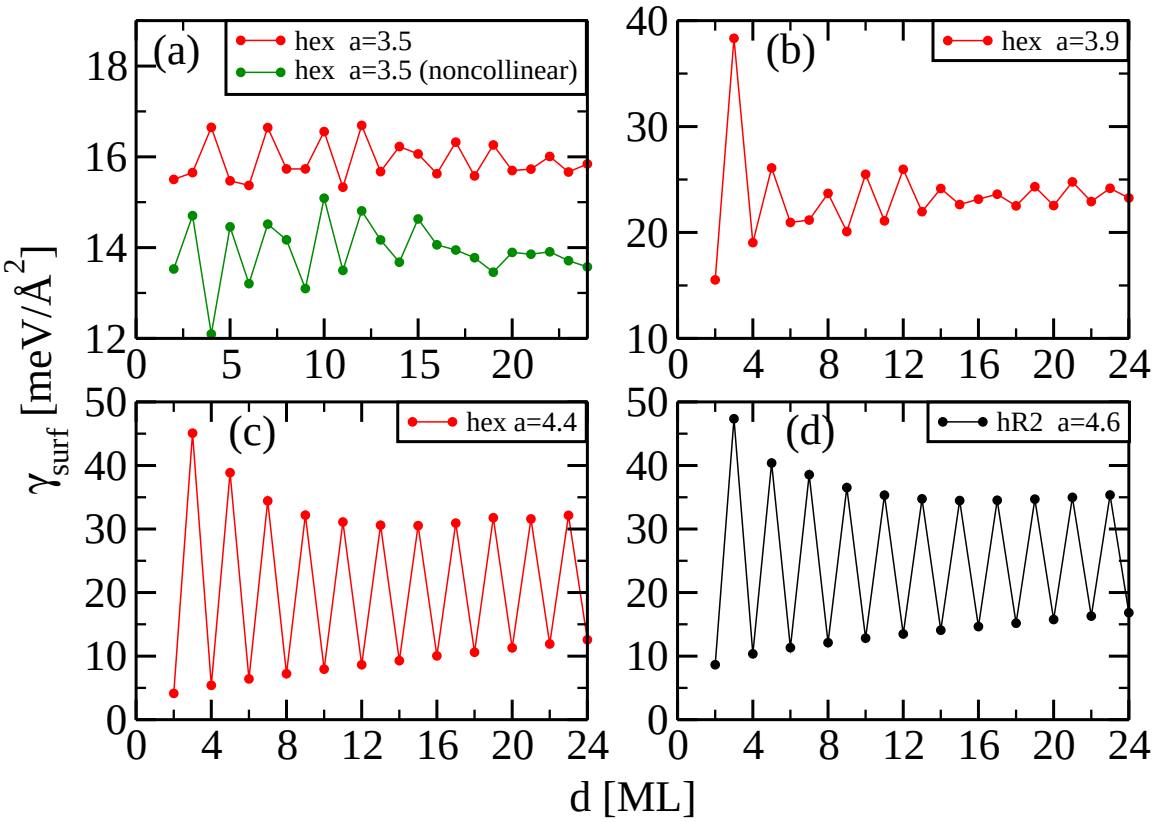

Figure 3.6: (Color online) Surface energies of free standing Bi films with different in-plane lattice constants a (units of Å). Black and red curves are using collinear calculation. Green using noncollinear.

Chapter 4

Bi on Transition Metal Grain Boundaries[1]

4.1 Introduction

Recently, grain boundary segregation with discrete numbers of layers (Dillon-Harmer complexions [36, 103]) were discovered in metallic systems Bi-Ni [6] and Bi-Cu [48], which could possibly explain the long standing puzzle of LME. In these experiments, Bi formed bilayer films ubiquitously in Ni at general orientation GBs around the penetration tip. In contrast, low-energy Ni grain boundaries were found to be clean (ie. with no Bi). Bi also formed bilayer films at Cu GBs around the penetration tip. However, the bilayer films were only observed close to the tip than at Ni GBs indicating bilayer films were stable over a much narrower Bi chemical potential window. Similarly to Ni, Bi did not segregate at low energy Cu GBs. A study of Fe revealed no Bi films [106].

A recent theoretical study [37] of Bi at Ni and Cu(111) twist and $\Sigma5(310)$ GBs found the Bi bilayer enthalpy of formation on $\Sigma5(310)$ is negative, which indicates

[1]This chapter has been adapted from our paper "First Principles Study of Bismuth Films at Transition Metal Grain Boundaries" [20].

thermodynamic stablity, while on (111) twist GBs it is positive. The authors proposed that bilayers are more stable than monolayers based on interaction strength between Bi and Ni layers and an electric dipole generated in the Bi bilayer on (111) twist GB. However, neither the origin of different segregation behavior of Bi on Ni compared with Cu, nor the relative stability of bilayer and trilayer films, was discussed. Moreover, a detailed study of the film structure, registry and bonding character is needed.

In this paper, we present a first-principles study of Bi films on low energy $\Sigma3(111)$ and high energy $\Sigma5(210)$ transition metal GBs. Our study explains bilayer film formation on Ni and Cu high energy GBs and its absence on Fe GBs (see Appendix A1 for Fe). Moreover, we discover a non-monotonic trend of Bi bilayer stability at 3d transition metals Co, Ni and Cu. We explain this trend based on competing effects of orbital localization and magnetization, and confirm this analysis with crystal orbital Hamilton populations (COHP) [107, 108] calculations. By exploiting the weak Bi interlayer interaction, we propose a model that can be used to predict Bi bilayer stability on various Ni GBs with relatively simple surface calculations. We discuss the temperature effect and the effect of Bi bilayer on embrittlement.

4.2 Methods

Our calculation methods are similar to our study of Bi on Ni(111) [13], namely PAW potentials [96, 97] in the PBE [77] generalized gradient approximation with default energy cutoffs using VASP [94, 95]. To find stable structure at GBs, we first study Bi structures on free surfaces. For Bi on TM(111) and (120), we construct models based on four and six metal layers normal to the surface respectively with Bi films on one side. We choose the $\Sigma3(111)$ twist and the $\Sigma5(012)$ tilt GBs as representative low energy and high energy GBs respectively. $\Sigma3(111)$ is formed by cleaving the bulk along the (111) plane, rotating one grain around [111] by 60^0 and rejoining the two

parts [109]. Σ5(012) is formed by cleaving the bulk along the (012) plane, rotating one grain around [100] by 53.1^0 and rejoining the two parts after removing overlapping atoms (see Fig. 4.1).

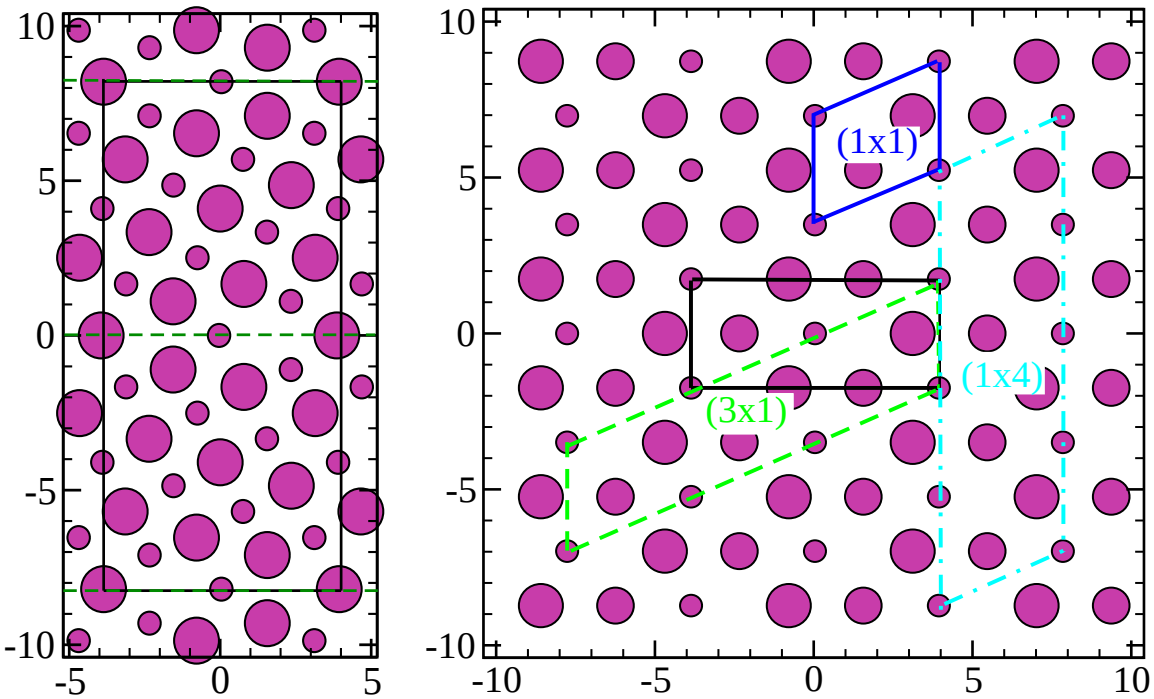

Figure 4.1: (Color online) Left: Side view of our Σ5(012) GB. The black cell is our unit cell. The dashed green lines are GB planes. Right: Top view of Σ5(012) GB plane. Three layers of atoms are shown. The black solid cell is the orthorhombic unit cell we use to calculate Σ5(012) GB energies. Atom size indicates depth (large below small). Units are Å.

For Bi on Σ3(111) GBs we stack six layers of metal with periodic boundary conditions and rotate three layers relative to the other three, thus creating the GBs. Then we insert our Bi film at one GB, leaving the other bare. To reduce computational complexity, the segregated structures at Σ5(012) GBs are calculated with six layers TM at each side of the Bi films and terminated by bare TM surfaces with vacuum at both sides. Convergence with respect to the number of Ni layers is documented in Appendix A2. The Σ5(120) GB plane is shown in Fig. 4.1. Later on, we refer the blue

solid cell as (1×1), green dashed cell as (3×1) and cyan dash-dotted cell as (1×4). To analyze interaction strength and bonding character, we perform COHP calculations which evaluate matrix elements of the total energy between pairs of atomic orbitals on neighboring atoms. The differential (dCOHP) reveals the bonding and antibonding orbitals while the integral up to the Fermi energy (iCOHP) measures the bond strength.

4.3 Results and Discussion

4.3.1 A. Film stability

Our calculated GB energies E_{GB} are shown in Table 4.1, and agree well with prior literature.

GB	Co	Ni	Cu
Σ 3(111)	-0.0016	0.0028 (0.0027 [110])	0.0001 (0.0014 [110])
Σ 5(120)	0.080	0.077 (0.089 [111])	0.055 (0.059 [112])

Table 4.1: GB energies, units are eV/Å^2. The energy conversion factor is 1 eV/Å^2 =16 J/m^2. Values from other studies are in parentheses. Note the Co Σ3(111) GB energy is negative because the $T = 0$ K state is HCP rather than the high-T FCC that we choose to compare with.

For Bi on the Ni(111) surface, we found a 4-atom Bi monolayer on a (3×3) surface cell is stable over a wide Bi chemical potential [13], and the same holds true for Co. For Bi on the Cu(111) surface, 2-atom Bi monolayer on a [2012] cell is stable, which agrees with experimental observation [113]. On TM(120) surfaces, Bi sitting on the valley sites of (1×1) cells [114] are stable over a wide range of chemical potential.

We then study various Bi films at GBs. To compare the stability of these films,

we calculate the enthalpy of formation, which is defined as,

$$\Delta H/A = [E_{\text{tot}} - E^{\text{TM}}_{\text{slab}} - E^{\text{Bi}}_{\text{bulk}} N_{\text{Bi}}]/A, \tag{4.1}$$

where E_{tot} is the energy of a TM slab containing GB segregated by Bi, $E^{\text{TM}}_{\text{slab}}$ is the energy of a TM slab containing a bare GB, $E^{\text{Bi}}_{\text{bulk}}$ is the Bi bulk energy, A is the GB area. Fig. 4.2 shows our enthalpies of formation. On the low energy Σ3(111) GBs, the enthalpies of Bi film formation are all large and positive, which suggests that Bi does not form stable films at these GBs. This is expected since the Σ3(111) GB differ from bulk only by a low energy stacking fault. It is energetically unfavorable to cut the strong bulk-like metal bonds and replace them by bonds with Bi. These results agree with the experimental observation [6, 48] of bare Ni and Cu low energy GBs near the Bi penetration tip. At the high energy Σ5(120) GB, ΔH is reduced for all TM. At Co Σ5(120) GB, ΔH remains positive suggesting all films are unstable. For Ni, all Bi films have negative ΔH which means Bi penetration is favorable for all these films. Moreover, bilayer Bi is most favorable, with lower enthalpy of formation than monolayer and trilayer. For Cu, Bi monolayer and bilayer film have negative enthalpies of formation. The bilayer preference is less pronounced than on Ni. Overall, the enthalpy of formation is less negative on Cu than on Ni, which indicates interfacial films are less favorable in the case of Cu.

To further illustrate the stability of Bi films at Σ5(120) GBs, we calculate the GB free energy. From equilibrium thermodynamics, the most stable structure at a certain Bi chemical potential minimizes the GB free energy γ [100],

$$\gamma = [\Delta H - \Delta\mu_{\text{Bi}} N_{\text{Bi}}]/A, \tag{4.2}$$

where $\Delta\mu_{Bi} \equiv \mu_{\text{Bi}} - E^{\text{Bi}}_{\text{bulk}}$ is the Bi relative chemical potential. Note that $\Delta\mu_{\text{Bi}} = 0$ corresponds to the chemical potential of bulk Bi.

As shown in Fig. 4.3, the stable sequence at Co Σ5(120) GB goes from a bare GB plane directly to an infinite height bulk-like film at $\Delta\mu_{Bi} = 0$ eV. In contrast, a Bi bilayer film is stable for $-0.37 < \Delta\mu_{Bi} < 0$ eV on Ni Σ5(120) GB and for

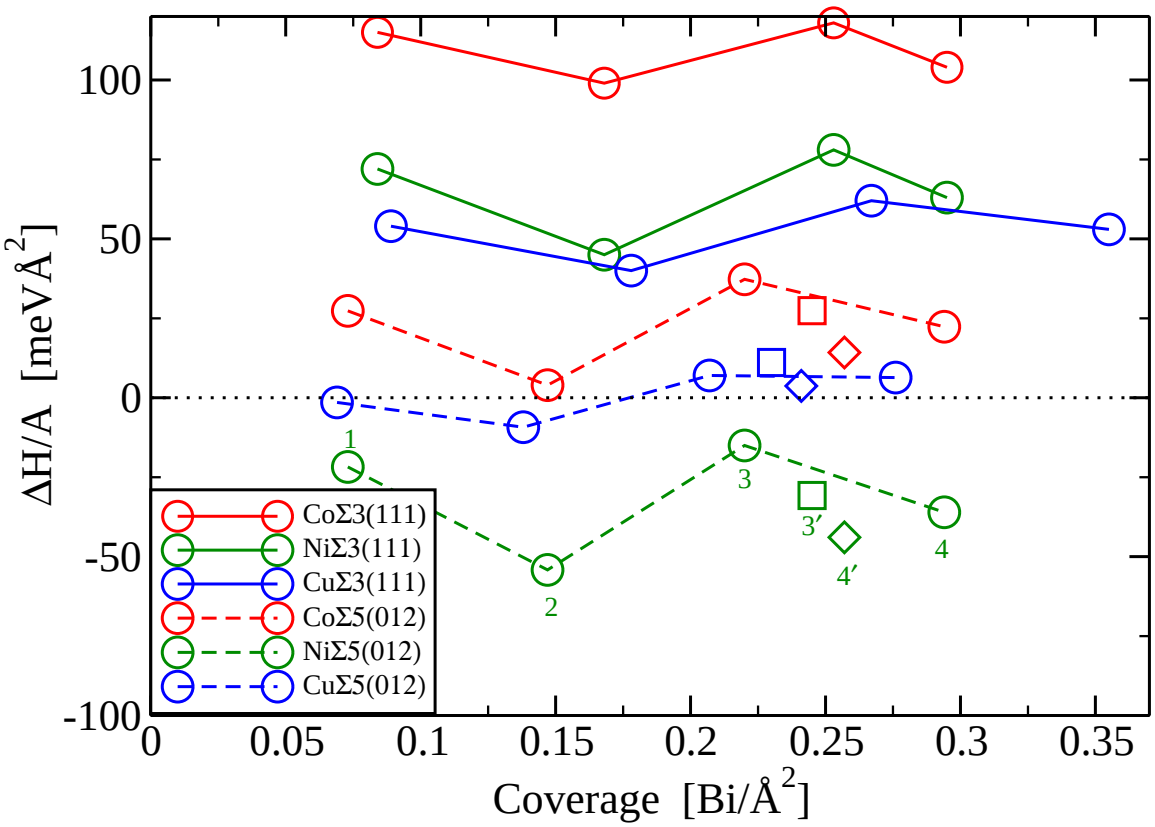

Figure 4.2: (Color online) Enthalpies of Bi films at Σ3(111) and Σ5(012) GBs. Solid lines connect Bi films on Σ3(111) GBs. Films of 1-3 layer thickness (labeled 1-3) have 4 Bi atoms per layer while the 4-layer films contain 4 Bi atoms per layer in layers adjacent to Ni but 3 Bi per layer in the middle two layers [13] for Ni and Co. Films for Cu have 2 Bi per layer. Dashed lines connect Bi films in (1×1) cells of Σ5(120) GBs. Red, green and blue colors indicate Co, Ni and Cu respectively. Square points (labeled as $3'$) stand for trilayer films in (3×1) cells of Σ5(120) GBs with denser middle layer (4 Bi in (3×1) cell). Diamond points (labeled as $4'$) stand for four layer films in (1×4) cells of Σ5(012) GBs with the in-plane density of the middle bilayer similar to bulk Bi (3 Bi in a (1×4) cell).

$-0.067 < \Delta\mu_{Bi} < 0$ eV on Cu Σ5(120) GB. Bi films are thus not stable on Co Σ5(120) GB. Moreover, the bilayer film is stable over a much wider chemical potential window on Ni than Cu Σ5(120) GB which is consistent with the experimental observations

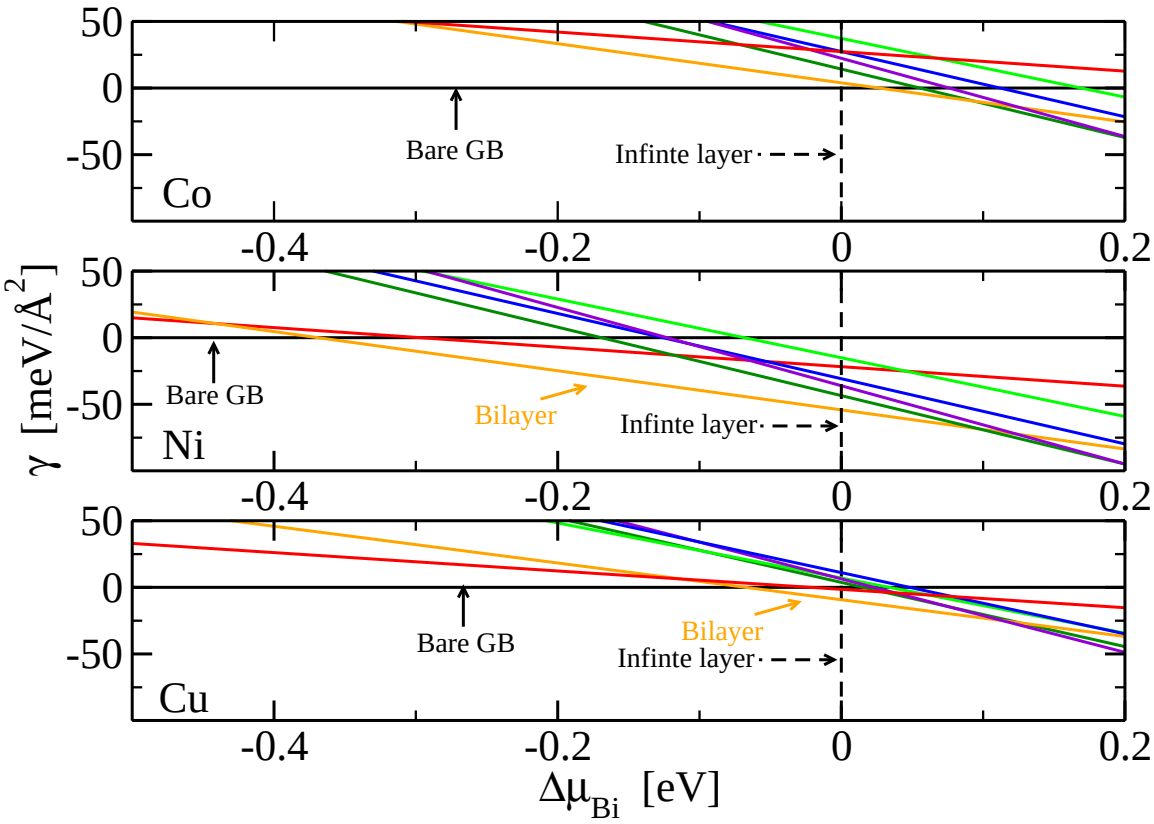

Figure 4.3: (Color online) GB free energy of Bi films at Co, Ni, Cu Σ5(120) GBs, respectively, top to bottom. The black solid lines stand for bare GBs while the black dashed lines stand for infinite bulk-like Bi films. Other lines are for different Bi films, with stable bilayer labeled.

[6, 48].

Studying other bilayer films with different registry and coverage, it turns out the valley site of a missing Ni atom is a strong Bi adsorption site. For structures with Bi density smaller than the (1×1) film, all Bi atoms relax into valley sites. The (1×1) film is more stable than these films due to the energy gain by putting more Bi at the remaining empty valley sites. With Bi density larger than the (1×1) film, Bi atoms in each layer bond with each other in the unfavorable metallic form and also leave some empty valley sites which weakens the bonds with Ni. Both these effects destabilize such films.

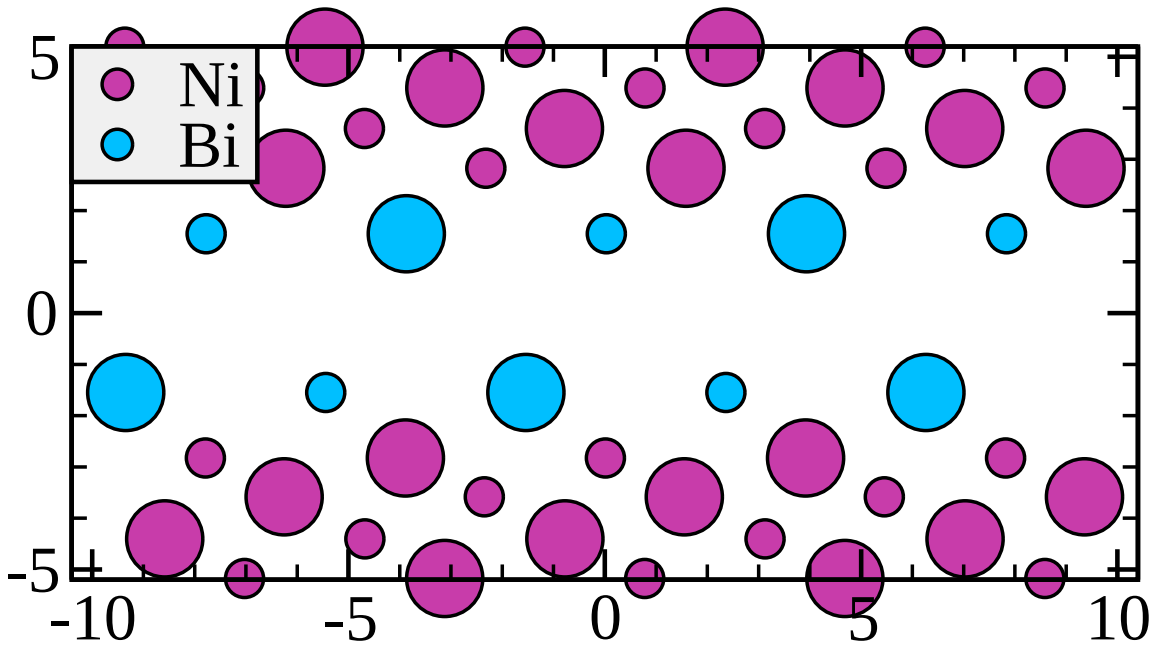

Figure 4.4: (Color online) Relaxed bilayer Bi films at (1×1) cell of Ni $\Sigma5(120)$ GB. Only Ni atoms close to Bi are shown. Atom size indicates depth (large below small). Units are Å.

Trilayer films are unfavorable at all GBs, again because of the bonding character of Bi. Bulk Bi has the common α-As group-V semimetal (strukturbericht A7, Pearson *hR2*) with rhombohedral space group $R\bar{3}m$ forming a bilayer structure. Each Bi atom has strong covalent bonds with three intrabilayer neighbors at the distance of 3.1 Å and bonds weakly with three interbilayer neighbors at 3.5 Å. The trilayer films contain a chemically adsorbed monolayer on each side of the GB plus a monolayer of atoms in between that forms metallic bonds. The four layer structure has a bilayer film similar to the bulk structure between the strong adsorbed monolayer films. Thus, bilayer films and four layer films are more favorable than trilayer films. The observed trilayer Bi film at Ni GB near the penetration tip is thus indeed predicted to be a metastable structure as inferred in Reference [6].

4.3.2 B. Thermodynamic Model

The Bi interlayer interaction is weak in the bilayer films at both Ni Σ3(111) and Σ5(120) GBs, with bond lengths around 3.9 Å and 4.2 Å respectively, which are larger than the weak Bi-Bi metallic bond. In experiment, the observed Bi layer spacing is 3.9±0.6 Å. Based on these observations, we propose a model to calculate the enthalpy of formation of Bi bilayer at Ni GBs with bare GB energies and surface adsorptions, by neglecting the Bi interlayer interaction,

$$\Delta H/A \approx E^a_{\text{surf}} + \Delta H^a_{\text{ML}}/A + E^b_{\text{surf}} + \Delta H^b_{\text{ML}}/A - E_{\text{GB}}, \tag{4.3}$$

where E^a_{surf} and E^b_{surf} are the surface energies of Ni surfaces a and b adjacent to the GB plane, ΔH^a_{ML} and ΔH^b_{ML} are the enthalpies of formation of Bi monolayers on Ni surfaces a and b. The first four terms represent the excess energy per area with bilayer intercalation. E_{GB} is the excess energy per area without intercalation. The values are shown in Table 4.2. We define $E^{\text{min}}_{\text{GB}}$ as the minimum energy of GB consisting of surfaces a and b such that formation of Bi bilayer is energetically favorable, i.e. for which $\Delta H/A \leq 0$. Hence

$$E^{\text{min}}_{\text{GB}} \approx E^a_{\text{surf}} + \Delta H^a_{\text{ML}}/A + E^b_{\text{surf}} + \Delta H^b_{\text{ML}}/A. \tag{4.4}$$

Results of this model are given in Tab. 4.3.

The enthalpies of formation from model predictions (ΔH^{model}) and direct calculations (ΔH^{calc}) are within 0.01 eV/Å^2, and slightly exceed the direct calculations because we neglect the interaction between Bi bilayers which lower the total energy. This model thus accurately predicts Bi bilayer enthalpies of formation, while being easier to calculate than direct Bi at Ni GBs.

Approximate energies for many bare GBs can be obtained from embedded atom method (EAM) calculations [115]. Direct comparison between DFT and EAM bare GB energies is shown in Fig. 4.5. The differences are small and within 0.005 eV/ Å^2, thus do not strongly affect the model prediction. Based on the EAM bare GBs, our

Surface	E_{surf}	$\Delta H_{\mathrm{ML}}/\mathrm{A}$	$E_{\mathrm{GB}}^{\mathrm{min}}$
(111)	0.118	-0.090	0.056
(001)	0.137	-0.122	0.030
(120)	0.150	-0.133	0.034

Table 4.2: Calculated input quantities for the enthalpy model (Eq. 3). Predicted $E_{\mathrm{GB}}^{\mathrm{min}}$ values for GB with the same surface plane (i.e. $a = b$) at two sides. The energy units are eV/Å^2. The Bi monolayer structure on Ni(100) surface is the $c(2 \times 2)$ structure as observed in experiment [1].

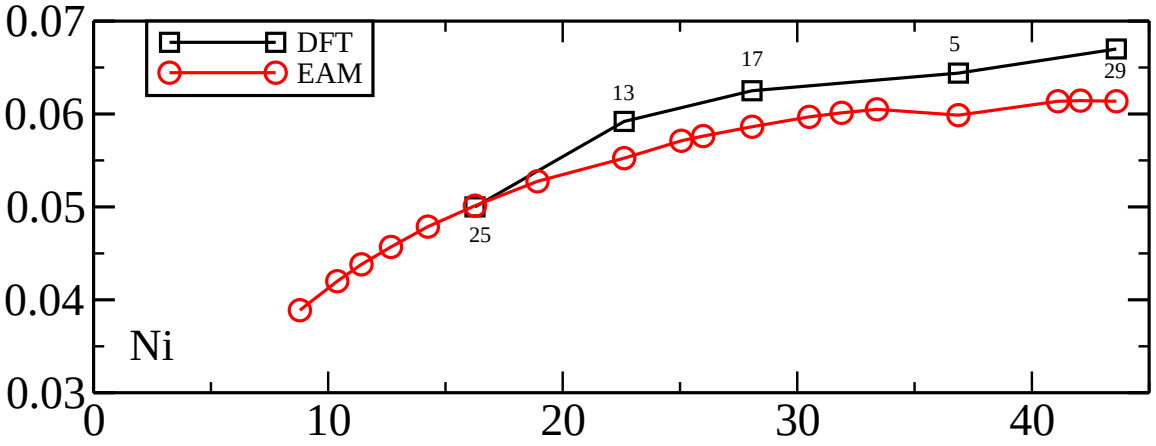

Figure 4.5: (Color online) Grain boundary energies calculated by DFT compared with embedded atom method (EAM) for Ni and Cu. The EAM data is taken from [14]. Numbers shown in the figure are the Σ values of those CSL GBs. For both metals, the results show similar trends and differ by less than 0.005 eV/ Å^2.

model predicts that Bi bilayer enthalpies of formation are positive on all Ni(111) CSL twist GBs, but are negative on (100) CSL twist GBs for rotation angles between 10 and 45 degrees. Moreover, for GBs with different adjacent surfaces (i.e. $a \neq b$) that are not commensurate with each other, model predictions that avoid artificial strain might be more accurate than affordable direct calculations. An example is shown in Table 4.3. This model could easily be generalized to other polycrystalline materials

GB	E_{GB}	$\Delta H^{\mathrm{model}}/\mathrm{A}$	$\Delta H^{\mathrm{calc}}/\mathrm{A}$	$W_{\mathrm{sep}}^{\mathrm{bare}}$	W_{sep}	Reduction
Σ3(111)	0.003	0.053	0.045	0.235	0.009	96.2%
Σ7(111)	0.029	0.027	0.023	0.209	0.009	95.7%
Σ5(100)	0.064	-0.034	-0.037	0.208	0.007	96.6%
Σ5(120)	0.077	-0.043	-0.054	0.220	0.010	95.5%
(111)/(100)	0.055	-0.012	-0.004	0.207	0.004	98.0%

Table 4.3: Model and calculated Ni GB energies and Bi bilayer enthalpies of formation at different Ni GBs. Work of separation for bare and Bi bilayer segregated GBs is shown on right. The energy units are eV/Å^2. The Σ7(111) GB is made by twisting the one side of bulk Ni by 21.8^o around the [111] axis with (111) as GB plane. The resulting GB cell is [3-112] as defined in [2] on which Bi favors 3 atoms per layer. The Σ5(100) GB is made by twisting one side of bulk Ni by 36.9^o around the [001] axis with (001) as GB plane. The general GB (111)/(100) is constructed with a =(111) and b =(100) planes with a (3×3) surface cell at the a side and a [2-213] surface cell (following the notation of [2]) at the b side. Unlike the CSL GBs, this general GB ΔH^{calc} is greater than $\Delta H^{\mathrm{model}}$ due to strain of the Ni cells (around 5%). This artificial strain introduced by forcing the two weakly interacting grains to share a common small cell makes the direct calculation inaccurate.

providing the interlayer interaction of segregated films is small.

4.3.3 C. Embrittlement and differences among TMs

Ni GBs are severely embrittled by Bi bilayer segregation. In Table 4.3, we show the work of separation (defined as $W_{\mathrm{sep}} = 2E_{\mathrm{surf}} - E_{\mathrm{GB}}$, the work needed to separate the GB [40]) at several bare and Bi segregated GBs. In all these GBs, W_{sep} is reduced by more than 95% due to the weak interaction between Bi layers [37].

The differences of Bi interactions among these three transition metal GBs can be

understood with a combination of localization of TM electron orbitals and magnetism. With increasing of atomic number from Co to Ni and to Cu, the 3d orbital becomes more localized, and thus the interactions between TMs and with Bi decreases. For example, shown in Table 4.4 the (012) surface energies E_{surf} and Bi monolayer $\Delta H/A$ on (012) surface diminish for Co, Ni and Cu respectively in nonmagnetic calculation. With magnetism, Co and Ni(012) E_{surf} decrease further due to increasing surface magnetic moment. The remaining greater Co surface energy due to stronger interaction between less localized orbitals makes the Co GBs harder to separate.

	Co(nonmag)	Co(mag)	Ni(nonmag)	Ni(mag)	Cu
E_{surf} (eV/Å^2)	0.193	0.164	0.152	0.150	0.100
ΔH (eV/Å^2)	-0.160	-0.118	-0.152	-0.133	-0.070
iCOHP(Bi-TM)	-1.75	-1.63	-1.77	-1.75	-1.33
iCOHP(TM-TM)^a	-1.38	-1.32	-1.13	-1.13	-0.43
iCOHP(TM-TM)^b	-1.17	-1.16	-0.85	-0.83	-0.66

Table 4.4: The (012) surface energy, Bi monolayer enthalpies of formation, integrated COHP (iCOHP) energies of Bi-TM bond, TM-TM bond near to Bi(a) and TM-TM bond away from impurities(b). The energy units are eV/bond for the iCOHP energies.

Values of iCOHP measure bond strength. The Bi-Co bond at surface is weaker than Bi-Ni when magnetism is included (see Table 4.4) due to the fact that Bi is nonmagnetic and quenches the TM surface magnetic moments. All of these effects are greater at the Co surface than Ni due to Co's larger surface magnetic moments, 1.93 μ_B/atom compared with 0.78 μ_B/atom for Ni. This leads to a greater increase in Bi $\Delta H/A$ on Co(012) than Ni(012) surface, compared with the nonmagnetic case. This effect is also manifested from our COHP calculation that the Bi-Co bond is weakened by 0.12 eV while Bi-Ni bond is weakened only by 0.02 eV due to magnetism. Thus Bi monolayers on Co(012) surface and Bi bilayers on Co $\Sigma5$(012) GB are less favorable to form than on Ni due to the stronger interaction between Co atoms than between Ni

atoms resulting from greater localization of 3d electrons on Ni, and weaker interaction between Bi and Co than between Bi and Ni, due to magnetism.

Apart from weaker interaction of Bi with Cu than with Ni, the Bi bilayer is less favorable on Cu than on Ni, since Bi gives electrons to Cu, increase the filling of Cu d states. This leads to stronger d orbital antibonding among Cu atoms close to Bi rather than s orbital antibonding as is inferred in [39]. Our COHP calculation results are shown in Fig. 4.6 (Note that for Cu, unlike Co and Ni, antibonding states lie below bonding states at the equilibrium lattice constant). The Ni-Ni and Co-Co bonds close to Bi however are stronger than in the bulk, where no antibonds appear.

4.3.4 D. Vibrational Free Energies

To incorporate the vibrational free energy we add ΔF_{vib} to ΔH, where the vibrational free energy ΔF_{vib} is calculated from the phonon density of states within the harmonic approximation [116] by integrating over the contribution of all independent phonon modes. For a single phonon mode with vibrational frequency ω, the vibrational free energy is $k_B T \ln[2\sinh(\hbar\omega/2k_B T)]$. The full vibrational free energy is,

$$F_{vib}(T) = k_B T \int g(\omega) \ln[2\sinh(\hbar\omega/2k_B T)] d\omega. \tag{4.5}$$

The phonon density of states $g(\omega)$ is calculated by employing the force constant method for phonon calculations with similar method to [117]. In our study, we calculate the vibrational free energy of the Bi atoms while keeping the TM atoms fixed. The change of vibrational free energy by mixing can be calculated by,

$$\Delta F_{vib}(T)/A = [F_{vib}^{\text{Bifilm}}(T) - F_{vib}^{\text{Bibulk}}(T)]/A, \tag{4.6}$$

where the F_{vib}^{Bifilm} is the total vibrational free energy of Bi bilayer at TM grain, and F_{vib}^{Bibulk} is the vibrational free energy of Bi in bulk form. The total change of free energy by mixing is thus,

$$\Delta F(T)/A = [\Delta H + \Delta F_{vib}(T)]/A. \tag{4.7}$$

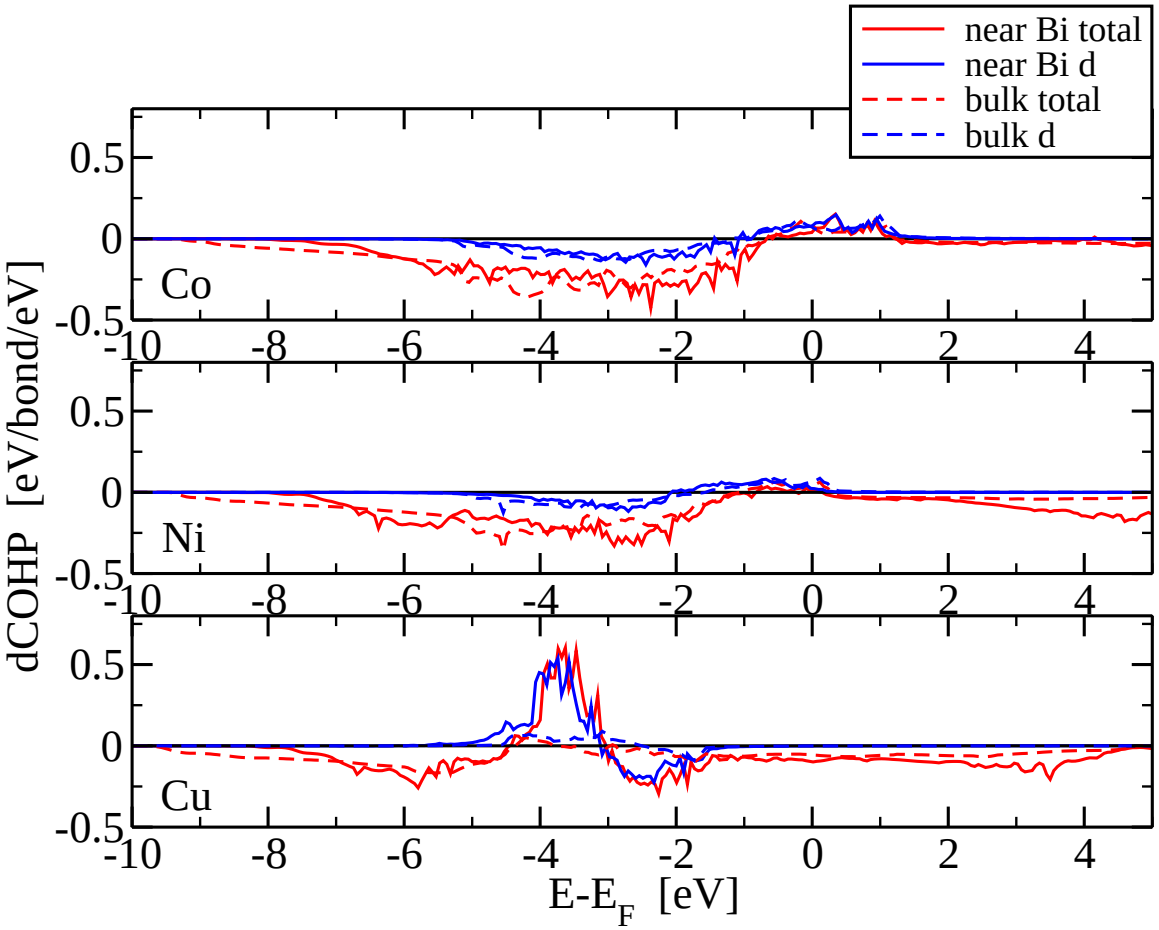

Figure 4.6: (Color online) Differential COHP of Metal-Metal interaction in the bulk and near to Bi. Negative is bonding while positive is antibonding. The Ni and Co results are the summation of two spin components. The dashed green line is the x axis. The zero in x axis is the Fermi energy.

The results of Bi bilayer at TM GBs are shown in Table 4.5. Vibrations leave the sign of ΔH unchanged for these GBs.

4.4 Conclusion

In conclusion, we have studied Bi segregation at Co, Ni and Cu low energy $\Sigma 3(111)$ and high energy $\Sigma 5(120)$ GBs using density functional theory. Our results reproduce

GB	Co	Ni	Cu
Σ 3(111)	0.089(0.099)	0.037(0.045)	0.030(0.040)
Σ 5(120)	0.012(0.004)	-0.043(-0.054)	-0.005(-0.009)

Table 4.5: $\Delta F(T)/A$ of Bi bilayer at TM GBs, units are eV/Å^2. Values in parenthesis are $\Delta H/A$.

the experimental result that Bi does not form film a at all in Fe GBs but forms a bilayer film ubiquitously at Ni high energy GBs, and in a much narrower chemical potential window at Cu high energy GB. The difference between these metals can be explained by the localization of 3d orbitals and also the loss of magnetism near the GB of Co (and presumably Fe). Moreover, Bi on Cu GB also increases the strength of antibonding, as confirmed by COHP calculation. We propose a model to predict the stability of Bi bilayer at various Ni GBs. Combining with the EAM GB energies from Reference [115], the model suggests Bi bilayer is not thermodynamically stable on (111) twist CSL GBs but should be stable in most (100) twist CSL GBs.

4.5 Appendix

4.5.1 A1. Bi bilayer on Fe Σ5(012) GB

We calculated Bi bilayer enthalpy on Fe Σ5(012), a high energy GB which is created by cleaving the BCC bulk along the (012) plane and rotating one grain around [001] by 53.1^o and rejoining the two parts. Our calculated GB energy is 0.098 eV/Å^2, close to the GB energy 0.104 eV/Å^2 of the lowest energy structure in the literature [118]. We first studied Bi monolayers on Fe (012) surfaces and then calculated bilayer films on the GB with the stable surface structure at two sides of the GB plane. We used 10 layers of Fe at each side of the Bi film. The relaxed structure is shown in Fig. 4.7. The lowest ΔH/A is +0.017 eV/Å^2 and including vabriations as in Eqn. 4.5 and 4.7

the $\Delta F/A$ is +0.016 eV/ Å^2 at 1000 K for bilayer films, which are large and positive indicating that the Bi bilayer is not stable even on this high energy GB.

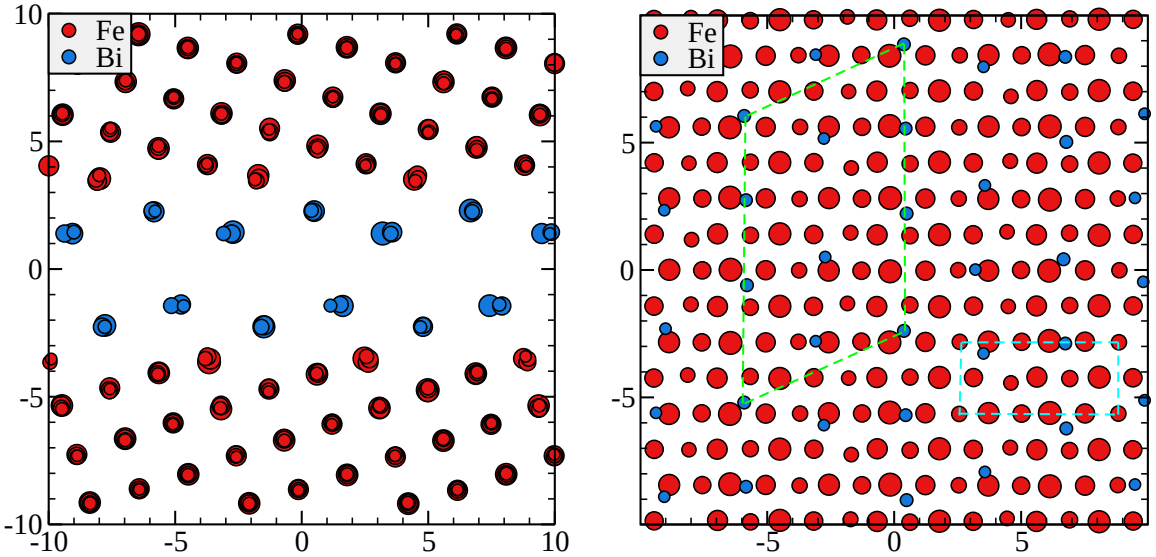

Figure 4.7: (Color online) Side view (left) of relaxed Bi bilayer at Fe Σ5(012) GB and top view (right) of Bi monolayer on one side of the GB plane. The cyan cell is the Fe GB unit cell, the green cell is the Bi segregated GB unit cell. Atom size indicates depth (large below small). Length units are in Å.

4.5.2 A2. Convergence with respect to number of Ni layers

To check whether the slabs in our calculations are thick enough to avoid artificial interaction between the terminating surfaces of the slabs and the grain boundaries in the center of the slabs, we calculate enthalpy of formation of Bi films at Ni Σ5(210) GB with different slab thicknesses. As seen in Fig. 4.8, ΔH oscillates for different slab thickness due to the quantum size effect [119] which is less than 0.005 eV/ Å^2 for 1, 2 and 4 layer Bi films. For the trilayer Bi film, the oscillation is exaggerated by the fact that the trilayer structure is not stable. The 12 layer Ni slab is thus thick enough for our study that concentrates on monolayer and bilayer films.

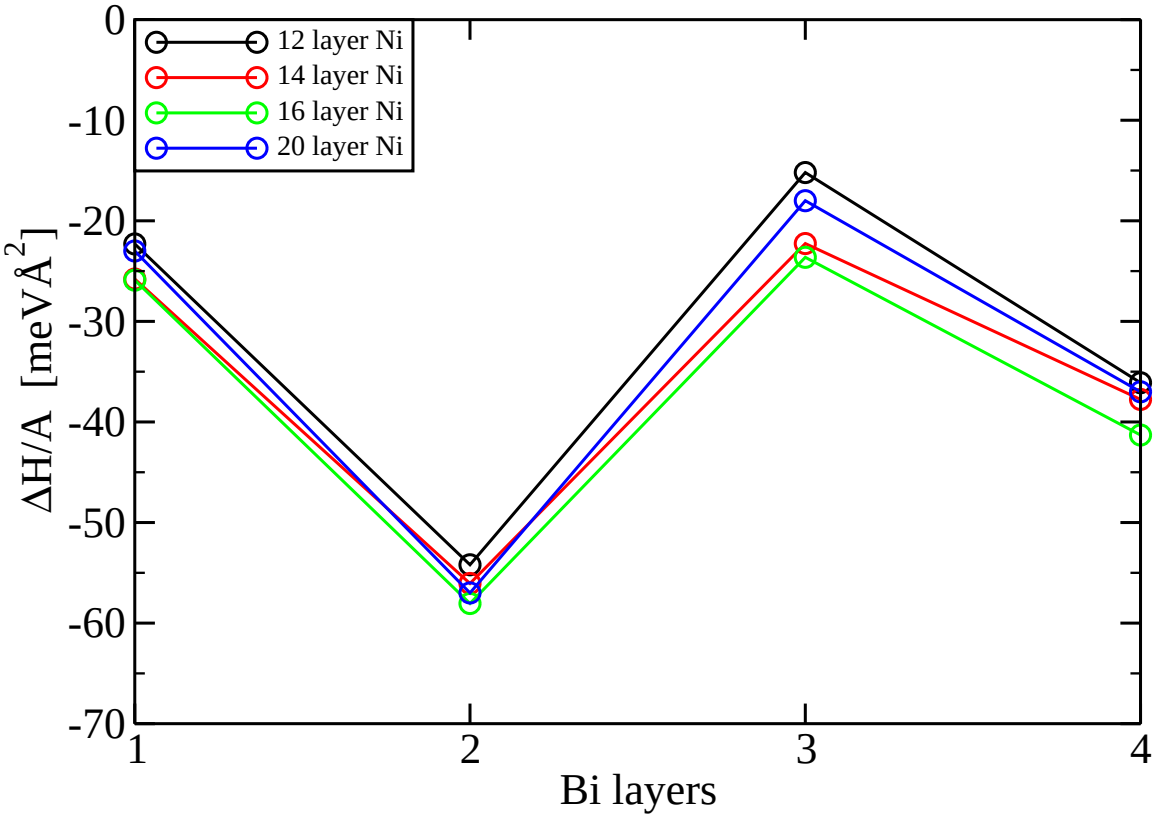

Figure 4.8: (Color online) Convergence with respect to the number of Ni layers in calculation of Bi bilayer at Ni Σ5(210) GB.

Chapter 5

Boron Carbide thermodynamics with Machine Learning methods

5.1 Introduction

Density functional theory (DFT) can accurately determine the total energies of crystals. However, DFT is time consuming and scales as the cube of the number of atoms. It is thus generally infeasible to directly use DFT for energy predictions in the Monte Carlo (MC) simulation of phase transitions, which require many evaluations of the energy of very large structures. Interatomic potentials [64], which typically fit the DFT energies as a function of the positions of the atomic nuclei, can be quickly evaluated to predict approximate energies. Cluster expansions [120, 121], which represent the energy as a sum of pair, triplet and higher-body interactions, provided a physically motivated and systematically improvable form for such a fit. However, the number of necessary terms can grow quite rapidly for complex crystal structures with many inequivalent positions, so this approach has been most successful when applied to regular lattice structures. We notice that certain information in the higher order terms like triplets can be expressed as nonlinear functions of pairs. This motivates our study with machine learning (ML) methods such as regression models that

can capture complex nonlinear interactions. ML methods have been used in various solid state physics problems [122, 123, 124, 125]. Interatomic potentials fitted with ML methods are generally more accurate and thus can be more useful for physical simulations [126, 127, 128, 129].

Boron carbide is an extremely hard and very light material with wide range of applications [63]. Despite its importance, the phase diagram of boron carbide is not precisely known. Its complex structure features 12-atom icosahedra and 3-atom chains and includes intrinsic disorder. It is difficult to equilibrate because of its strong covalent bonds. The small difference between the atomic numbers of boron and carbon make precise composition hard to measure. Because of their chemical similarity, substitutional disorder is prevalent, in particular among the so-called polar sites of the icosahedra. Two major problems exist in the widely accepted experimental boron carbide phase diagrams [130, 131]: 1) the solubility range of carbon is given as $0.090 \leq x_C \leq 0.192$, while the DFT-predicted ground state has composition B_4C with $x_C = 0.200$; 2) the boundaries of the composition range are temperature-independent, which is thermodynamically improbable. Since experimental measurement is not reliable at low temperature (say, $T < 1000$ K), computer simulation can help resolve these problems.

In this study, we exploit several ML methods to fit the interatomic potential of boron carbide and use the potential to perform MC simulations. A previous study [132], fit a linear model of pair interactions for structures with $x_C = 0.200$ and studied phase transitions at this high carbon limit. In this paper, instead of fixing $x_C = 0.200$, we allow arbitrary substitutions and swaps between boron and carbon among the polar sites, thus extending the carbon concentration from a lower limit of $B_{13}C_2$ ($x_C = 0.133$) with no upper limit. We fit the DFT energies with machine learning methods including L_1-penalized polynomial regression, neural network (NN), Gaussian process (GP) and support vector regression (SVR). We find the GP has smallest prediction error (0.31meV/atom), which is 33% less than the linear

model. We then perform Monte Carlo simulations with a linear regression model, a restricted polynomial regression model and a mixed-kernel Gaussian process model. The three energy models qualitatively agree with each other and indicate a phase transition at low temperature and high carbon chemical potential.

5.2 Methods

5.2.1 DFT calculations

Our calculation methods are similar to our previous study [132], namely electronic density functional theory utilizing PAW potentials [96, 97] in the PBE [77] generalized gradient approximation with default energy cutoffs using VASP [94, 95]. We calculate the fully relaxed total energies of 597 structures with supercell sizes $2 \times 2 \times 2$ (120 atoms) through $4 \times 4 \times 4$ (405 atoms). The majority of the sampled structures were created through Monte Carlo simulations between T =400 and 2000K based on preliminary interaction models. The data set to be fit consists of the enthalpies of formation of individual structures relative to the tie-line joining the ground states $B_{13}C_2$ and B_4C.

5.2.2 Supervised Regression Models

Linear model

One way of modeling the energies of structures is using cluster expansion [120, 121, 133, 134]. This approach is appealing because the relaxed energy is a function of the initial assignment of carbon atoms to polar sites, resulting in a lattice gas-type model. That is, only carbon positions must be specified, as boron necessarily occupy the remaining sites. However, due to the complexity of the boron carbide structure (a 15-atom basis) and the low density of polar carbons (typically 0-2 carbons among the 6 polar sites per cell), there are too many triplets and higher order clusters to be

included. A length cutoff of $R_c = 6.58$ Å would result in 427 triplets. One feasible approximation is to truncate the expansion at the pairwise level, resulting in 23 pairs with separation up to R_c. Our linear model (LM) based on this approximation is

$$E(\mathbf{N}) = E(N_0, ..., N_{23}) = E_0 + \sum_{i=0}^{23} \beta_i N_i, \tag{5.1}$$

where N_0 is the number of polar carbon in the structure and the remaining N_i's are the different pairs. The set $\{N_i\}$ can be considered as a 24-dimensional vector $\mathbf{N}$. Appendix A1 presents some characteristics of the data set and its dependence on $\mathbf{N}$.

L_1-penalized polynomial model

A polynomial model directly generalizes the linear model in Eq. 5.1. Due to the limited size of the data set, we choose a second order polynomial model (PR2),

$$E(\mathbf{N}) = E(N_0, ..., N_{23}) = E_0 + \sum_{i=0}^{23} \beta_i N_i + \sum_{j=0}^{23} \sum_{k=j}^{23} \gamma_{jk} N_j N_k, \tag{5.2}$$

which fully characterizes the second order interactions between numbers of pairs. This model contains 325 parameters. To avoid overfitting and perform feature selection, we add an L_1 norm penalty term. The resulting optimization problem is,

$$\min_{\theta} \sum_{m=1}^{M} \frac{1}{2} (E_m^{DFT} - E(\mathbf{N}_m; \theta))^2 + \lambda \|\theta\|_1, \tag{5.3}$$

where θ is the collection of all parameters, E_0, $\{\beta_i\}$ and $\{\gamma_{jk}\}$. E_m^{DFT} is the DFT calculated energy of the mth structure, $\mathbf{N}_m$ is its 24 dimensional feature vector, M is the size of the training set and λ is a tuning parameter. In this paper, we shall use i, j and k as indices for features, and l, m and n as indices for samples.

Neural network

In our neural network, the input layer contains 24 nodes corresponding to the components of $\mathbf{N}$. We choose 1-2 hidden layers of 1-10 nodes with nonlinear activation

functions like "tanh" and "sinh" in the hidden layers. The single node output layer utilizes a linear function. A Bayesian regularization for the model parameters reduces overfitting. We use the Matlab Neural Network Toolbox [135] with default starting coefficients and regularization parameters. A detailed description of neural networks can be found in [136].

Gaussian process

In GP, we assume the energies of structures are Gaussian distributed,

$$\begin{pmatrix} E_{\text{train}} \\ E_{\text{pred}} \end{pmatrix} \sim \mathcal{N}\left(\mu, \Sigma\right), \text{ with } \Sigma = \begin{pmatrix} \Sigma_{tt} & \Sigma_{tp} \\ \Sigma_{tp}^T & \Sigma_{pp} \end{pmatrix}, \tag{5.4}$$

where the E_{train} and E_{pred} vectors denote the energies of training structures and structures whose energies to be predicted (predicting structures) respectively, $\mathcal{N}$ is a normal distribution with mean μ (set to zero in later derivation for simplicity), and Σ is the covariance matrix. The mth row and nth column of Σ is,

$$\Sigma_{mn} = k(\mathbf{N}_m, \mathbf{N}_n), \tag{5.5}$$

where $\mathbf{N}_m$ and $\mathbf{N}_n$ are the feature vectors of the mth and nth structure respectively. The kernel function $k(\mathbf{N}_m, \mathbf{N}_n)$ characterizes the similarity between feature vectors, and therefore structures. In our study, we use and compare the polynomial kernel $(1 + \beta \mathbf{N}_m \cdot \mathbf{N}_n)^d$, the Gaussian kernel $\exp(-\|\mathbf{N}_m - \mathbf{N}_n\|_2^2/\gamma^2)$, and the Laplacian Kernel $\exp(-\|\mathbf{N}_m - \mathbf{N}_n\|_1/\gamma)$.

A constant variance term δ^2 is added to the kernel when $m = n$ to model the noise. The DFT energy is precise and thus lacks noise. A perfect model containing all relevant inputs would in principle precisely fit the DFT energy. However, since our features only represent a subset of the structural information, the DFT energies are noisy in the subspace spanned by the features. We thus need variance δ^2 to model the noise. The parameters β, d, γ and δ in the kernels are called hyperparameters. We can optimize these hyperparameters by maximizing the likelihood of the training

data, which is a convex optimization problem that can be efficiently solved [136]. We use the GPML Toolbox [137] to perform our GP model fitting and testing.

Under the assumptions of GP, the conditional distribution of predicted energy given the training data is Gaussian. We take the mean value of this distribution as the predicted energy. More explicitly, for a new structure with feature vector $\mathbf{N}_l$, the predicted energy is,

$$E(\mathbf{N}_l) = \sum_{m=1}^{M}\sum_{n=1}^{M} k(\mathbf{N}_l, \mathbf{N}_m)(\Sigma_{tt}^{-1})_{mn} E_{\text{train,n}}. \tag{5.6}$$

Moreover, GP also provides the variance of the predicted energy which implies the accuracy or confidence of the prediction, which is

$$\sigma^2(\mathbf{N}_l) = k(\mathbf{N}_l, \mathbf{N}_l) - \sum_{m=1}^{M}\sum_{n=1}^{M} k(\mathbf{N}_l, \mathbf{N}_m)(\Sigma_{tt}^{-1})_{mn} k(\mathbf{N}_n, \mathbf{N}_l). \tag{5.7}$$

To illustrate the properties of GP, the left panel of Fig. 5.1 shows a toy example of fitting a one dimensional function. The fitted nonlinear function captures the local properties of the data. Moreover, the fit provides the standard error of the prediction, where large standard error indicates small data density in the nearby region or large extrapolation. The standard errors of prediction can be used to check whether the data well sample the feature space, and to guide us in generating training structures for poorly represented regions.

Support vector regression

In SVR [138] the fitted function $E(\mathbf{N}) = \sum_i \omega_i \cdot \Phi_i(\mathbf{N}) + b$ minimizes the target function,

$$C\sum_{m=1}^{M} \max(0, |E(\mathbf{N}_m) - E_m^{\text{DFT}}| - \epsilon) + \frac{1}{2}\|\boldsymbol{\omega}\|_2^2, \tag{5.8}$$

where C and ϵ are positive real numbers, $\{\Phi_i(\mathbf{N})\}$ is a collection of chosen functions of $\mathbf{N}$, and $\boldsymbol{\omega}$ and b are fitting parameters. As shown in the right panel of Fig. 5.1, the errors of points within the ϵ-tube are not counted in the target function, which

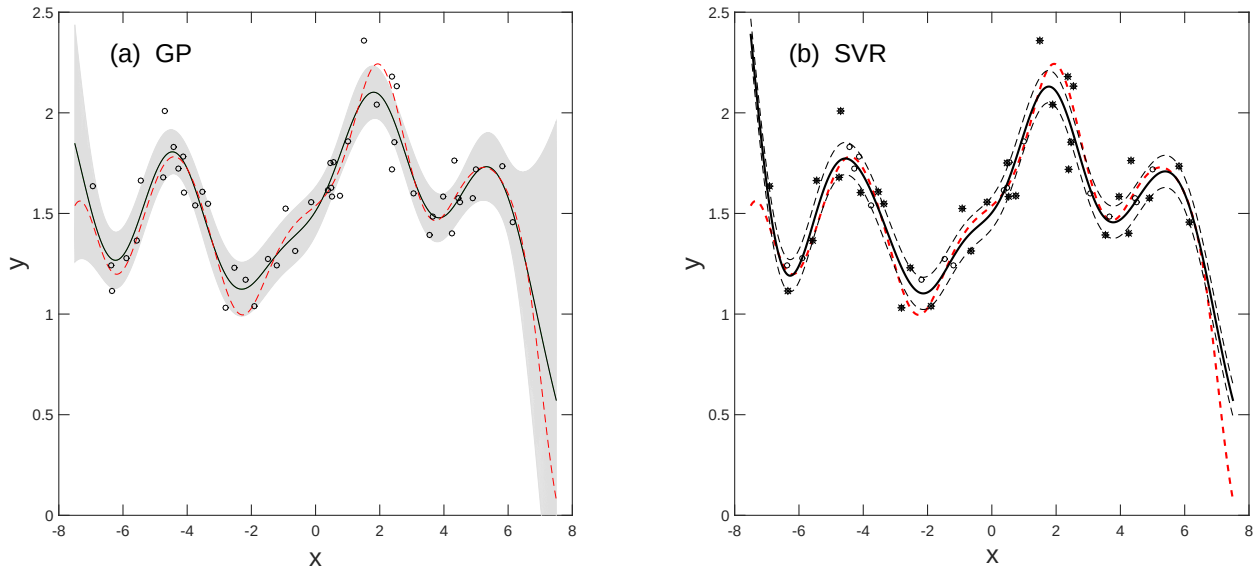

Figure 5.1: (a) GP and (b) SVR fits of a toy one-dimensional function. The dashed-red curve is the ground truth function. A "o" denotes a data point which is drawn randomly from the ground truth function and added with Gaussian noise. The black solid lines in both panels are the fitted functions. (a) The shaded region lies within two standard error of the GP prediction (95% confidence interval). (b) The dashed curves are the boundaries of the ϵ-tube. The "o" points with "*" at the centers are support vectors.

is thus insensitive to the intrinsic small noise in the energies. The points outside of the ϵ-tube only introduce linear penalty to the target function, which is more robust to outlier than least square error fit.

We can relax the constraints associated with the tube to obtain a dual form of SVR in which the energy prediction is

$$E(\mathbf{N}_l) = \sum_{m=1}^{M} \alpha_m k(\mathbf{N}_l, \mathbf{N}_m) + b, \tag{5.9}$$

where only data points on or outside the ϵ tube have nonzero α values, and are called support vectors. b is a constant that can be calculated by support vectors.

One advantange of SVR is it transforms the features $\mathbf{N}$ to new features $\Phi_i(\mathbf{N})$, more suitable for fitting. However, $\{\Phi_i(\mathbf{N})\}$ might be a high (or even infinite) dimensional vector. That is hard to use in practice. In this dual form, instead of $\{\Phi_i(\mathbf{N})\}$, only the kernel function $k(\mathbf{N}_l, \mathbf{N}_m) = \sum_i \Phi_i(\mathbf{N}_l)\Phi_i(\mathbf{N}_m)$ is needed to train the model and make predictions. The possible kernel functions are similar as in GP, which are flexible and easy to use. We use the LIBSVM Toolbox [139] to perform our SVR model fitting and testing.

5.2.3 Cross validation

We perform 5-fold cross validation (CV) to evaluate our models. In 5-fold CV, the data is randomly divided into 5 sets. In every validation, we choose one set as the validation set and the rest as the training set. We train our model using the training set and predict the energies of the structures in the validation set. After such validations, we aquire the predicted energy of every structure in the dataset. We then calculate the CV root mean square errors (RMSE) of the structures, which is defined as,

$$RMSE = \sqrt{\frac{1}{M}\sum_{m=1}^{M}(E_m^{\mathrm{DFT}} - E_m^{\mathrm{predict}})^2}, \tag{5.10}$$

where M is the total number of structures in the dataset. CV RMSE mimics the generalization error, which is the standard error for predicting the energy of an unseen structure which is useful in comparing different models. Since ML models can be very complex, the fitting error can be very small while the CV error remains large, which is a sign of overfitting. Throughout this paper, we report the CV RMSEs and generalization errors, which are superior measures of model performance to fitting error.

5.2.4 Monte Carlo

Our Metropolis Monte Carlo simulations utilize a semi-grand canonical ensemble [140, 141, 142] in which we associate a chemical potential $\mu = \mu_C - \mu_B$ for the conversion of a polar boron to carbon. The physically meaningful range of μ extends from -0.55 to +0.14 eV at $T = 0$K. To circumvent difficulties arising from hysteresis near first order transitions, we apply replica exchange [143] along both the temperature and chemical potential (μ/T) axes. Data was collected on grids in the $(T, \mu/T)$-plane in the form of multidimensional histograms $H(x_C, E; T, \mu/T)$ then was analyzed using multiple histogram methods [144].

5.3 Results and analysis

We calculate the RMSEs of 5-fold CV to evaluate the models as shown in Table 5.1. Improvement is defined as the percentage decrease of RMSE compared to the linear model (LM, Eq. (5.1)). The second order polynomial regression with L_1 penalty (PR2, Eq. (5.2)) outperforms the linear model by a decrease of 20% in RMSE error. The RMSE minimizes at 197 nonzero parameters out of a possible 325. The neural network (NN) performs similarly to PR2 in CV. The best performing NN has 24 input nodes (features), one hidden layer of 3 or 4 nodes with "tanh" activation function and a single-node output layer with linear activation function. The nonparametric GP and SVR models (Eqs. (5.6) and (5.9)) decrease the CV error by around 33%. Since GP has a probabilistic interpretation, we choose the hyperparameters by maximizing the likelihood of the training data. However, SVR does not have such interpretation, thus we perform an extensive search over a grid of hyperparameters to find the set of hyperparameters that minimizes the 5-fold CV error.

The goodness of fit is shown in Fig. 5.2 by comparing the predicted energies of the validation sets in the 5-fold CV with the corresponding DFT energies. The points generally lie near the $y = x$ line. GP fits better than the linear model. To illustrate

MODEL	RMSE (meV/atom)	improvement
LM	0.48 ± 0.01	0%
PR2	0.39 ± 0.01	20±1%
NN	0.37 ± 0.01	24±1%
GP	**0.31 ± 0.01**	**33±1%**
SVR	0.32 ± 0.01	32±1%

Table 5.1: RMSE of 5-fold cross validation and improvement of different models. The standard error of these quantities are obtained from the statistics of ten repetitions of cross validation.

the fine details, we only show structures with energies up to 13.3 meV/atom rather than the maximum energy of around 40 meV/atom present in the full data set. For comparison, the mean energy at a high temperature of $T = 2500$K is around 10 meV/atom in the high carbon limit. To further compare the performance of linear model and GP, the residuals of the validation sets in the 5-fold CV are shown in Appendix A2. The residuals of the linear model are generally larger than residuals of GP. Patterns exist in the residuals which indicate underfitting, and these are more obvious in the linear model.

Since we need to predict energies of large cell structures in our Monte Carlo simulation, we also study the performance of our models when generalizing to large cells. We use our $2 \times 2 \times 2$ and $3 \times 3 \times 3$ cell structures as the training set and the remaining 12 larger cell structures ($3 \times 3 \times 4$ and $4 \times 4 \times 4$) as the generalization set. The generalization error are 0.43, 0.46 and 0.86 meV/atom for SVR, GP and the linear model respectively. All these models have larger generalization errors than the CV errors of the whole dataset, but this difference is less pronounced for SVR and GP.

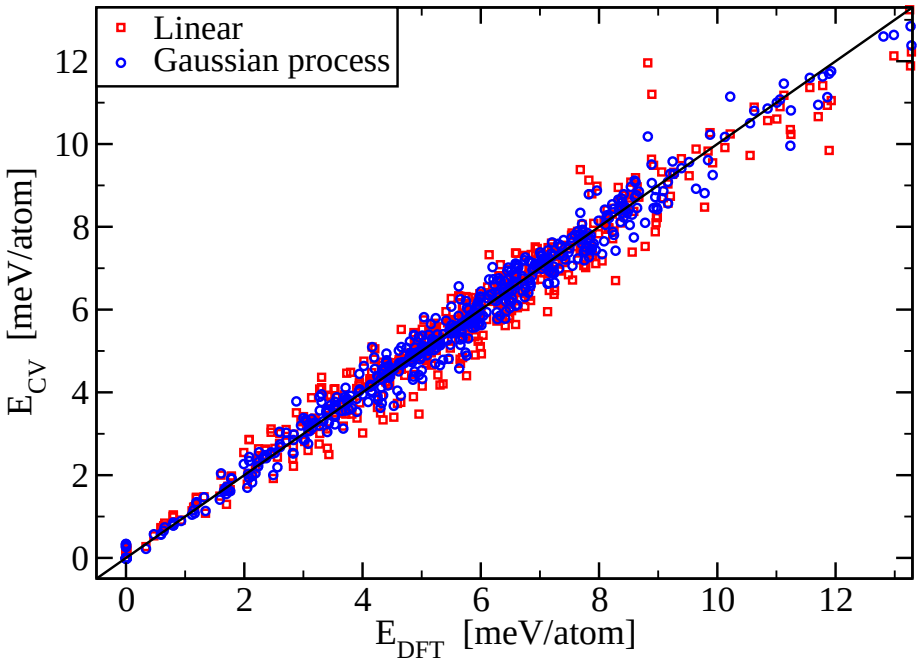

Figure 5.2: (Color online) The predicted energies in 5-fold CV vs the ground truth DFT energies. The black line is $y = x$. Red points are from linear model and blue from GP predictions.

5.3.1 Model Selection and Acceleration

We perform a greedy stepwise feature selection, as shown in Fig. 5.3 where the 24 features yield the smallest CV errors. Note that the CV error is still decreasing near 24 features, which suggests that our description of the structures with these 24 features is insufficient and further improvement could be made by adding more effective features. Moreover, Fig. 5.3 shows that both GP and SVR CV errors are insensitive to the choice of kernel.

Since the CV error is insensitive to the choice of kernel, we use GP with polynomial kernel of degree $d = 2$ to predict the energies quickly enough for the Monte Carlo themodynamics simulation. In Metropolis Monte Carlo simulation, structures are generated and energies are claculated sequentially and energies. Directly using Eq. 5.6 or Eq. 5.9 to predict is slow since to predict one energy we have to sum over the whole

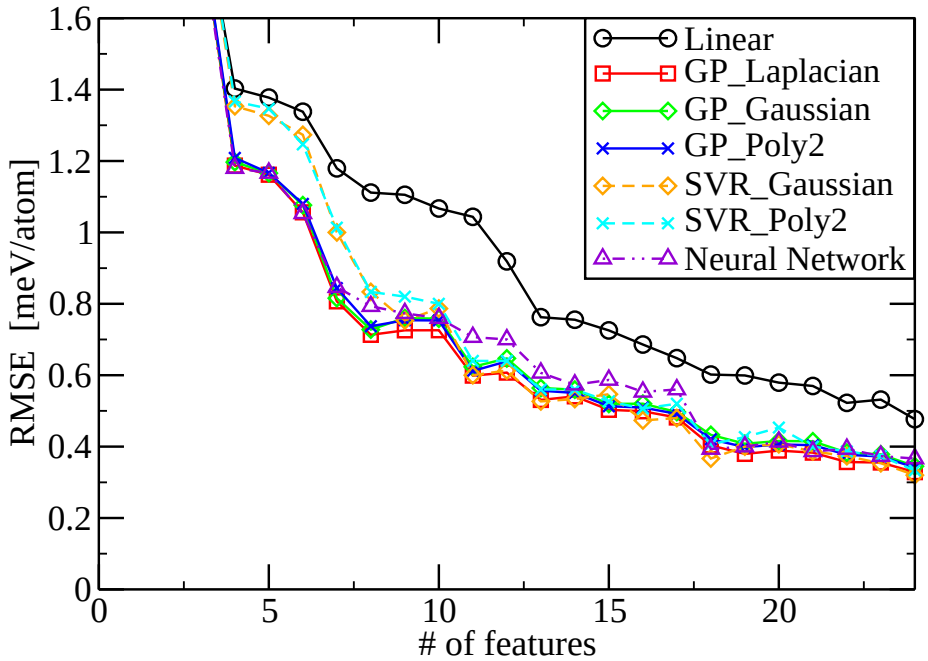

Figure 5.3: (Color online) RMSE of linear model, GP, NN and SVR vs number of features. The black curve is linear model, solid curves are GP with different kernels. Dashed curves are SVR with different kernels. The purple dot-dashed curve is NN.

training set (~ 600) or all support vectors (~ 400). It thus takes several hundreds of inner products of 24-dimensional vectors to predict one energy. However, with polynomial kernel of degree two, we can use a change of summation order trick to accelerate the prediction, which is essentially rewriting the prediction in a parametric form.

Define $\alpha = \Sigma_{tt}^{-1} E_{\text{train}}$ which can be easily calculated offline before the Monte Carlo simulations, the GP energy prediction Eq. (5.6) can be rewritten as,

$$E(\mathbf{N}_l) = \sum_{m=1}^{M} \alpha_m k(\mathbf{N}_l, \mathbf{N}_m) = \sum_{m=1}^{M} \alpha_m (1 + \beta \mathbf{N}_l \cdot \mathbf{N}_m)^2 = c + \mathbf{v} \cdot \mathbf{N}_l + \mathbf{N}_l^T A \mathbf{N}_l, \quad (5.11)$$

where $c = \sum_{m=1}^{M} \alpha_m$, $\mathbf{v} = \sum_{m=1}^{M} 2\beta\alpha_m \mathbf{N}_m$ and the matrix $A = \sum_{m=1}^{M} \beta^2 \alpha_m \mathbf{N}_m \mathbf{N}_m^T$. Since c, $\mathbf{v}$ and A can be calculated in advance using the training set, the calculation to predict one structure only needs 25 vector multiplications, which is 30 times fewer than directly using Eq. 5.6. In practice, the prediction is fast enough for Monte Carlo

simulation. The same trick works for SVR also.

5.4 Monte Carlo simulation

During MC simulation, we find that the GP model in Eq. 5.11 predicts unphysically low energies for some structures. This is because the dataset size is limited and the distributions of the numbers of long bonds (e.g. the values of N_i for large i) is large, leading to unreliable extrapolation. We found two solutions to this problem.

First, we modify our GP model by defining a mixed kernel that captures interactions between carbon concentration (N_0) and the three types of shortest bonds while ignores other interactions. Define $\mathbf{N}_{\parallel} = (N_0, N_1, N_2, N_3)$ and $\mathbf{N}_{\perp} = (N_4, N_5, ..., N_{23})$, our mixed Gaussian/linear kernel is,

$$k(\mathbf{N}, \mathbf{N}') = \sigma_f^2 \exp(\frac{||\mathbf{N}_{\parallel} - \mathbf{N}'_{\parallel}||_2^2}{2l^2}) + \sigma_p^2(\mathbf{N}_{\perp} \cdot \mathbf{N}'_{\perp} + c), \tag{5.12}$$

where σ_f, l, σ_p and c are hyperparameters. This kernel has RMSE 0.36± 0.01 meV/atom in 5-fold CV which is slightly higher than the GP with full Gaussian kernel.

Second, since we observed that the GP model with polynomial kernel of degree $d = 2$ is similar to a parametric polynomial regression of degree two (PR2), we fit less flexible PR2 models with only short-bond interactions. We start with the 24 features N_i and add the products $N_i N_j$ successively as new features for $i = 0, 1, 2$ and $j = i, i+1, ..., 10$. The 41-feature PR2 model has smallest CV error, which is 0.35±0.01 meV/atom, similar to the mixed-kernel GP.

Simulations of a variety of supercell sizes were performed using energies predicted by the linear model, the mixed-kernel GP, and the 41-feature PR2 model. Resulting histograms of energies of 6×6×6 cells at $T = 600K$ and different μ/k_BT's are shown in Fig. 5.4. Rapidly changing histograms, or multiply-peaked histograms indicate a possible phase transition. The histograms of these models are similar in trend, with rapid change between μ/k_BT=0.5 and 1.0.

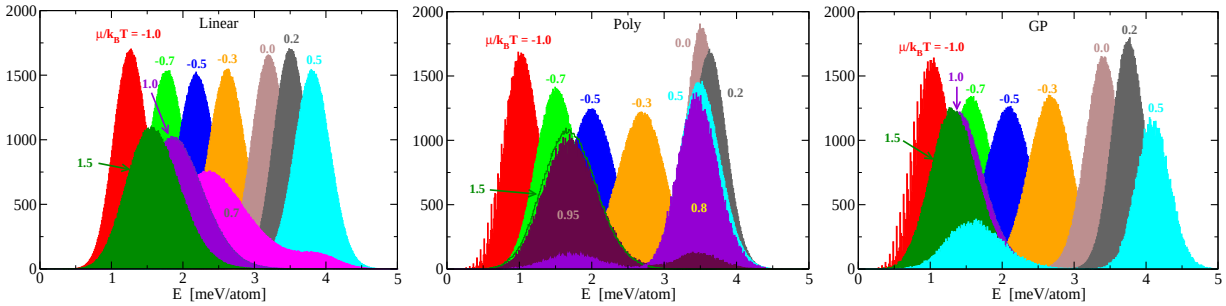

Figure 5.4: (Color online) Energy histograms of the linear model (left), the 41-feature PR2 model (middle), and the mixed-kernel GP (right).

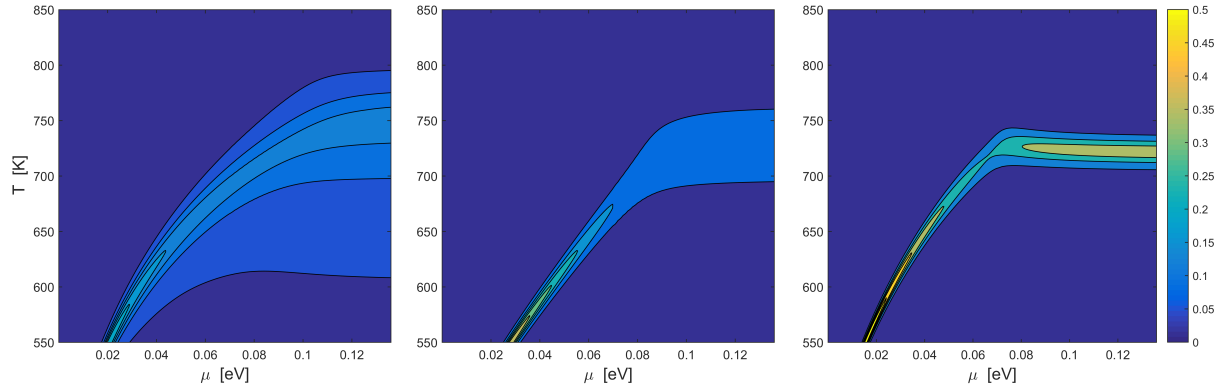

Figure 5.5: (Color online) The MC simulated heat capacity of boron carbide using the linear model (left), the 41-feature PR2 model (middle), and the mixed-kernel GP (right).

Based on the histograms in the MC simulations, the heat capacities of boron carbide are calculated using the multi-histogram method [145, 144, 132], as shown in Fig. 5.5. At infinite cell size, diverging heat capacity indicates a phase transition. We analyzed the scaling of heat capacity with 4×4×4, 5×5×5 and 6×6×6 cells. The peaks of the heat capacities in all three models increase quickly and do not greatly alter their positions. All these models thus suggest a first order phase transition, which corresponds well with the fast evolving histograms in high μ/k_BT, seen in Fig. 5.4. This phase transition is consistent with a previous study [132] at 20% carbon limit. The mixed-kernel GP, and the 41-feature PR2 model more accurately predict

the energies, thus should be quantitatively more reliable. The previously found [132] second order transition is hard to see using heat capacity.

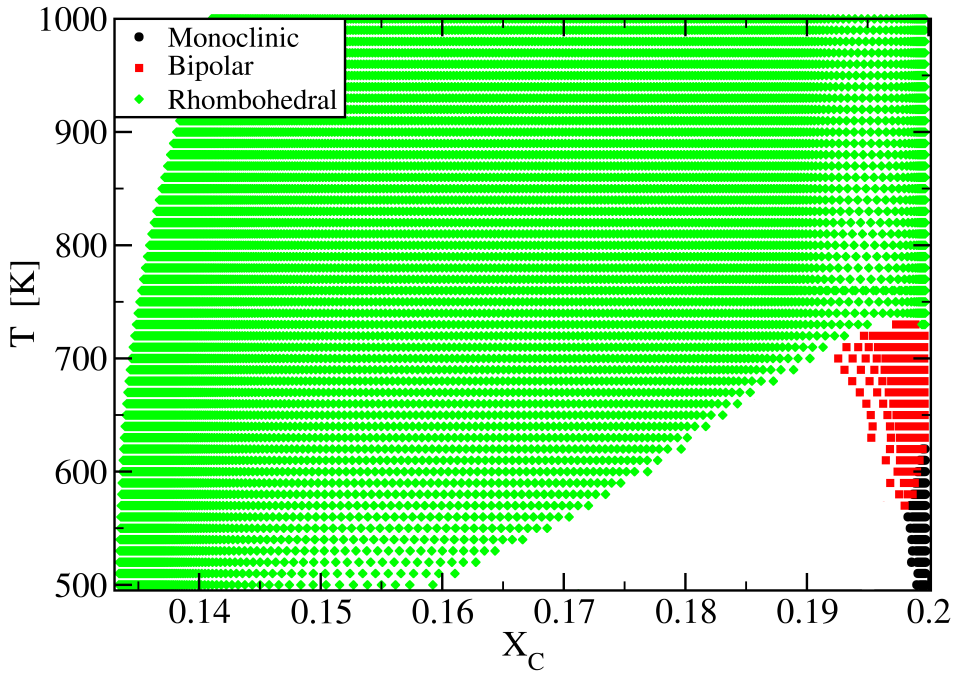

Figure 5.6: (Color online) Boron carbide phase diagram in the (X_C, T) plane. Black region is the Monoclinic phase, red is the Bipolar phase, and green is the Rhombohedral phase.

Fig. 5.6 shows the phase diagram of boron carbide from our MC simulation with the mixed-kernel GP interaction model. Three phases appear [132]: 1) Rhombohedral phase, where carbon occupies the six polar sites on the icosahedra with equal probability; 2) Bipolar phase, where the 3-fold rotational symmetry is broken but the two poles remains equivalent; 3) Monoclinic phase, the 2-fold symmetry between the two poles is broken in addition to the 3-fold rotational symmetry. At lower temperature, the Rhombohedral phase (green) shrinks gradually to the point $X_C = 0.133$ as $T \to 0$ K, and the Monoclinic phase (black) shrinks gradually to the point $X_C = 0.20$ as $T \to 0$ K. The rhombohedral phase extends down to $X_C = 0.133$ at all temperatures. The existence of three phases agrees with a previous restricted study at

20% carbon composition [132]. A comprehensive study of the phase transitions and analysis of the order parameters will be reported in a forthcoming paper.

5.5 Conclusion

In this study we construct ML-based interatomic potentials of boron carbide and perform MC simulations with these potentials. We started with a cluster-expansion motivated linear model, then exploit the nonlinear interaction between features using parametric models like L_1-regularized polynomial model and neural network, and nonparametric models like Gaussian process and support vector regression. Our result shows that L_1-regularized polynomial model and neural network decrease the cross validation error by 20%, while the nonparametric models achieve 33% improvement. The accuracy of nonparametric models is insensitive to the choice of kernel in our problem.

We perform MC simulation with gaussian process (GP). Directly using polynomial-kernel GP leads to wrong ground states. Augmenting our data set to include structures with large predicted uncertainty resulted in decreased CV RMSE but did not alleviate the problem of false ground states. Instead we developed a mixed-kernel GP model and a restricted polynomial regression model to fix it. The specific heat obtained from MC simulations with these models and the linear model all clearly indicate a phase transition at high carbon concentration and low temperature. Three phases are identified from our simulations and agrees well with a previous restricted study at 20% carbon composition. To improve the models, local properties of atoms could be included in the models, rather than just using the total numbers of pairs in the structure. Another possible improvement is to include numbers of triplets. Including the local features or triplets might require more data to avoid extrapolation problems.

5.6 Appendix

5.6.1 A1. Data Exploration

Histograms and pairwise scatter plots of three selected features (polar C concentration x, number of nearest C-C bonds N_1, number of second nearest C-C bonds N_2) and energy E are shown in Fig. 5.7. All the variables are skew distributed due to the physical distribution of the boron carbide structures. For example, our structrues are weighted towards few short bonds N_1 and low energy E. Moreover, the scatter plots show the features are correlated but not collinear and that the energy correlates with these three features. For example, low energy correlates with low N_1. The variances of energies at different feature values are not the same. The scewed distributions and non-constant variances might bring difficulty to linear model and other models with similar assumptions.

5.6.2 A2. Residuals of Linear model and GP

The residuals of the linear model and the GP are compared in Fig. 5.8. The residuals of GP are smaller in magnitude, and less pronounced patterns exist in GP than in the linear model.

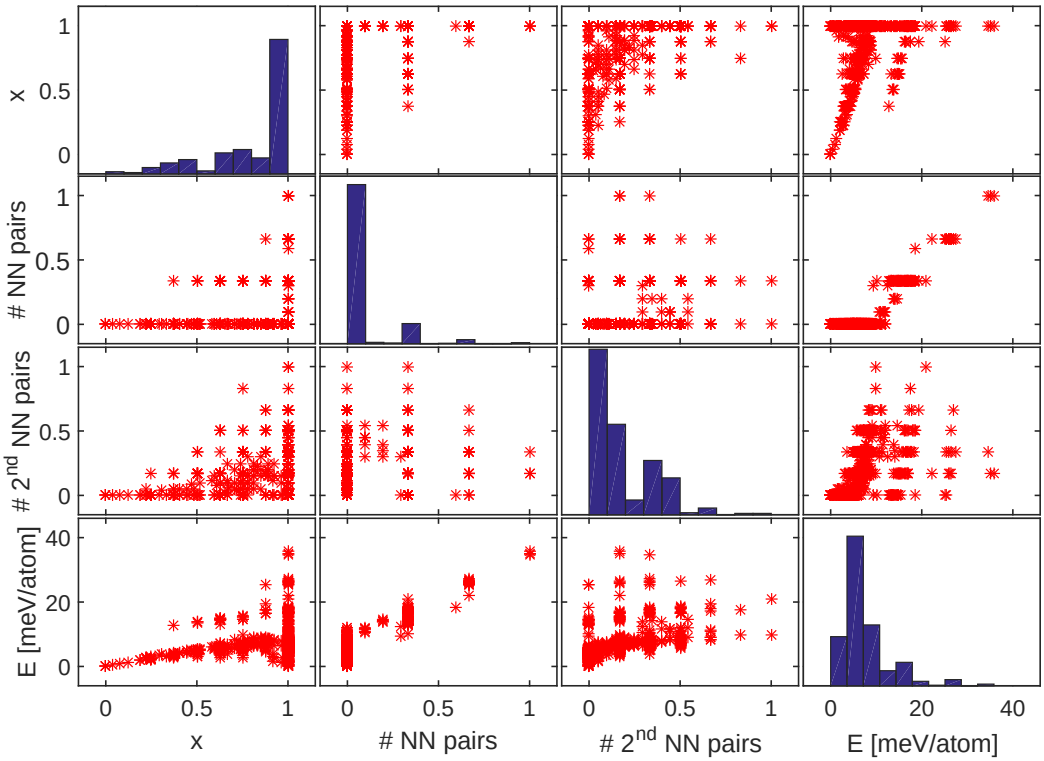

Figure 5.7: (Color online) Histograms (diagonal plots) and pairwise scatter plots (off-diagonal plots) of features and energies. The variables from left to right and from top to bottom are the polar C concentration x_C, number of nearest C-C bonds N_1, number of second nearest C-C bond N_2, and the DFT calculated energy E. All the three features are normalized. Every red star represents the value of one structure.

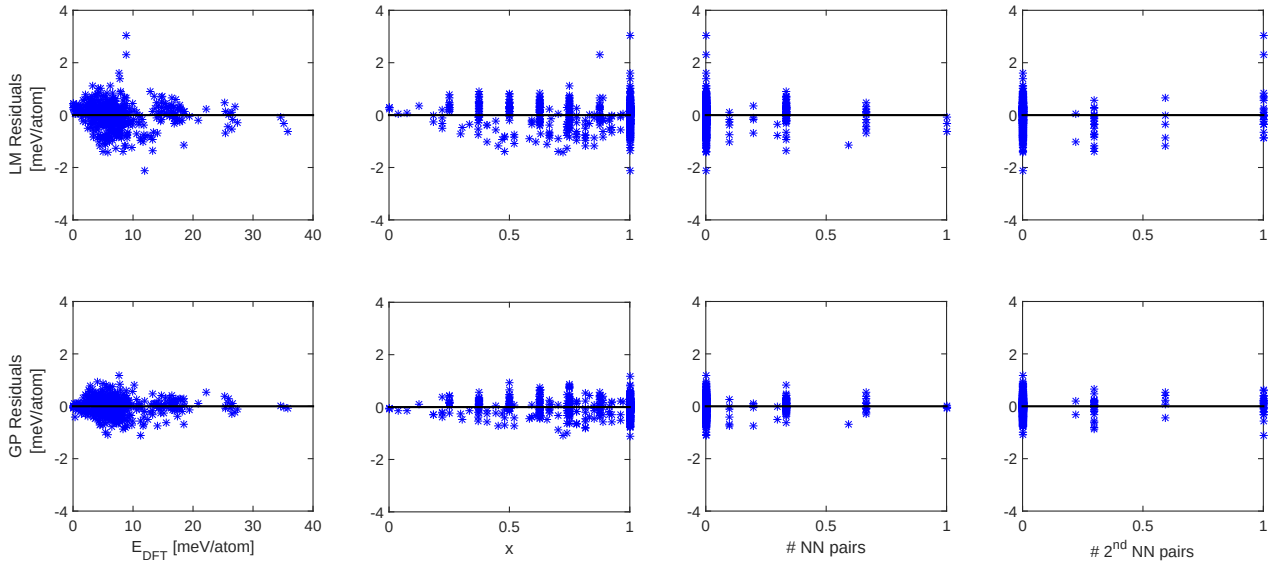

Figure 5.8: (Color online) Residuals of predicted energies in 5-fold CV of linear model (top) and GP (bottom). From left to right the x-axis represents the DFT energy, carbon concentration, number of nearest bonds and number of second nearest bonds, respectively.

Chapter 6

Summary and Future Work

6.1 Summary

This thesis focuses on our first-principles study of Bi on Ni(111) surface, at transition metal interfaces and bulk thermodynamics of boron carbide. We directly use DFT to study Bi film stability at Ni(111) surface and special grain boundaries. To study problems beyond the computational feasibility of DFT, we develop a thermodynamic model to study Bi film stability at general GBs and DFT/machine learning interaction models to study boron carbide phase diagram.

A recent experiment suggested that Bi forms hexagonal films on the Ni(111) surface, of heights one, three, five, and seven layers. The experimental group proposed a quantum size effect based on free electrons. To test this idea, we calculate the total energies of Bi on the Ni(111) surface using density functional theory. We find that the stabilities of the proposed hexagonal film structures disagree with the observed odd layer preferences, and the structures are mechanically destabilized by adding capping atoms which pucker the hexagonal layers. Furthermore, we find that a surface monolayer followed by rhombohedral films based on the bulk Bi structure are energetically more favorable than the proposed hexagonal films. These structures also favor odd numbers of layers, but owing to covalent chemical bonding rather than confinement

of free electrons.

Recent experiments suggest that Bi impurities segregate to form bilayer films on Ni and Cu grain boundaries (GBs) but do not segregate in Fe. To explain these phenomena, we study the total energies of Bi films on transition-metal (TM) $\Sigma 3(111)$ and $\Sigma 5(012)$ GBs using density functional theory. Our results agree with the observed stabilities. We propose a model to predict Bi bilayer stability at Ni GBs which suggests that a Bi bilayer (i.e. a pair of strongly bound surface monolayers) is not stable on (111) twist CSL GBs but *is* stable in most (100) twist CSL GBs. We investigate the interaction and bonding character between Bi and TMs to explain the differences among TMs based on localization of orbitals and magnetism, as well as evaluating the contribution of interfacial phonons at high temperature.

Total energies of crystal structures can be calculated to high precision using quantum-based density functional theory (DFT) methods, but the calculations can be time consuming and scale badly with system size. Cluster expansions of total energy as a linear superposition of pair, triplet and higher interactions can efficiently approximate the total energies but are best suited to simple lattice structures. To model the total energy of boron carbide, with a complex crystal structure, we explore the utility of machine learning methods (L1-penalized regression, neural network, Gaussian process and support vector regression) that capture certain non-linear effects associated with manybody interactions despite requiring only pair frequencies as input. The machine learning models reduce the predictive error by 20 - 33%. Our interaction models are combined with Monte Carlo simulations to evaluate the thermodynamics of chemical ordering. The specific heat obtained from different interaction models is qualitatively similar and indicates phase transitions. Three boron carbide phases are identified in agreement with a previous restricted study at 20% carbon composition [132].

6.2 Future Work

The long-term goal is to understand and predict complexions and to tailor material properties by complexion engineering. The first crucial step is to understand the structures of complexions and the conditions that stabilize them. For the surface complexion, an atomic-resolved experiment of Bi on Ni(111) is warranted to end the debate over the Bi surface structures and stability mechanism [2, 13]. For the GB complexion, although the bilayer complexion is observed, the exact complexion structures and their relation with complexion properties are still unknown. Structural modeling based on direct HAADF-STEM observation and combined with DFT verification is needed. Since a strong effect of additives on the formation of IGF has been demonstrated [44], the effect of additives on Bi (sub)nanometer complexions is also an attractive question. Complexion transitions like prewetting/premelting, faceting, roughening also remain to be observed and analyzed [41].

Analytical models have the advantage of representing the whole space of GB configurations, but lack accurate total energies and entropies, while DFT calculations can accurately deal only with small cell sizes. It is thus desirable to feed DFT calculated interaction parameters into analytical models. MC and MD simulations using empirical potentials successfully applied to Cu and Ag/Cu can in principle be used to study Bi/Ni and Bi/Cu complexion transitions, but only if accurate interaction potentials can be obtained. One approach is to develop DFT-based machine learning models, which are capable of learning atomic interactions from small-cell DFT calculations and generalizing to large cell simulations [127].

After the identification of three boron carbide phases, a detailed analysis of the phase diagram remains to be performed. In the analysis of phase diagram, we need to compare the order parameters from MC simulations and from low temperature expansions using exact DFT energies. Machine learning interaction models might also be improved by introducing physical weights in the fitting procedures or by other better descriptors.

Bibliography

[1] Chameli Panja, Mark E. Jones, John M. Heitzinger, Steven C. Gebhard, and Bruce E. Koel. Bi adsorption and poisoning on ni(100) surface as probed by co chemisorption. *The Journal of Physical Chemistry B*, 104(14):3130–3139, 2000.

[2] T. R. J. Bollmann, R. van Gastel, H. J. W. Zandvliet, and B. Poelsema. Quantum size effect driven structure modifications of bi films on ni(111). *Phys. Rev. Lett.*, 107:176102, 2011.

[3] L.-S Chang, E Rabkin, B.B Straumal, B Baretzky, and W Gust. Thermodynamic aspects of the grain boundary segregation in cu(bi) alloys. *Acta Materialia*, 47(1516):4041 – 4046, 1999.

[4] K. Wolski and V. Laporte. Grain boundary diffusion and wetting in the analysis of intergranular penetration. *Materials Science and Engineering: A*, 495(12):138 – 146, 2008. Fifth International Conference on High Temperature Capillarity HTC-2007, Alicante, Spain.

[5] B.B. Straumal, S.A. Polyakov, E. Bischoff, W. Gust, and B. Baretzky. Faceting of sigma 3 and sigma 9 grain boundaries in cu-bi alloys. *Acta Materialia*, 53(2):247 – 254, 2005.

[6] J. Luo, H. Cheng, K. M. Asl, C.J. Kiely, and M.P. Harmer. The role of a bilayer interfacial phase on liquid metal embrittlement. *Science*, 333:1730, 2011.

[7] P. Wynblatt and Zhan Shi. Relation between grain boundary segregation and grain boundary character in fcc alloys. *Journal of Materials Science*, 40(11):2765–2773, 2005.

[8] D. Udler and D. N. Seidman. Solute-atom segregation at symmetrical twist boundaries studied by monte carlo simulation. *physica status solidi (b)*, 172(1):267–286, 1992.

[9] Paul Wynblatt and Dominique Chatain. Solid-state wetting transitions at grain boundaries. *Materials Science and Engineering: A*, 495(1.2):119 – 125, 2008. Fifth International Conference on High Temperature Capillarity HTC-2007, Alicante, Spain.

[10] Timofey Frolov, David L. Olmsted, Mark Asta, and Yuri Mishin. Structural phase transformations in metallic grain boundaries. *Nat Commun*, 4(1899), 2012.

[11] T. Frolov, M. Asta, and Y. Mishin. Segregation-induced phase transformations in grain boundaries. *Phys. Rev. B*, 92:020103, Jul 2015.

[12] Stuart Golin. Band structure of bismuth: Pseudopotential approach. *Phys. Rev.*, 166:643–651, Feb 1968.

[13] Qin Gao and Michael Widom. First-principles study of bismuth films on the ni(111) surface. *Phys. Rev. B*, 88:155416, Oct 2013.

[14] Elizabeth A. Holm, David L. Olmsted, and Stephen M. Foiles. Comparing grain boundary energies in face-centered cubic metals: Al, au, cu and ni. *Scripta Materialia*, 63(9):905 – 908, 2010.

[15] J. Bardeen, L. N. Cooper, and J. R. Schrieffer. Theory of superconductivity. *Phys. Rev.*, 108:1175–1204, Dec 1957.

[16] R. B. Laughlin. Anomalous quantum hall effect: An incompressible quantum fluid with fractionally charged excitations. *Phys. Rev. Lett.*, 50:1395–1398, May 1983.

[17] K. S. Novoselov, Geim A. K., S. V. Morozov, D. Jiang, M. I. Katsnelson, I. V. Grigorieva, S. V. Dubonos, and A. A. Firsov. Two-dimensional gas of massless dirac fermions in graphene. *Nature*, 438:197–200, Dec 2005.

[18] M. Z. Hasan and C. L. Kane. *Colloquium* : Topological insulators. *Rev. Mod. Phys.*, 82:3045–3067, Nov 2010.

[19] P. A. M. Dirac. Quantum mechanics of many-electron systems. *Proceedings of the Royal Society of London A: Mathematical, Physical and Engineering Sciences*, 123(792):714–733, 1929.

[20] Qin Gao and Michael Widom. First-principles study of bismuth films at transition-metal grain boundaries. *Phys. Rev. B*, 90:144102, Oct 2014.

[21] C. Scott, M. Kaliszewski, C. Greskovich, and L. Levinson. Conversion of polycrystalline al 2o 3 into single-crystal sapphire by abnormal grain growth. *J. Am. Ceram. Soc.*, 85(5):1275–1280, 2002.

[22] J. Cho, M.P. Harmer, H.M. Chan, J.M. Rickman, and A.M. Thompson. Effect of yttrium and lanthanum on the tensile creep behavior of aluminum oxide. *J. Am. Ceram. Soc.*, 80(4):1013–1017, 1997.

[23] B. Joseph, M. Picat, and F. Barbier. Liquid metal embrittlement: A state-of-the-art appraisal. *The Eur. Phys. J.-Appl. Phys.*, 5:19–31, 0 1999.

[24] K. Wolski and V. Laporte. Grain boundary diffusion and wetting in the analysis of intergranular penetration. *Mater. Sci. Eng.: A*, 495(12):138 – 146, 2008.

[25] R.K. Viswanadham, T.S. Sun, and J.A.S. Green. Grain boundary segregation in al-zn-mg alloysimplications to stress corrosion cracking. *Metall. Mater. Trans. A*, 11(1):85–89, 1980.

[26] S.P. Knight, N. Birbilis, B.C. Muddle, A.R. Trueman, and S.P. Lynch. Correlations between intergranular stress corrosion cracking, grain-boundary microchemistry, and grain-boundary electrochemistry for alznmgcu alloys. *Corros. Sci.*, 52(12):4073 – 4080, 2010.

[27] Ming Tang, W. Craig Carter, and Rowland M. Cannon. Grain boundary transitions in binary alloys. *Phys. Rev. Lett.*, 97:075502, Aug 2006.

[28] M.P. Harmer. The phase behavior of interfaces. *Science*, 332:182, 2011.

[29] LawrenceE. Felton, ChristopherH. Raeder, and DavidB. Knorr. The properties of tin-bismuth alloy solders. *JOM*, 45(7):28–32, 1993.

[30] Huanqin Zhu, Jianqiang Hu, Yongguo Zhang, and Yiwei Fei. Extreme pressure properties and mechnism of bismuth naphthenate with sulfur containing additives. In Jianbin Luo, Yonggang Meng, Tianmin Shao, and Qian Zhao, editors, *Advanced Tribology*, pages 878–879. Springer Berlin Heidelberg, 2010.

[31] N. Marie, K. Wolski, and M. Biscondi. Intergranular penetration and embrittlement of solid nickel through bismuth vapour condensation at 700°c. *Journal of Nuclear Materials*, 296(1.3):282 – 288, 2001. 4th Int. Workshop on Spallation Materials Technology.

[32] B. Straumal and B. Baretzky. Grain boundary phase transitions and their influence on properties of polycrystals. *Interface Science*, 12(2-3):147–155, 2004.

[33] John W. Cahn. Critical point wetting. *The Journal of Chemical Physics*, 66(8), 1977.

[34] Ryo Kobayashi, James A. Warren, and W. Craig Carter. A continuum model of grain boundaries. *Physica D: Nonlinear Phenomena*, 140(1.2):141 – 150, 2000.

[35] James A. Warren, Ryo Kobayashi, Alexander E. Lobkovsky, and W. Craig Carter. Extending phase field models of solidification to polycrystalline materials. *Acta Materialia*, 51(20):6035 – 6058, 2003.

[36] Patrick R. Cantwell, Ming Tang, Shen J. Dillon, Jian Luo, Gregory S. Rohrer, and Martin P. Harmer. Grain boundary complexions. *Acta Materialia*, 62(0):1 – 48, 2014.

[37] Joongoo Kang, Greg C. Glatzmaier, and Su-Huai Wei. Origin of the bismuth-induced decohesion of nickel and copper grain boundaries. *Phys. Rev. Lett.*, 111:055502, Jul 2013.

[38] T. Frolov, S. V. Divinski, M. Asta, and Y. Mishin. Effect of interface phase transformations on diffusion and segregation in high-angle grain boundaries. *Phys. Rev. Lett.*, 110:255502, Jun 2013.

[39] G. Duscher, M. F. Chisholm, U. Alber, and M. Ruhle. Bismuth-induced embrittlement of copper grain boundaries. *Nat. Mater.*, 3:621, 2004.

[40] R. Schweinfest, A.T. Paxton, and M. W. Finnis. Bismuth embrittlement of copper is an atomic size effect. *Nature*, 432:1008, 2004.

[41] Patrick R. Cantwell, Ming Tang, Shen J. Dillon, Jian Luo, Gregory S. Rohrer, and Martin P. Harmer. Grain boundary complexions. *Acta Materialia*, 62:1 – 48, 2014.

[42] K. Wolski, V. Laporte, N. Mari, and M. Biscondi. About the importance of nanometer-thick intergranular penetration in the analysis of liquid metal embrittlement. *Interface Science*, 9(3-4):183–189, 2001.

[43] E. Pereiro-López, W. Ludwig, D. Bellet, P. Cloetens, and C. Lemaignan. Direct evidence of nanometric invasionlike grain boundary penetration in the Al/Ga system. *Phys. Rev. Lett.*, 95:215501, Nov 2005.

[44] Kaveh Meshinchi Asl and Jian Luo. Impurity effects on the intergranular liquid bismuth penetration in polycrystalline nickel. *Acta Materialia*, 60(1):149 – 165, 2012.

[45] N. Mari, K. Wolski, and M. Biscondi. Grain boundary penetration of nickel by liquid bismuth as a film of nanometric thickness. *Scripta Materialia*, 43(10):943–949, 2000.

[46] Jochen Schlhammer, Brigitte Baretzky, Wolfgang Gust, Eric Mittemeijer, and Boris Straumal. Grain boundary grooving as an indicator of grain boundary phase transformations. *Interface Science*, 9(1-2):43–53, 2001.

[47] L.-S. Chang and K.-B. Huang. Temperature dependence of the grain boundary segregation of bi in ni polycrystals. *Scripta Materialia*, 51(6):551 – 555, 2004.

[48] Animesh Kundu, Kaveh Meshinchi Asl, Jian Luo, and Martin P. Harmer. Identification of a bilayer grain boundary complexion in bi-doped cu. *Scripta Mater.*, 68(2):146 – 149, 2013.

[49] B.B. Straumal, O. Kogtenkova, and P. Zi.ba. Wetting transition of grain-boundary triple junctions. *Acta Materialia*, 56(5):925 – 933, 2008.

[50] Yuanyao Zhang and Jian Luo. Observation of an unusual case of triple-line instability. *Scripta Materialia*, 88:45 – 48, 2014.

[51] D. McLean. Grain boundaries in metals. *Oxford: Clarendon Press*, 1957.

[52] Y.W. Lee and H.I. Aaronson. Anisotropy of coherent interphase boundary energy. *Acta Metallurgica*, 28(4):539 – 548, 1980.

[53] Y.W. Lee and H.I. Aaronson. Surface concentration profile and surface energy in binary alloys. *Surface Science*, 95(1):227 – 244, 1980.

[54] Daniel A. Steigerwald, Sarah J. Miller, and Paul Wynblatt. Anisotropy of surface composition in a ni.au alloy. *Surface Science*, 155(1):79 – 100, 1985.

[55] P. Wynblatt and R.C. Ku. Surface energy and solute strain energy effects in surface segregation. *Surface Science*, 65(2):511 – 531, 1977.

[56] J. Friedel. Electronic structure of primary solid solutions in metals. *Advances in Physics*, 3(12):446–507, 1954.

[57] J.M. Rickman, H.M. Chan, M.P. Harmer, and J. Luo. Grain-boundary layering transitions in a model bicrystal. *Surface Science*, 618:88 – 93, 2013.

[58] Ming Tang, W. Craig Carter, and Rowland M. Cannon. Grain boundary transitions in binary alloys. *Phys. Rev. Lett.*, 97:075502, Aug 2006.

[59] Jian Luo. Grain boundary complexions: The interplay of premelting, prewetting, and multilayer adsorption. *Applied Physics Letters*, 95(7):–, 2009.

[60] Y. Mishin, M. Asta, and Ju Li. Atomistic modeling of interfaces and their impact on microstructure and properties. *Acta Materialia*, 58(4):1117 – 1151, 2010.

[61] Sergiy V. Divinski, Henning Edelhoff, and Sergei Prokofjev. Diffusion and segregation of silver in copper $\Sigma 5(310)$ grain boundary. *Phys. Rev. B*, 85:144104, Apr 2012.

[62] E. Budke, T. Surholt, S.I. Prokofjev, L.S. Shvindlerman, and Chr. Herzig. Tracer diffusion of au and cu in a series of near .=5 (310)[001] symmetrical cu tilt grain boundaries. *Acta Materialia*, 47(2):385 – 395, 1999.

[63] Vladislav Domnich, Sara Reynaud, Richard A. Haber, and Manish Chhowalla. Boron carbide: Structure, properties, and stability under stress. *Journal of the American Ceramic Society*, 94(11):3605–3628, 2011.

[64] Marek Mihalkovič and C. L. Henley. Empirical oscillating potentials for alloys from *ab initio* fits and the prediction of quasicrystal-related structures in the al-cu-sc system. *Phys. Rev. B*, 85:092102, Mar 2012.

[65] Richard Martin. Electronic structure. 2005.

[66] David Sholl and Janice Steckel. Density functional theory. 2009.

[67] E. Schrödinger. An undulatory theory of the mechanics of atoms and molecules. *Phys. Rev.*, 28:1049–1070, Dec 1926.

[68] M. Born and R. Oppenheimer. Zur quantentheorie der molekeln. *Annalen der Physik*, 389(20):457–484, 1927.

[69] J. C. Slater. The theory of complex spectra. *Phys. Rev.*, 34:1293–1322, Nov 1929.

[70] P. Hohenberg and W. Kohn. Inhomogeneous electron gas. *Phys. Rev.*, 136:B864–B871, Nov 1964.

[71] Kohn W. highlights in condensed matter theory. 1985.

[72] Mel Levy. Electron densities in search of hamiltonians. *Phys. Rev. A*, 26:1200–1208, Sep 1982.

[73] W. Kohn and L. J. Sham. Self-consistent equations including exchange and correlation effects. *Phys. Rev.*, 140:A1133–A1138, Nov 1965.

[74] E. Wigner and F. Seitz. On the constitution of metallic sodium. ii. *Phys. Rev.*, 46:509–524, Sep 1934.

[75] John P. Perdew and Yue Wang. Accurate and simple analytic representation of the electron-gas correlation energy. *Phys. Rev. B*, 45:13244–13249, Jun 1992.

[76] D. M. Ceperley and B. J. Alder. Ground state of the electron gas by a stochastic method. *Phys. Rev. Lett.*, 45:566–569, Aug 1980.

[77] J. P. Perdew, K. Burke, and M. Ernzerhof. Generalized gradient approximation made simple. *Phys. Rev. Lett.*, 77:3865, 1996.

[78] Felix Bloch. ber die quantenmechanik der elektronen in kristallgittern. *Zeitschrift fr Physik*, 52(7-8):555–600, 1929.

[79] Frank Jensen. Introduction to computational chemistry. 2007.

[80] Pekka Pyykko. Relativistic effects in structural chemistry. *Chemical Reviews*, 88(3):563–594, 1988.

[81] P. A. M. Dirac. The quantum theory of the electron. *Proceedings of the Royal Society of London. Series A, Containing Papers of a Mathematical and Physical Character*, 117(778):610–624, 1928.

[82] Leslie L. Foldy and Siegfried A. Wouthuysen. On the dirac theory of spin 1/2 particles and its non-relativistic limit. *Phys. Rev.*, 78:29–36, Apr 1950.

[83] G. Kresse, J. Furthmller, and J. Hafner. Ab initio force constant approach to phonon dispersion relations of diamond and graphite. *EPL (Europhysics Letters)*, 32(9):729, 1995.

[84] Z. Zhang, Q. Niu, and C.K. Shih. "electronic growth" of metallic overlayers on semiconductor substrates. *Phys. Rev. Lett.*, 80:24, 1998.

[85] Ph. Hofmann. The surfaces of bismuth: Structural and electronic properties. *Prog. in Surf. Sci.*, 81:191, 2006.

[86] V. S. Edel'mman. Electrons in bismuth. *Advances in Physics*, 25:555, 1976.

[87] E. I. Rogacheva, S. N. Grigorov, S. Lyubchenko O. N. Nashchekina, and M. S. Dresselhaus. Quantum-size effects in n-type bismuth thin films. *Appl. Phys. Lett.*, 82:2628, 2003.

[88] T. Nagao, J. T. Sadowski, M. Saito, S. Yaginuma, Y. Fujikawa, T. Kogure, T. Ohno, Y. Hasegawa, S. Hasegawa, and T. Sakurai. Nanofilm allotrope and phase transformation of ultrathin bi film on si(111)-77. *Phys. Rev. Lett.*, 93:105501, 2004.

[89] V. Fourneé, H. R. Sharma, M. Shimoda, A. P. Tsai, A. R. Ross B. Unal, T. A. Lograsso, and P. A. Thiel. Quantum size effects in metal thin films grown on quasicrystalline substrates. *Phys. Rev. Lett.*, 95:155504, 2005.

[90] S. Yaginumaa, T. Nagaoa, J.T. Sadowski, M. Saito, K. Nagaoka, Y. Fujikawa, T. Sakurai, and T. Nakayama. Origin of flat morphology and high crystallinity of ultrathin bismuth films. *Surf. Sci.*, 601:3593, 2007.

[91] H. Jones. Applications of the bloch theory to the study of alloys and of the properties of bismuth. *Proc. Roy. Soc. A (London)*, 147:396, 1934.

[92] H. Mönig, J. Sun, Yu. M. Koroteev, G. Bihlmayer, J. Wells, E. V. Chulkov, K. Pohl, and Ph. Hofmann. Structure of the (111) surface of bismuth: Leed analysis and first-principles calculations. *Phys. Rev. B*, 72:085410, Aug 2005.

[93] T. R. J. Bollmann, R. van Gastel, H. J. W. Zandvliet, and B. Poelsema. Erratum: Quantum size effect driven structure modifications of bi films on ni(111). *Phys. Rev. Lett.*, 109:269903, 2012.

[94] G. Kresse and J. Hafner. Ab initio molecular dynamics for liquid metals. *Phys. Rev. B*, 47:RC558–61, 1993.

[95] G. Kresse and J. Furthmuller. Efficient iterative schemes for ab initio total-

energy calculations using a plane-wave basis set. *Phys. Rev. B*, 54:11169–86, 1996.

[96] P. E. Blochl. Projector augmented-wave method. *Phys. Rev. B*, 50:17953–79, 1994.

[97] G. Kresse and D. Joubert. From ultrasoft pseudopotentials to the projector augmented-wave method. *Phys. Rev. B*, 59:1758–75, 1999.

[98] Vincenzo Fiorentini and M Methfessel. Extracting convergent surface energies from slab calculations. *J. Phys.: Condens. Matter*, 8:6525, 1996.

[99] B. Wu and Z. Zhang. Stability of metallic thin films studied with a free electron model. *Phys. Rev. B.*, 77:035410, 2008.

[100] J. R. Kitchin, K. Reuter, and M. Scheffler. Alloy surface segregation in reactive environments: First-principles atomistic thermodynamics study of ag3p(111) in oxygen atmospheres. *Phys. Rev. B*, 77:075437, 2007.

[101] Toru Hirahara, Gustav Bihlmayer, Yusuke Sakamoto, Manabu Yamada, Hidetoshi Miyazaki, Shin-ichi Kimura, Stefan Blügel, and Shuji Hasegawa. Interfacing 2d and 3d topological insulators: Bi(111) bilayer on bi_2te_3. *Phys. Rev. Lett.*, 107:166801, 2011.

[102] Fang Yang, Lin Miao, Z. F. Wang, Meng-Yu Yao, Fengfeng Zhu, Y. R. Song, Mei-Xiao Wang, Jin-Peng Xu, Alexei V. Fedorov, Z. Sun, G. B. Zhang, Canhua Liu, Feng Liu, Dong Qian, C. L. Gao, and Jin-Feng Jia. Spatial and energy distribution of topological edge states in single bi(111) bilayer. *Phys. Rev. Lett.*, 109:016801, 2012.

[103] S. J. Dillon, M. Tang, W. C. Carter, and M. P. Harmer. Complexion: A new concept for kinetic engineering in materials science. *Acta Mater.*, 55:6208, 2007.

[104] T. Miller, A. Samsavar, G. E. Franklin, and T. C. Chiang. Quantum-well states in a metallic system: Ag on au(111). *Phys. Rev. Lett.*, 61:1404, 1988.

[105] C. M. Wei and M. Y. Chou. Quantum size effect in pb(100) films: Critical role of crystal band structure. *Phys. Rev. B.*, 75:195417, 2007.

[106] J. Luo. *Private communication*, 2013.

[107] Richard Dronskowski and Peter E. Bloechl. Crystal orbital hamilton populations (cohp): energy-resolved visualization of chemical bonding in solids based on density-functional calculations. *The Journal of Physical Chemistry*, 97(33):8617–8624, 1993.

[108] O. Jepsen and O.K. Andersen. Calculated electronic structure of the sandwichd1 metals lai2 and cei2: Application of new lmto techniques. *Zeitschrift fr Physik B Condensed Matter*, 97(1):35–47, 1995.

[109] Michael D. Sangid, Huseyin Sehitoglu, Hans J. Maier, and Thomas Niendorf. Grain boundary characterization and energetics of superalloys. *Materials Science and Engineering: A*, 527(26):7115 – 7125, 2010.

[110] Von L. E. Murr. Interfacial phenomena in metal and alloys. *Interfacial Phenomena in Metal and Alloys, Addison-Wesley Publishing Company*, page 138, 1975.

[111] Masatake Yamaguchi, Motoyuki Shiga, and Hideo Kaburaki. Energetics of segregation and embrittling potency for non-transition elements in the ni $\sigma 5$ (012) symmetrical tilt grain boundary: a first-principles study. *Journal of Phys.: Condens. Matter*, 16(23):3933, 2004.

[112] M. A. Tschopp and D. L. Mcdowell. Asymmetric tilt grain boundary structure and energy in copper and aluminium. *Phil. Mag.*, 87(25):3871–92, 2007.

[113] D. Kaminski, P. Poodt, E. Aret, N. Radenovic, and E. Vlieg. Surface alloys, overlayer and incommensurate structures of bi on cu(111). *Surface Science*, 575(3):233 – 246, 2005.

[114] B. Blum and H. Ascolani. The growth modes of vapor-deposited bi on cu(210). *Surface Science*, 482-485, Part 2(0):946 – 953, 2001.

[115] David L. Olmsted, Stephen M. Foiles, and Elizabeth A. Holm. Survey of computed grain boundary properties in face-centered cubic metals: I. grain boundary energy. *Acta Materialia*, 57(13):3694 – 3703, 2009.

[116] G Kresse, J Furthmüller, and J Hafner. Ab initio force constant approach to phonon dispersion relations of diamond and graphite. *EPL (Europhysics Letters)*, 32(9):729, 1995.

[117] M. Mihalkovič and M. Widom. Structure and stability of al_2fe and al_5fe_2: First-principles total energy and phonon calculations. *Phys. Rev. B*, 85:014113, Jan 2012.

[118] T. Ossowski, J. Kuriplach, E. Zhurkin, M. Hou, and A. Kiejna. Structure and stability of grain boundaries in iron. Presented as the 27th Max Born Symposium, Wroclaw, Poland, 2010.

[119] Bo Sun, Ping Zhang, Suqing Duan, Xian-Geng Zhao, and Qi-Kun Xue. First-principles calculations of cs adsorbed on cu(001): Quantum size effect in surface energetics and surface chemical reactivities. *Phys. Rev. B*, 75:245422, Jun 2007.

[120] J. Sanchez, F. Ducastelle, and D. Gratias. Generalized cluster description of multicomponent systems. *Physica A*, 1984.

[121] D. De Fontaine. Cluster approach to order-disorder transformations in alloys. In H. Ehrenreich and D. Turnbull, editors, *Solid State Physics*, volume 47 of *Solid State Physics*, pages 33 – 176. Academic Press, 1994.

[122] Stefano Curtarolo, Gus L. W. Hart, Marco Buongiorno Nardelli, Natalio Mingo, Stefano Sanvito, and Ohad Levy. The high-throughput highway to computational materials design. *Nature Materials*, 12:191, 2013.

[123] Atsuto Seko, Tomoya Maekawa, Koji Tsuda, and Isao Tanaka. Machine learning with systematic density-functional theory calculations: Application to melting temperatures of single- and binary-component solids. *Phys. Rev. B*, 89:054303, Feb 2014.

[124] K. T. Schütt, H. Glawe, F. Brockherde, A. Sanna, K. R. Müller, and E. K. U. Gross. How to represent crystal structures for machine learning: Towards fast prediction of electronic properties. *Phys. Rev. B*, 89:205118, May 2014.

[125] Zhenwei Li, James R. Kermode, and Alessandro De Vita. Molecular dynamics with on-the-fly machine learning of quantum-mechanical forces. *Phys. Rev. Lett.*, 114:096405, Mar 2015.

[126] Snke Lorenz, Axel Gro, and Matthias Scheffler. Representing high-dimensional potential-energy surfaces for reactions at surfaces by neural networks. *Chemical Physics Letters*, 395(4.6):210 – 215, 2004.

[127] Jörg Behler and Michele Parrinello. Generalized neural-network representation of high-dimensional potential-energy surfaces. *Phys. Rev. Lett.*, 98:146401, Apr 2007.

[128] Albert P. Bartók, Mike C. Payne, Risi Kondor, and Gábor Csányi. Gaussian approximation potentials: The accuracy of quantum mechanics, without the electrons. *Phys. Rev. Lett.*, 104:136403, Apr 2010.

[129] Matthias Rupp, Alexandre Tkatchenko, Klaus-Robert Müller, and O. Anatole von Lilienfeld. Fast and accurate modeling of molecular atomization energies with machine learning. *Phys. Rev. Lett.*, 108:058301, Jan 2012.

[130] Karl A. Schwetz and P. Karduck. Investigations in the boron-carbon system with the aid of electron probe microanalysis. *Journal of the Less Common Metals*, 175(1):1 – 11, 1991.

[131] H. Okamoto. B-c (boron-carbon). *Journal of Phase Equilibria*, 13(4):436–436, 1992.

[132] Sanxi Yao, W.P. Huhn, and M. Widom. Phase transitions of boron carbide: Pair interaction model of high carbon limit. *Solid State Sciences*, (0):–, 2014.

[133] P. Paufler. F. ducastelle. order and phase stability in alloys. (cohesion and structure vol. 3). north-holland/elsevier science publishers, amsterdam 1991. 511. *Crystal Research and Technology*, 27(6):874–874, 1992.

[134] A. van de Walle and G. Ceder. Automating first-principles phase diagram calculations. *J. Phase Equil.*, 23:348, 2002.

[135] Beale Mark Hudson, Hagan Martin T., and Demuth Howard B. Neural network toolbox for use with matlab version 8.3. *Mathworks*, 2015.

[136] Carl Edward Rasmussen. *Gaussian processes for machine learning*, 2006.

[137] Carl Edward Rasmussen and Hannes Nickisch. Gaussian processes for machine learning (gpml) toolbox. *J. Mach. Learn. Res.*, 11:3011–3015, December 2010.

[138] Christopher Bishop. *Pattern Recognition and Machine Learning*, 2007.

[139] Chih-Chung Chang and Chih-Jen Lin. Libsvm: A library for support vector machines. *ACM Trans. Intell. Syst. Technol.*, 2(3):27:1–27:27, May 2011.

[140] R. B. Griffiths and J. C. Wheeler. Critical points in multicomponent systems. *Phys. Rev. A*, 1970.

[141] D. A. Kofke. Semigrand canonical monte carlo simulation; integration along coexistence lines. In I. Prigogine and S. A. Rice, editors, *Adv. Chem. Phys: Monte Carlo Methods in Chem. Phys.*, volume 105, pages 405–441. Wiley, 1999.

[142] M. Widom and W. P. Huhn. Prediction of orientational phase transition in boron carbide. *Sol. State Sci.*, pages 1648–52, 2012.

[143] R. H. Swendsen and J. S. Wang. Replica monte carlo simulation of spin glasses. *Phys. Rev. Lett.*, 57:2607–9, 1986.

[144] Alan M. Ferrenberg and Robert H. Swendsen. Optimized monte carlo data analysis. *Phys. Rev. Lett.*, 63:1195–1198, Sep 1989.

[145] Alan M. Ferrenberg and Robert H. Swendsen. New monte carlo technique for studying phase transitions. *Phys. Rev. Lett.*, 61:2635–2638, Dec 1988.